

Seakeeping calculations
for ships,
taking into account the
non-linear steady waves

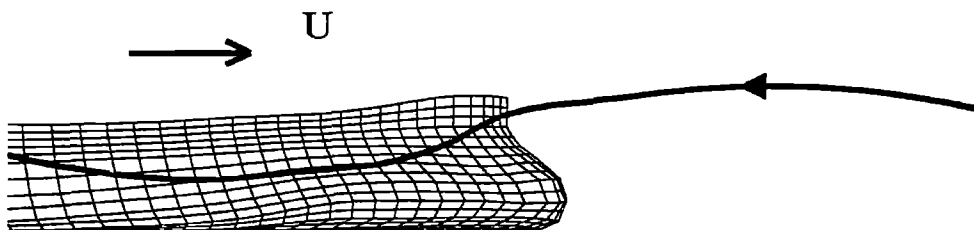
TECHNISCHE UNIVERSITEIT

Scheepshydraulica

Archief

Mekelweg 2, 2628 CD Delft

Tel: 015-2786873 / Fax: 2781836



Tim Bunnik

**Seakeeping calculations
for ships,
taking into account the
non-linear steady waves**

**Seakeeping calculations
for ships,
taking into account the
non-linear steady waves**

PROEFSCHRIFT

ter verkrijging van de graad van doctor
aan de Technische Universiteit Delft,
op gezag van Rector Magnificus prof. ir. K.F. Wakker,
in het openbaar te verdedigen ten overstaan van een commissie,
door het College voor Promoties aangewezen,
op maandag 22 november 1999 te 13.30 uur

door

Timotheus Henricus Joannes BUNNIK

wiskundig ingenieur,
geboren te Gouda.

Dit proefschrift is goedgekeurd door de promotor:

Prof. dr. ir. A.J. Hermans

Samenstelling promotiecommissie:

Rector Magnificus

Prof. dr. ir. A.J. Hermans

Prof. dr. R. Eatock Taylor

Prof. dr. ir. H.W. Hoogstraten

Prof. dr. ir. J.J.W. van der Vegt

Prof. dr. H.G. Meijer

Prof. dr. ir. J.A. Pinkster

Dr. ir. H.C. Raven

voorzitter

Technische Universiteit Delft, promotor

University of Oxford

Universiteit Groningen

Universiteit Twente

Technische Universiteit Delft

Technische Universiteit Delft

Marin, Wageningen

Copyright ©1999 by T.H.J. Bunnik

ISBN 90-9013222-8

Contents

List of symbols	v
Introduction	1
1 Mathematical formulation	5
1.1 Overview of recently developed methods	5
1.2 Introduction	8
1.3 The non-linear formulation	9
1.4 The linear formulation	12
1.4.1 The free-surface condition	12
1.4.2 The hull boundary condition	16
1.5 Absorbing boundary condition	16
1.6 Forces and moments	20
1.6.1 Steady forces and moments	22
1.6.2 First-order forces and ship motions	22
1.6.3 Second-order forces and moments	24
1.7 Solving the Laplace equation	25
2 Numerical formulation	29
2.1 Introduction	29
2.2 Discretization of the boundary integral	30
2.2.1 Raised panels	33
2.3 Discretization of the free-surface condition	34
2.4 Derivatives of the steady velocity	38
2.4.1 The derivatives of the squared velocity	39
2.4.2 The transfer term	40
2.4.3 Derivatives of the velocity on the hull	42
2.4.4 Interpolation of steady velocities and derivatives	43
2.5 Incoming waves	44
2.6 Symmetry relations	44
2.7 Parallelization of the computer code	47
3 Accuracy and stability analysis	49
3.1 Introduction	49
3.2 The continuous dispersion relation	51

3.3	The discrete dispersion relation	53
3.4	Damping and dispersion	55
3.5	Temporal stability	62
3.6	Summary and conclusions	66
4	Test case	67
4.1	Introduction	67
4.2	Convergence of steady velocities and their derivatives	69
4.3	Modeling incoming waves	72
4.4	Convergence of unsteady waves and forces	76
4.5	Influence of the transfer term	82
4.6	Summary and conclusions	85
5	Results for an LNG carrier	87
5.1	Introduction	87
5.2	Convergence of steady velocities and their derivatives	88
5.3	Added mass, damping and ship motions	93
5.4	Added resistance	98
5.5	Comparison with other linearizations	104
5.6	Summary and conclusions	108
	Discussion and conclusions	109
A	Restoring-force coefficients	111
B	Derivation of the discrete dispersion relation	113
B.1	The continuous Fourier transform of the Green function	113
B.2	The discrete dispersion relation	115
	Bibliography	119
	Summary	123
	Samenvatting (Summary in Dutch)	125
	Dankwoord (Acknowledgements in Dutch)	127
	Curriculum Vitae (in Dutch)	128

List of symbols

A	added-mass matrix
B	breadth
B	damping matrix
C	matrix of restoring-force coefficients
C_i	numerical damping
C_r	numerical dispersion
\vec{F}	force
Fn	Froude number
$Fn_{\Delta x}$	grid Froude number
G	Green's function
H	hull surface
\bar{H}	mean wetted hull surface
L	ship's length
M	mass matrix
\vec{M}	moment
R_w	wave resistance
S	free-surface function
T	transfer term
U	forward speed
Z	growth rate
\vec{X}	translational motion
g	gravitational acceleration
h	water depth
i	imaginary unit, $i^2 = -1$
k	wave number
k_{xx}	transverse gyradius
k_{yy}	longitudinal gyradius
k_{zz}	vertical gyradius
m	ship's mass
\vec{n}	normal vector
p	pressure
p_0	atmospheric pressure
r	distance between two points
t	time

$\vec{u} = (u, v, w)^T$	fluid velocity
$\vec{x} = (x, y, z)^T$	coordinates
\vec{x}_g	centre of gravity
z_{fs}	raised-panel distance
Φ	total potential
Φ_s	stationary potential
$\vec{\Omega}$	rotational motion
$\vec{\alpha}$	total displacement
$\hat{\alpha}$	dimensionless longitudinal wave number
$\hat{\beta}$	dimensionless transverse wave number
γ	phase shift of rotational motion
δ	phase shift of translational motion
ϵ	small parameter
ζ	wave height
ζ_a	amplitude of incoming wave
θ	angle of incidence
κ	quotient of transverse and longitudinal panel size
λ	wavelength
μ	dimensionless raised-panel distance
ν	artificial damping
ρ	density
σ	source strength
τ	speed-frequency number
ϕ	time-dependent potential
ω	frequency of encounter
$\hat{\omega}$	dimensionless frequency
ω_0	earth-fixed frequency
Δt	time step
Δx	longitudinal panel size
Δy	transverse panel size
Δz	vertical distance
Δ	mean submerged volume of the ship

Introduction

A ship sailing at sea is exposed to forces due to wind, current and waves. These forces not only cause the motions of the ship, which can be very annoying for its passengers, but also account for the resistance of the ship or drift the ship away from its course. The resistance of the ship is balanced by the propulsive power of the ship, and is desired to be as small as possible to save fuel and to keep the costs of transport as low as possible. The drifting of the ship can be checked by adjusting the angle of the rudder.

The two most important contributions to the resistance of a ship are the resistance due to viscosity and the resistance due to the excitation of waves. In still water, the second contribution is called the wave resistance. Especially for high forward speed, this contribution may become larger than the viscous contribution. The corresponding steady waves are characteristic for a ship sailing at a constant speed, and can easily be spotted when you watch a ship go by while waiting for an open bridge: This wave pattern and the corresponding wave resistance can be approximated by a method called RAPID, which has been developed at the MARitime Research INstitute (MARIN) in recent years. Unlike most other methods, it takes into account the non-linear behaviour of the waves and therefore gives more reliable predictions for the wave resistance than linearized methods.

When the sea is not calm, and the ship sails in incoming waves then, besides the steady resistance, the ship experiences a time-varying force. When the mean value of the incoming waves is zero, this force nevertheless can have a mean value which is non-zero due to quadratic effects. The direction of this force is the direction that the incoming waves propagate, so the incoming waves want to push the ship ahead of them. This means that, when the waves come in front, the ship experiences an extra resistance, called the added resistance, which leads to a power loss. Besides this power loss, a transverse force will drift the ship from its course, and a rotating moment about the ship's vertical axis leads to a change of its course. Therefore, eventually, the ship will sail in head waves or following waves, unless this is prevented by adjusting the angle between the rudder and the forward direction of the ship.

It is important that, before a ship is built, as much as possible is known about the ship's performance in calm water and in waves. Therefore, a scale model of the ship can be built and tested in a basin in which a uniform stream and incoming waves are generated. This is done, amongst others, at the MARIN in Wageningen. These model tests are very expensive and, although they are irreplaceable, a tool is sought that can assist these tests,

gain more physical insight and maybe take over some of the tests once it has been thoroughly validated. This tool is found in simulating the model basin on a computer. With the increase in computer power, it has become possible to simulate a ship's behaviour in waves numerically. These simulations are based on mathematical descriptions of the physics of the ship and the sea. Although they are always an approximate description of reality, under certain circumstances they can be very helpful in the process of optimizing the performance of a ship.

In this thesis we derive a mathematical and numerical model that can determine the motions of and the forces on a ship sailing in waves. Emphasis is laid on making the model suitable for moderate and high speeds of the ship. For low speeds, various models already exist that are too simple however, to obtain reliable results when we increase the speed, because they use a very simple approximation of the steady flow around the ship. Because the interaction between the steady flow around the ship on the one hand and the incoming waves, the motion of the ship and the drift forces on the other hand is very strong, we need a better description for the steady flow. Therefore, we use the non-linear steady flow, that can be determined by RAPID, to model the steady flow around the ship. It is very hard to determine the remaining, time-dependent waves that propagate over the steady waves, because some non-linearities are involved. Therefore, we make some assumptions on the steepness of these time-dependent waves and the amplitudes of the motions of the ship, which allow us to linearize the equations that describe the propagation of these waves and the ship's motions. The result is a linear mathematical model that, unfortunately, cannot be solved analytically. Therefore, it has to be discretized, and the resulting numerical model is solved on a computer. This way we obtain an approximation of the solution of the mathematical model, which was a linearized version of a more difficult mathematical model, which was again an approximation of reality. Although this involves three simplification steps, we shall see that we can obtain some very nice predictions for the motions of and the forces on a ship sailing in waves.

In the first chapter we derive the mathematical model that describes the time-dependent flow around a ship and the motions of a ship. We assume that the fluid is inviscid and irrotational, which allows us to introduce a velocity potential that satisfies the equation of Laplace inside the fluid domain. The linearization is carried out and a linear free-surface condition and a linear hull condition are derived. By means of a boundary-element method, the three-dimensional problem is reduced to a two-dimensional problem, in which only the strength of pulsating sources on the boundaries (the free surface and the hull of the ship) has to be determined. Due to the linearization, separate expressions are found for the steady forces on the ship in calm water, the harmonic forces on the ship, which have a zero mean value and are of first order in the steepness of the incoming waves, and the drift forces, which generally have a non-zero mean value and are of second order in the steepness of the incoming waves.

Special attention is paid to the absorption of outgoing waves. In our model, the size of the sea is finite. Near the edges of this finite area, a special condition must be applied to absorb outgoing waves and to avoid that waves reflect and go back to the ship.

In the second chapter we discretize the mathematical model and transform it into a numerical model that can be solved on a computer. The hull of the ship and the free surface are divided into small areas, called panels, and on each of these panels the strength of the sources is assumed to be constant. Because of the linearization around the steady flow, we need the steady wave, the steady fluid velocities and several derivatives of these velocities. The steady wave and the steady velocities are directly calculated by RAPID. However, the derivatives have to be determined with difference schemes, and these are introduced. When this has been done we discretize the linear free-surface condition. It contains derivatives of the unsteady velocity potential in space and time. We discretize the time derivatives by using a difference scheme with a constant time step. This results in a time iteration in which we have to recalculate the unsteady flow at each time level. We discretize the space derivatives with upwind difference schemes. The result is a matrix equation for the unknown source strengths which can be solved with LU-decomposition.

In the third chapter we carry out an accuracy and stability analysis for a simplified model. We test whether or not several difference schemes are capable of predicting the correct wave amplitude and the correct wavelength. The stability of the time stepping depends on the rate at which the solution grows in each time step. If this rate is larger than one, the time stepping is unstable. We derive a discrete dispersion relation from which this growth rate can be found. It is shown that for moderate and high speeds, upwind difference schemes have to be used to guarantee stability. The more accurate central difference schemes can only be used if the ship has a small forward speed.

In the fourth chapter we apply the model to a test ship. We investigate the convergence of the steady waves, the derivatives of the steady velocities, and the convergence of the unsteady waves. We implement and compare two methods that simulate the incoming waves, and the best method is applied to the calculations in the fifth chapter. There, we apply the model to an LNG carrier. We calculate the motions and the added resistance of this ship for three moderate speeds, and for several lengths and angles of the incoming wave. The results are compared with measurements, carried out at the MARIN. Finally, conclusions are drawn and recommendations are made to improve the model.

Chapter 1

Mathematical formulation

In this chapter a mathematical model is presented that describes the unsteady water flow around a sailing ship. Because of the complex non-linearity of this model, some assumptions are made to linearize it. By means of perturbation techniques, equations are derived for the first- and second-order forces on a ship, and the equation of motion is formulated. Artificial damping is used to absorb outgoing waves and an investigation is made on how large the damping should be. Finally, we use Green's second identity to formulate a method to solve the Laplace equation.

1.1 Overview of recently developed methods

In the recent past, a lot of research in the field of unsteady potential-flow solvers has been done. When one starts developing a new model and computer code, it is important to have an overview of what already has been done, and prevent the wheel from being invented twice. Most of the potential-flow solvers use some kind of boundary-integral method, which can be derived from Green's theorem, resulting in the well-known panel methods. The methods can roughly be divided in three groups: the linear methods, the semi non-linear methods and the fully non-linear methods.

LINEAR METHODS

The most simple, but also the most practical methods are the linear methods. Although in some sense the amplitude of the solution must be assumed small, it is mostly possible to apply such models to a wide variety of applications without major difficulties. In a linear model, the time dependence can be removed by assuming that the solution is harmonic in time. This leads to the so-called frequency-domain approach. If no assumption is made on the time behaviour of the solution, a time-domain approach has to be used. The frequency-domain methods are generally the fastest, but are limited to simulating one frequency at a time. Furthermore, irregular frequencies may appear at which the solution becomes unbounded. When random seas are to be simulated, it is far more efficient to use a time-domain approach.

The approach that can be followed to solve the linear equations depends on the kind of linearization that is used and whether or not forward speed is involved. Generally, if the coefficients in the linear free-surface condition are independent of space, it is possible to find a Green function that satisfies the free-surface condition. If the coefficients are space dependent, it is mostly not possible to find such a Green function. The advantage of the use of a Green function that satisfies the free-surface condition is that singularities only have to be distributed over the ship's hull. The disadvantage is that the free-surface condition has to be relatively simple which often restricts the applicability of the model. Furthermore, it can be rather difficult to calculate this Green function. Without forward speed, it is very efficient to use a Green function that satisfies the free-surface condition and the radiation condition. Clément [11] found an ordinary differential equation for the time-domain Green function that makes it possible to calculate it very efficiently. With forward speed, the Green function becomes much more difficult to evaluate. When, for example, the source and field point are both on the free surface, this function becomes highly oscillatory, which makes its integration difficult. Huijsmans used the frequency-domain version of this Green function in his method to determine the mean wave drift force in current [17]. Korsmeyer and Bingham [21] use the time-domain version of this Green function to solve the forward speed diffraction problem in their code TIMIT. Recently, developments by Chen and Noblesse [10] have lead to a method that is able to calculate the highly oscillatory part of the Green function more accurately and efficiently. The same holds for the integrated Green function, which they call the "super Green function". Ba and Guilbaud [2] also developed a method that calculates the Green function fast, but to the author's knowledge, it has not been applied to a seakeeping code yet.

When the linear free-surface condition is more complicated, Green functions satisfying the free-surface condition cannot be found anymore. With forward speed, this happens for example when a linearization is carried out about a space-dependent steady flow like the double-body flow, instead of the uniform flow. In that case, it is very convenient to use a distribution of Rankine sources to obtain a solution. Prins [28] developed a time-domain code using the Rankine source and the double-body flow and applied this code successfully to a tanker with a small forward speed. Sierevogel [31] extended this code with a very effective absorbing boundary condition which makes it possible to use a much smaller part of the free surface in the computations. However, when she tried to increase the speed she got erroneous results for an LNG carrier, which is probably due to the fact that the double-body flow is used. Similarly, Skourup, Büchmann and Bingham [32] developed the linear time-domain code WAVETANK that determines the first and second-order potentials for several three-dimensional objects in waves. The results for the runup on a vertical mounted cylinder agree very well with the non-linear results from Ferrant [14]. At the MIT, several linear Rankine panel methods have been developed successfully, like the SWAN code by Nakos [24]. All these mentioned codes, however, are restricted to low speeds of the ship or current, because only first-order effects on forward speed are taken into account. Bertram [5] developed a linear frequency-domain Rankine panel method that takes into account the non-linear steady flow. His results have not shown yet that his method is capable of predicting the added resistance correctly.

Iwashita [18] developed the method further but encountered difficulties in predicting the correct wave elevation.

SEMI NON-LINEAR METHODS

Because linear methods are restricted to waves and motions with small amplitudes, methods have been developed that overcome such problems by adding some non-linearities. At the MIT for example, the computer code SWAN has been developed. Started as a linear code by Nakos [24], some non-linear features have been built in the code as well. The so-called weak scatterer method, see Huang and Sclavounos [16], does not require the amplitude of the incoming waves and the ship motions to be small. The only assumption that is made is that the waves that are diffracted and radiated by the ship are small, so the ship has to be slender. In that case, a linearization about the time-varying position of the incoming wave can be made, and the exact body boundary condition can be applied at the instantaneous submerged ship surface, resulting in a semi non-linear method. The Laplace equation is solved by distributing Rankine sources over the body surface and part of the free surface. However, at high forward speed the incoming wave is significantly diffracted, especially by a non-slender ship, and the method is no longer valid, which makes this approach not suitable for our purposes. The multi-level computer code LAMP developed by Lin and Yue [23] uses a similar approach, but with a mixed-source formulation. Close to the ship in an inner domain, Rankine sources are applied, and on the boundary of the inner domain the transient Green function is applied, so the radiation condition is automatically fulfilled.

NON-LINEAR METHODS

The rather complex and time-consuming fully non-linear methods have become popular in recent years because of the huge increase in computer power. The complexity lies in the fact that in case of non-linearities a time-domain algorithm has to be used in which a regridding is necessary because the geometry of the free surface and the position of the floating object changes during the simulation. This regridding is very expensive in terms of computational time. Another problem is that it is rather difficult to determine the intersection between the floating object and the free surface. With the increase of computer power, and the development of new algorithms, these methods become more and more promising. At the university of Twente, for example, research by Romate [30], Broeze [6], van Daalen [12], de Haas [15] and Berkvens [3] resulted in a method that is able to determine the non-linear waves around several two-dimensional floating objects for zero forward speed. In three dimensions results have been obtained for an oscillating sphere and for waves diffracting around a vertical mounted cylinder. Tanizawa [34] developed a similar, two-dimensional method with which large-amplitude body motions can be simulated. Another method called ANSWAVE, developed by Ferrant [14], is able to calculate the non-linear runup on a vertical cylinder with current. Similarly, Beck *et al.* [9] developed a numerical wave tank in which the non-linear waves around a vertical truncated cylinder can be determined. They use a desingularized method, in which the

sources are located above the free surface instead of on the free surface, as discussed in section 2.2.1. Finally, at the MIT a method has been developed to solve the non-linear wave body interactions with forward speed, see Kring *et al.* [22]. It has successfully been applied to a heaving Mobile Offshore Base and looks a very promising candidate for future non-linear seakeeping studies.

However, until now all these non-linear methods involve simplified geometries, or are limited to zero forward speed or small forward speed of the floating object and are therefore not yet capable of simulating the behaviour of commercial ships. Therefore, in this thesis we present a linear code. A time-domain algorithm is used so the code is not restricted to regular waves, and the steady flow is approximated by the non-linear flow to allow moderate and high speeds of the ship.

1.2 Introduction

The mathematical model presented in this chapter aims to predict the forces acting on a ship sailing in water waves, and its subsequent motions. The emphasis is laid on making the model suitable for moderate and high speeds of the ship, because until now, computer codes were mostly based on low-speed approximations.

There are a number of ways to model the water flow around a ship. Some of these are very complex, and it must therefore be considered whether these formulations are really necessary to capture the most important physics. The most exact description of the flow of water is given by the Navier-Stokes equations, which take into account the water's viscosity. Viscosity in ship hydrodynamics can be important in turbulent areas like, for example near a rudder, propulsor or a sharp edge of the hull, but none of these is considered in this thesis. Near the hull, a small boundary layer exists in which viscous effects dominate, but this layer does not really affect the large-scale interactions of ocean waves and ship motions. Only the roll motion of the ship is strongly influenced by viscosity, but fortunately, the roll motion does not affect the added resistance very much. In this study, the effect of viscosity is therefore neglected and potential theory is used to describe the flow of water.

Although this is a major simplification, the remaining problem is still very complicated due to the presence of a moving free surface and a surface-piercing body. The boundary condition on this free surface is non-linear in two ways. First, it is defined on a moving surface which is part of the solution and not known in advance. Second, the condition itself is non-linear because it contains products of the velocity potential. The steady non-linear problem (so without incoming waves and ship motions) has been solved numerically by Raven [29], amongst others. As indicated in the previous section, some efforts have been made to tackle the unsteady non-linear problem. Until now, the resulting models are restricted to simplified geometries or small forward speeds. Furthermore, the corresponding computer programs are very time consuming. We therefore decided to make a further simplification by linearizing the conditions on the free surface and the hull of the

ship.

As said, when the ship only has a forward speed, the non-linear problem can relatively easily be solved. The resulting steady base flow can be used to linearize the unsteady flow if the unsteady flow is assumed to be small. This way we incorporate the steady solution into our linear unsteady solution and let the two interact by means of linearized unsteady boundary conditions. Because all the steady characteristics of the ship are now included in the model, such as trim, sinkage and the steady wave profile, it is also suitable for moderate and high speeds.

1.3 The non-linear formulation

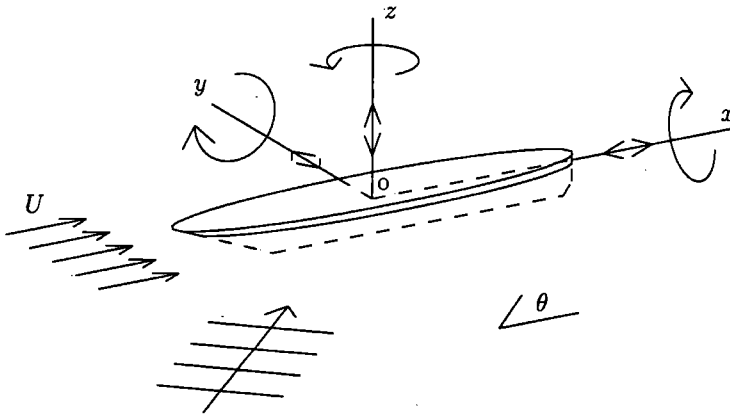


Figure 1.1: View of the geometry

We consider a symmetrical, smoothly-shaped ship sailing with a constant velocity U in incoming waves that propagate in a direction which makes an angle θ with the forward direction of the ship. We choose a coordinate system fixed to the ship and moving with its mean velocity. Standing in this coordinate system it is as if the ship has no forward speed and as if there is a current with velocity U coming from the bow side of the ship. The frequency at which the incoming waves are encountered changes due to this forward speed, unless the ship sails in beam waves. The x -axis is along the direction of this current in the symmetry plane of the ship. The z -axis points upwards and the origin lies in the undisturbed free surface $z = 0$. The ship is free to rotate around or translate along any of its axes. The water depth h is supposed to be constant and, therefore, the bottom corresponds to the plane $z = -h$.

The two objects in this study, the fluid and the ship, form a complex combination. Both have not only typical characteristics, they also interact. The moving fluid will search its way around the ship and unsteady forces and moments are generated by pressure changes in the fluid. These forces will cause the ship to rotate and translate, which again will generate motions of the fluid. In the mathematical model we therefore need separate descriptions for the behaviour of the fluid and the ship, and some condition describing the interaction between the two.

Water is a fluid with a low viscosity, which means it is not sticky like, for example, oil. Therefore, a first approximation that we make is that the water is not viscid at all, which simplifies our equations considerably. The influence of viscosity on the hydrodynamics of the ship is limited to a thin boundary layer near the hull, which does not influence the large-scale effects of incoming waves and ship motions very much, and justifies this approximation. If we also assume that the flow is irrotational and incompressible, a velocity potential Φ exists, which gradient is the velocity of a fluid particle

$$\vec{u} = \vec{\nabla}\Phi$$

Inside the fluid domain this potential satisfies the equation of Laplace, which follows from the conservation of mass

$$\Delta\Phi = 0$$

The solution of this equation is unique if, on the boundaries of the fluid domain, a linear combination of the potential and its normal derivative is given, and if in at least one point the potential is given. The solution is determinate, but for a constant if the value of the potential is nowhere specified. After differentiating, this constant disappears, so it has no influence on the velocity field. This implies that on the boundaries of the fluid domain, which are the free surface, the bottom of the water and the hull of the ship, we need conditions relating the potential and its normal derivative. Fortunately there are physical demands for these boundaries, which will give us these relations.

On the free surface two physical conditions hold. The first is the dynamic free-surface condition, stating that the pressure should equal the atmospheric pressure, which is true when we neglect surface tension. The pressure p inside the fluid follows from the equation of Bernoulli, which relates it to the velocity potential

$$-\frac{p - p_0}{\rho} = \frac{\partial\Phi}{\partial t} + \frac{1}{2}\vec{\nabla}\Phi \cdot \vec{\nabla}\Phi + gz - \frac{1}{2}U^2$$

Imposing atmospheric pressure on the unknown free surface $z = \zeta$ gives the dynamic free-surface condition

$$\zeta = \frac{-1}{g} \left(\frac{\partial\Phi}{\partial t} + \frac{1}{2}\vec{\nabla}\Phi \cdot \vec{\nabla}\Phi - \frac{1}{2}U^2 \right) \quad \text{on } z = \zeta \quad (1.1)$$

The second is the kinematic condition, stating that a fluid particle cannot leave the free surface, which is mathematically described by

$$\frac{\partial \Phi}{\partial x} \frac{\partial \zeta}{\partial x} + \frac{\partial \Phi}{\partial y} \frac{\partial \zeta}{\partial y} + \frac{\partial \zeta}{\partial t} - \frac{\partial \Phi}{\partial z} = 0 \quad \text{on } z = \zeta$$

If these two conditions are combined, the free-surface elevation ζ can be eliminated, resulting in a condition that only contains the velocity potential

$$\frac{\partial^2 \Phi}{\partial t^2} + \vec{\nabla} \Phi \cdot \vec{\nabla} \frac{\partial \Phi}{\partial t} + \left(\frac{\partial \Phi}{\partial x} \frac{\partial}{\partial x_\zeta} + \frac{\partial \Phi}{\partial y} \frac{\partial}{\partial y_\zeta} \right) \left(\frac{\partial \Phi}{\partial t} + \frac{1}{2} \vec{\nabla} \Phi \cdot \vec{\nabla} \Phi \right) + g \frac{\partial \Phi}{\partial z} = 0 \quad \text{on } z = \zeta \quad (1.2)$$

Care must be taken with the definition of the derivatives in this condition. The gradient, $\vec{\nabla}$, is defined as the vector with partial derivatives in x, y and z -direction. The partial derivatives $\frac{\partial}{\partial x_\zeta}$ and $\frac{\partial}{\partial y_\zeta}$, however, are here defined as operators working on a function that is defined at the free surface $z = \zeta$, so if $F = F(x, y, \zeta(x, y))$, these partial derivatives relate as follows to the partial derivatives $\frac{\partial}{\partial x}$ and $\frac{\partial}{\partial y}$

$$\frac{\partial F(x, y, \zeta(x, y))}{\partial x_\zeta} = \frac{\partial F}{\partial x} + \frac{\partial F}{\partial z} \frac{\partial \zeta}{\partial x} \quad \text{and} \quad \frac{\partial F(x, y, \zeta(x, y))}{\partial y_\zeta} = \frac{\partial F}{\partial y} + \frac{\partial F}{\partial z} \frac{\partial \zeta}{\partial y}$$

So implicitly, the vertical partial derivative is hidden in these expressions. The partial derivatives $\frac{\partial}{\partial x_\zeta}$ and $\frac{\partial}{\partial y_\zeta}$ can be obtained by calculating the differences between points on the free surface, so we can use very simple difference schemes for a flat plane.

The bottom of the water is a fixed boundary and no fluid particles may cross it. This means that the normal velocity of a fluid particle at the bottom should be zero and that only a tangential velocity component is allowed, which is expressed by

$$\frac{\partial \Phi}{\partial n} = 0 \quad \text{at } z = -h$$

The condition on the hull of the ship should take into account the interaction between the motion of the hull and the motion of the water at the hull. Just like the bottom of the water, the hull of the ship cannot be crossed by a fluid particle. The water should therefore have the same normal velocity as the ship's hull, which is expressed by

$$\frac{\partial \Phi}{\partial n} = \frac{\partial \alpha}{\partial t} \cdot \vec{n} \quad \text{on } H(t) \quad (1.3)$$

where α is the displacement and $H(t)$ the exact position of the ship's hull in the ship-fixed coordinate system.

To obtain a unique solution, we have to impose a radiation condition. This condition states that waves generated by the ship should propagate away from the ship. This

may sound obvious, but it is not. Because computer memory is limited, we can take into account only a small part of the free surface around the ship. When waves reach the edge of this computational domain, they may reflect and return to the ship if no proper condition is imposed. There are a lot of methods to avoid this and all have their advantages and disadvantages. We choose to damp the waves by introducing an artificial damping zone on the free surface. When waves enter this damping zone, their amplitudes decrease along the direction of propagation. If the damping is strong enough the waves have vanished when the edge of the computational domain is reached and cannot reflect. An extensive discussion on the use of artificial damping can be found in section 1.5.

1.4 The linear formulation

It is very difficult and time consuming to solve the non-linear equations formulated in the previous section, especially when the ship has a forward speed. With the increase of computer power, non-linear calculations become more and more promising. With the present state of computer technology, however, it is not yet possible to calculate the non-linear time-varying flow around a sailing ship within acceptable time limits yet. We therefore decided to make some approximations and linearize the boundary conditions.

1.4.1 The free-surface condition

In order to linearize the free-surface condition, we have to assume that the time-dependent flow around the ship is small in some sense. The small parameter we use in the linearization is the wave steepness $\epsilon = \frac{A}{\lambda}$, where A is the amplitude and λ the length of the time-dependent waves. It is not sufficient to require only a small wave amplitude, because then short waves might still break; a strongly non-linear effect that has not been accounted for by a linear model. If the wave steepness is assumed to be small, waves cannot break. The velocity potential is now decomposed into a steady, time-independent part Φ_s , and an unsteady, time-dependent part Φ_u . Because the time-dependent part is assumed to be small, it can be perturbed using the wave-steepness parameter ϵ

$$\Phi(\vec{x}, t) = \Phi_s(\vec{x}) + \Phi_u(\vec{x}, t) = \Phi_s(\vec{x}) + \epsilon\phi_u^{(1)}(\vec{x}, t) + \epsilon^2\phi_u^{(2)}(\vec{x}, t) + \dots \quad (1.4)$$

Φ_s is the solution of the flow problem without ship motions and incoming waves, so there is only a stream, with uniform velocity U at infinity, flowing around the ship. This steady solution is assumed to be known, and there are a number of ways to represent it, resulting in various linear free-surface conditions.

A very simple and straightforward way to model this flow is to assume that the water does not “feel” the presence of the ship and goes right through it, which means that the steady flow is uniform in the entire fluid. This assumption has the advantage that it leads to a relatively easy free-surface condition which can be solved by means of analytical techniques. This approximation is only valid for very slender ships and low speeds however, so it is not suitable for our model because we want to be able to obtain results for general

but smoothly-shaped hulls and moderate to high speeds.

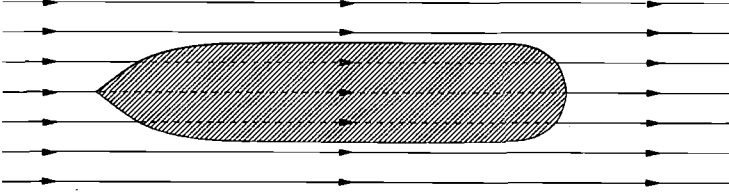


Figure 1.2: Top view of uniform-flow approximation.

A flow pattern which bears more resemblance to reality is the double-body flow. In this case the flow around the ship is approximated by the flow around the double body, which is the ship together with its reflection in the calm water plane $z = 0$. Because there is no longer a free surface, no waves are generated, but at least the no-flux condition on the hull of the ship is satisfied. This method is also only valid for low speeds; for higher speeds the steady wave pattern has to be taken into account.

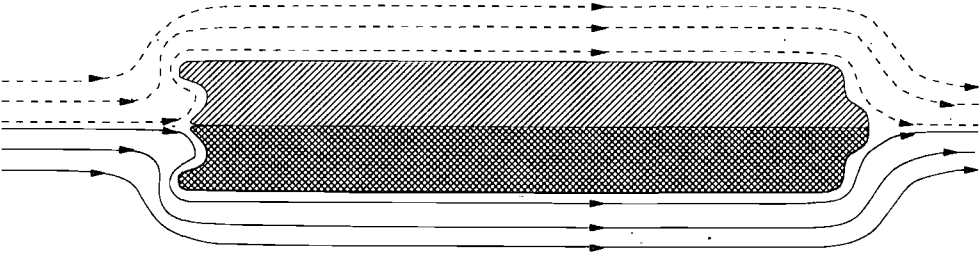


Figure 1.3: Side view of double-body-flow approximation.

It was shown by Raven [29] that to compute the wave resistance at finite speed, the complete non-linear free surface has to be taken into account. He therefore developed a method, RAPID, that can solve the non-linear steady flow, including trim and sinkage, around several types of vessels. RAPID means RAised Panel Iterative Dawson and the method obtains an approximation of the non-linear steady flow in a number of iterations, starting from a first guess and updating the previous approximation in each iteration. The solution found with RAPID satisfies up to a small discretization and truncation error

$$\frac{\partial \Phi_s}{\partial x} \frac{\partial \zeta_s}{\partial x} + \frac{\partial \Phi_s}{\partial y} \frac{\partial \zeta_s}{\partial y} - \frac{\partial \Phi_s}{\partial z} = 0 \quad \text{on } z = \zeta_s \tag{1.5}$$

ζ_s is the steady free-surface elevation that satisfies

$$\zeta_s = -\frac{1}{2g} \left(\vec{\nabla} \Phi_s \cdot \vec{\nabla} \Phi_s - U^2 \right) \tag{1.6}$$

On the hull, the steady flow satisfies the no-flux condition

$$\frac{\partial \Phi_s}{\partial n} = 0 \quad \text{on } H \quad (1.7)$$

and of course it satisfies the Laplace equation inside the fluid domain. We use the discrete RAPID solution of these equations to approximate the steady-flow potential Φ_s . In the derivation of the linear unsteady free-surface condition we will assume that the RAPID velocities satisfy the boundary conditions (1.5) and (1.7) exactly, but we must always keep in mind that we are dealing with an approximation of the non-linear steady flow.

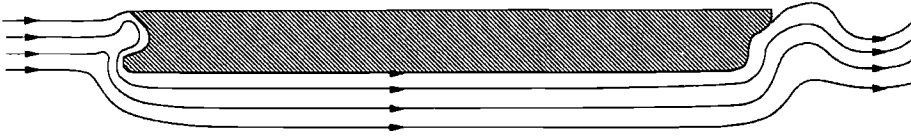


Figure 1.4: Side view of non-linear flow.

When the perturbed potential (1.4) is substituted in the dynamic free-surface condition (1.1), we find up to order ϵ

$$\zeta = -\frac{1}{g} \left(\epsilon \left(\frac{\partial \phi_u^{(1)}}{\partial t} + \vec{\nabla} \Phi_s \cdot \vec{\nabla} \phi_u^{(1)} \right) + \frac{1}{2} \vec{\nabla} \Phi_s \cdot \vec{\nabla} \Phi_s - \frac{1}{2} U^2 \right) \quad \text{on } z = \zeta$$

This condition is imposed on an unknown surface $z = \zeta$ which is part of the solution. This non-linearity is removed by expanding the dynamic free-surface condition (DFSC) in a Taylor series around the known steady free surface

$$(\text{DFSC})|_{z=\zeta} = (\text{DFSC})|_{z=\zeta_s} + (\zeta - \zeta_s) \frac{\partial}{\partial z} (\text{DFSC})|_{z=\zeta_s} + \mathcal{O}((\zeta - \zeta_s)^2) \quad (1.8)$$

If we also use the fact that the perturbed expression for the wave elevation looks like

$$\zeta = \zeta_s + \epsilon \zeta_u^{(1)} + \mathcal{O}(\epsilon^2)$$

then we find

$$\begin{aligned} \zeta_s + \epsilon \zeta_u^{(1)} = & -\frac{1}{2g} (\vec{\nabla} \Phi_s \cdot \vec{\nabla} \Phi_s - U^2) + \epsilon \left(-\frac{1}{g} \left(\frac{\partial \phi_u^{(1)}}{\partial t} + \vec{\nabla} \Phi_s \cdot \vec{\nabla} \phi_u^{(1)} \right) \right. \\ & \left. - \frac{1}{2g} \zeta_u^{(1)} \frac{\partial}{\partial z} (\vec{\nabla} \Phi_s \cdot \vec{\nabla} \Phi_s) \right) + \mathcal{O}(\epsilon^2) \quad \text{on } z = \zeta_s \quad (1.9) \end{aligned}$$

This means that the first-order wave elevation equals

$$\zeta_u^{(1)} = -\frac{1}{g} \left(\frac{\partial \phi_u^{(1)}}{\partial t} + \vec{\nabla} \Phi_s \cdot \vec{\nabla} \phi_u^{(1)} \right) / \left(1 + \frac{1}{2g} \frac{\partial}{\partial z} (\vec{\nabla} \Phi_s \cdot \vec{\nabla} \Phi_s) \right) \quad \text{on } z = \zeta_s \quad (1.10)$$

The same linearization procedure can be applied to the combined free-surface condition (1.2). When we substitute the perturbation series for the potential in that condition we find up to order ϵ

$$\begin{aligned} \frac{1}{2} \left(\frac{\partial \Phi_s}{\partial x} \frac{\partial}{\partial x_\zeta} + \frac{\partial \Phi_s}{\partial y} \frac{\partial}{\partial y_\zeta} \right) \|\vec{\nabla} \Phi_s\|^2 + g \frac{\partial \Phi_s}{\partial z} + \epsilon \left(\frac{\partial^2 \phi_u^{(1)}}{\partial t^2} + \vec{\nabla} \Phi_s \cdot \vec{\nabla} \frac{\partial \phi_u^{(1)}}{\partial t} \right. \\ \left. + \left(\frac{\partial \Phi_s}{\partial x} \frac{\partial}{\partial x_\zeta} + \frac{\partial \Phi_s}{\partial y} \frac{\partial}{\partial y_\zeta} \right) \left(\frac{\partial \phi_u^{(1)}}{\partial t} + \vec{\nabla} \Phi_s \cdot \vec{\nabla} \phi_u^{(1)} \right) + g \frac{\partial \phi_u^{(1)}}{\partial z} \right. \\ \left. + \frac{1}{2} \left(\frac{\partial \phi_u^{(1)}}{\partial x} \frac{\partial}{\partial x_\zeta} + \frac{\partial \phi_u^{(1)}}{\partial y} \frac{\partial}{\partial y_\zeta} \right) \|\vec{\nabla} \Phi_s\|^2 \right) = 0 \quad \text{on } z = \zeta \quad (1.11) \end{aligned}$$

where $\|\vec{\nabla} \Phi_s\|^2 = \left(\frac{\partial \Phi_s}{\partial x} \right)^2 + \left(\frac{\partial \Phi_s}{\partial y} \right)^2 + \left(\frac{\partial \Phi_s}{\partial z} \right)^2$ is the sum of the squares of the three steady velocities. With a Taylor-series expansion similar to (1.8), we transfer this condition to the known surface $z = \zeta_s$. If we use the fact that on this surface, the steady potential and surface elevation satisfy the steady kinematic free-surface condition (1.5), we find

$$\begin{aligned} \frac{\partial^2 \phi_u^{(1)}}{\partial t^2} + 2 \vec{\nabla} \Phi_s \cdot \vec{\nabla} \frac{\partial \phi_u^{(1)}}{\partial t} + \vec{\nabla} \Phi_s \cdot \vec{\nabla} \left(\vec{\nabla} \Phi_s \cdot \vec{\nabla} \phi_u^{(1)} \right) + \frac{1}{2} \left(\frac{\partial \phi_u^{(1)}}{\partial x} \frac{\partial}{\partial x_{\zeta_s}} + \frac{\partial \phi_u^{(1)}}{\partial y} \frac{\partial}{\partial y_{\zeta_s}} \right) \|\vec{\nabla} \Phi_s\|^2 \\ + g \frac{\partial \phi_u^{(1)}}{\partial z} + \zeta_s^{(1)} \frac{\partial}{\partial z} \left(\frac{1}{2} \left(\frac{\partial \Phi_s}{\partial x} \frac{\partial}{\partial x_{\zeta_s}} + \frac{\partial \Phi_s}{\partial y} \frac{\partial}{\partial y_{\zeta_s}} \right) \|\vec{\nabla} \Phi_s\|^2 + g \frac{\partial \Phi_s}{\partial z} \right) = 0 \quad \text{on } z = \zeta_s \quad (1.12) \end{aligned}$$

This free-surface condition was already derived by Newman [25] and was used in the seakeeping program FREDDY developed at the Technical University of Hamburg, see Bertram [5].

Far away from the ship, where the steady flow is uniform, so $\Phi_s = Ux$, this condition reduces to the Kelvin condition

$$\frac{\partial^2 \phi_u^{(1)}}{\partial t^2} + 2U \frac{\partial^2 \phi_u^{(1)}}{\partial x \partial t} + U^2 \frac{\partial^2 \phi_u^{(1)}}{\partial x^2} + g \frac{\partial \phi_u^{(1)}}{\partial z} = 0 \quad \text{on } z = 0 \quad (1.13)$$

When we compare these two linear free-surface conditions, it can be seen that the first contains two extra terms compared to the second one. The first extra term is a term with the products of unsteady velocities and partial derivatives of the squared velocity along the steady free surface. The second extra term is a transfer term which is included because the free-surface condition is imposed on the steady free surface instead of on the actual free surface. Both terms contain first and/or second derivatives of the steady velocity. If we want to use condition (1.12) we must first make sure that these derivatives can be calculated accurately. An investigation on their convergence is therefore made in chapter 4 for the test ship and in chapter 5 for the LNG carrier.

1.4.2 The hull boundary condition

The boundary condition on the hull (1.3) is non-linear in the sense that it is imposed on a moving boundary $H(t)$, which position is part of the solution and not known in advance. Timman and Newman [35] showed that if the displacement relative to the mean position of the ship is small, the boundary condition can be linearized about the mean position by using a Taylor expansion. To guarantee a small displacement, the amplitude of the incoming waves must be small, and the frequency of the incoming wave may not be near the eigenfrequency of the ship. This is because a small force near the eigenfrequency can still lead to large ship motions. The Taylor expansion results in the following condition

$$\frac{\partial \phi_u^{(1)}}{\partial n} = \frac{\partial \vec{\alpha}^{(1)}}{\partial t} \cdot \vec{n} + \left((\vec{\nabla} \Phi_s \cdot \vec{\nabla}) \vec{\alpha}^{(1)} - (\vec{\alpha}^{(1)} \cdot \vec{\nabla}) \vec{\nabla} \Phi_s \right) \cdot \vec{n} \quad (1.14)$$

where $\vec{\alpha}^{(1)}$ is the total first-order displacement vector, consisting of a translation $\vec{X}^{(1)}$ and a rotation $\vec{\Omega}^{(1)}$ relative to the centre of gravity of the ship \vec{x}_g , so

$$\vec{\alpha}^{(1)} = \vec{X}^{(1)} + \vec{\Omega}^{(1)} \times (\vec{x} - \vec{x}_g) \quad (1.15)$$

As can be seen, the hull boundary condition not only contains steady velocities on the hull, but also their derivatives. These derivatives must be examined carefully, because it can be hard to determine them accurately. Especially near stagnation points like for example at a blunt bow, it can be impossible to do so.

1.5 Absorbing boundary condition

When a ship sails at sea it will generate waves by diffracting incoming waves or by radiating waves. At a large sea these waves propagate away from the ship without encountering any obstacles that can reflect them back and they will disappear into infinity. We want our mathematical model to behave in the same way, which is made difficult by the fact that we have to truncate our free surface somewhere. This is because an infinite free surface cannot be discretized into a finite number of free-surface elements, which is required for a computer simulation. Therefore, a special condition has to be imposed to absorb waves that reach the truncation and to avoid that they reflect and propagate back to the ship. A lot of research has been done on absorbing boundary conditions and some methods will be summarized shortly.

Sommerfeld's radiation condition

A very popular method to absorb waves is to use Sommerfeld's radiation condition [33] on a vertical boundary that connects the free surface and the sea bottom. It relates the normal velocity and the time derivative of ϕ in terms of the local normal phase velocity c

$$c \frac{\partial \phi}{\partial n} + \frac{\partial \phi}{\partial t} = 0$$

This condition ensures that waves with phase velocity c are absorbed. Waves with other phase velocities are only partially absorbed and may reflect. The problem is to choose the appropriate phase velocity. It can be estimated in advance with an asymptotical analysis, or it can be estimated from data during the simulation. Because no continuous range of phase velocities can be dealt with, and because it is hard to determine the appropriate phase velocity, we prefer other methods.

DtN Relation

Sierevogel [31] developed an absorbing boundary condition independent of frequency called a DtN (Dirichlet-to-Neumann) relation. In her method, the fluid domain is divided in an inner and an outer domain. In the inner domain near the ship the double-body flow is used to approximate the steady flow, in the outer domain the Kelvin condition (1.13) is imposed on the free surface. By using a Green function that satisfies the discretized Kelvin condition, the flow also satisfies this condition and only the flow in the inner domain has to be solved. The disadvantage of this method is that the outer domain has to be in an area where the steady flow can be assumed uniform. When the non-linear wave pattern is used, the inner domain should be quite large because the non-linear disturbance of the steady flow can stretch over a wide area. Another disadvantage is that the method is quite extensive and costs a lot of work to implement compared to other simpler methods that achieve almost the same results.

Damping zone

To avoid reflections, it is also possible to use a damping zone on the free surface. This method consists of adding some extra terms to the free-surface condition which will damp the waves. Because it is very easy to implement this method and because it can absorb waves at a wide frequency range at the same time, we will use it in our model. The extra term that we add to our linear free-surface condition is

$$\nu(x, y) \left(\frac{\partial \phi_u^{(1)}}{\partial t} + \vec{\nabla} \Phi_s \cdot \vec{\nabla} \phi_u^{(1)} \right)$$

In the vicinity of the ship the damping strength, ν , is zero. Near the truncation of the free surface, it should be chosen non-zero. This change in damping strength must go smoothly because a sudden, discontinuous, increase can behave like a rigid wall and may reflect the waves. We therefore choose a linearly-increasing damping strength, ranging from zero at the start of the damping zone to the maximal damping strength at the free-surface truncation. The maximal damping strength depends on the range of frequencies of the waves that must be absorbed and the size of the damping zone.

To obtain a criterion expressing how large the maximal damping strength must be chosen, we look in detail at the Kelvin condition with damping

$$\frac{\partial^2 \phi_u^{(1)}}{\partial t^2} + 2U \frac{\partial^2 \phi_u^{(1)}}{\partial x \partial t} + U^2 \frac{\partial^2 \phi_u^{(1)}}{\partial x^2} + g \frac{\partial \phi_u^{(1)}}{\partial z} + \nu \left(\frac{\partial \phi_u^{(1)}}{\partial t} + U \frac{\partial \phi_u^{(1)}}{\partial x} \right) = 0 \quad \text{on } z = 0$$

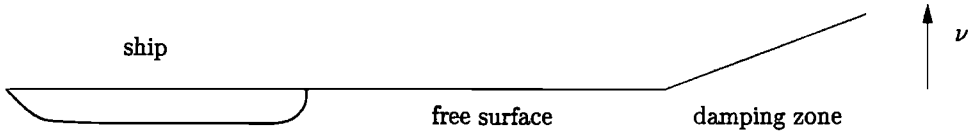


Figure 1.5: Example of linearly-increasing damping strength behind a ship.

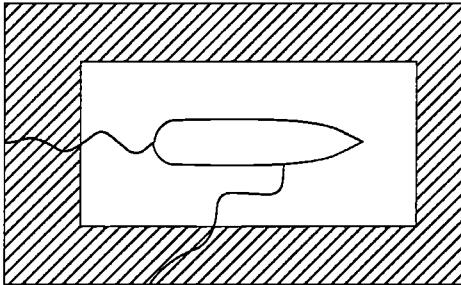


Figure 1.6: Example of the position of the damping zone. The shaded region corresponds to the damping zone, in the white region the damping is zero.

For simplicity we assume that this condition holds for the damping zone, which is allowed because the damping zone is not near the ship. Furthermore, we assume that the water depth is infinite. We consider a surface wave propagating over the free surface according to

$$\phi_u^{(1)} = Ae^{i(\omega t - kx \cos \theta - ky \sin \theta) + kz}$$

The wave must satisfy the free-surface condition, and substituting it leads to a damped version of the dispersion relation

$$-\omega^2 + 2Uk\omega \cos \theta - U^2k^2 \cos^2 \theta + gk + \nu (i\omega - iUk \cos \theta) = 0$$

We assume that frequency, speed, wave angle and damping strength are known and express the wave number k in terms of these quantities. If there is no damping, the solutions of the dispersion relation are

$$k|_{\nu=0} = \begin{cases} \frac{g}{4U^2 \cos^2 \theta} (1 \pm \sqrt{1 + 4\tau \cos \theta})^2 & \text{if } 1 + 4\tau \cos \theta \geq 0, \\ \frac{g}{4U^2 \cos^2 \theta} (1 \pm i\sqrt{-1 - 4\tau \cos \theta})^2 & \text{if } 1 + 4\tau \cos \theta < 0 \end{cases}$$

where $\tau = \frac{\omega U}{g}$. If $1 + 4\tau \cos \theta < 0$ the wave number has a non-zero imaginary part, which means that the waves are evanescent, so no damping is required.

If the damping is non-zero, no simple expression can be found for the wave number, but the solutions look like

$$k = k_r + ik_i$$

where k_r is the real part and k_i the imaginary part of k . The dispersion relation has two solutions. In most cases one solution corresponds to a very short wave, and the other to a longer wave. We will only consider the longer waves, because the short waves damp very fast; the grid size is too large to represent them. When a wave propagates at a wave angle θ in the damping zone over a distance $\sqrt{\Delta x^2 + \Delta y^2}$, where $\tan \theta = \frac{\Delta y}{\Delta x}$, the amplitude of the waves is multiplied by a factor

$$e^{k_i(\Delta x \cos \theta + \Delta y \sin \theta)}$$

So if k_x is negative, the waves are damped. The amount of damping can be enlarged by increasing the size of the damping zone or by enlarging the damping strength in order to decrease k_x . Figure 1.6 shows that damping zones may exist in front of, along the sides of and behind the ship. In most of our calculations, the speed of the flow and the encounter frequency of the incoming waves are high enough to ensure that waves can only propagate in downstream direction, which implies that the damping zones in front of and behind the ship are redundant. We therefore look more in detail at the damping zone along the sides of the ship. We consider a damping zone of infinite length and width B like the one shown in figure 1.7. The damping strength ν is taken to be constant (the average value of the linearly-increasing damping strength) for simplicity, because this is the only way we can make a statement about the amount of damping. A wave with wave angle θ that enters this damping zone will travel through it over a distance $\frac{B}{\sin \theta}$. This means that waves with wave angles close to zero are damped well because they spend a long time in the damping zone.

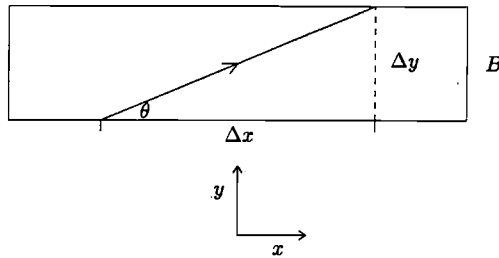


Figure 1.7: Example of infinitely-long damping zone with width B .

Figure 1.8 shows the amount of damping for downstream waves at Froude number 0.2 and $\tau = 1$ if the damping strength $\nu = 6$ and the width of the damping zone B is half a ship's length. The Froude number is defined as $Fn = \frac{U}{\sqrt{gL}}$. As can be seen, the wave at wave angle $\theta \approx 0.9$ is damped the least, but still for almost 90 percent. Waves at wave angles which are almost zero are damped nearly completely, as expected.

We can now try to find the smallest value of ν , for fixed Froude number and fixed τ , where all the waves are damped for at least 90 percent. If we do this for a range of τ -values and several Froude numbers, we obtain the 90-percent curves, which are shown in figure 1.9. It shows that most damping is required for low-frequency waves. This is because low-frequency waves are longer than high-frequency waves, so they have to be damped in an area which is small compared to their wavelength. It is therefore expected that in this low-frequency region the damping zone is not very effective. This can be solved by enlarging the width of the damping zone, but this increases the number of panels and therefore the computational time. Figure 1.9 also shows that the higher the Froude number, the more damping is required. Finally, we may conclude that for values of τ larger than one, this method can be applied without problems. Below that value, the method should be used with care, because the large damping strength may cause the damping zone to act like a wall that reflects the waves instead of absorbing them.

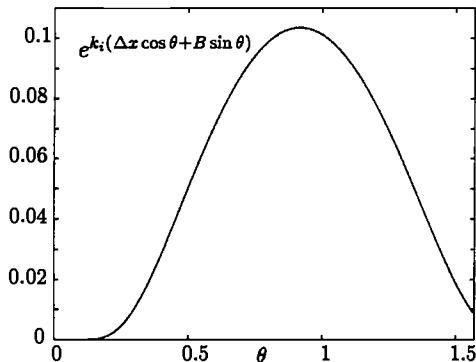


Figure 1.8: Amount of damping for downstream wave angles, $B = 0.5L$, $\nu = 6$ and $Fn = 0.2$.

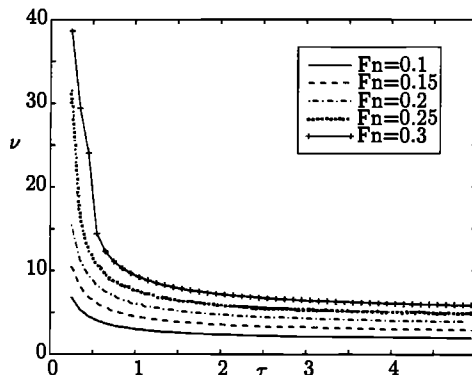


Figure 1.9: 90-percent damping curves for increasing τ and several Froude numbers.

1.6 Forces and moments

The mathematical model is developed to obtain an estimation of the forces and moments on the ship and the subsequent motions. Because the water is assumed to be inviscid, the only forces in our model are pressure forces. They can be obtained by integrating the pressure over the wetted surface of the ship

$$\vec{F} = \iint_H p \vec{n} dS \quad \vec{M} = \iint_H p (\vec{x} - \vec{x}_g) \times \vec{n} dS \quad (1.16)$$

where \vec{n} is the unit normal vector, directed into the ship. Due to the linearization, only the pressure on the mean position of the hull is known, and the wetted part of the hull is unknown. Therefore, to evaluate (1.16) we need perturbation theory. We follow the method outlined by Pinkster [27] and extended by Prins [28], who showed that the expression for the forces and moments can be perturbed into

$$\vec{F} = \vec{F}_s + \epsilon \vec{F}_u^{(1)} + \epsilon^2 \vec{F}_u^{(2)} + \dots \quad \text{and} \quad \vec{M} = \epsilon \vec{M}_u^{(1)} + \epsilon^2 \vec{M}_u^{(2)} + \dots$$

where all contributions can be calculated by evaluating the flow quantities on the mean position of the hull. Prins neglected contributions of second and higher order in the ship's velocity when deriving formulas for the first- and second-order forces and moments. He could do this, because he only considered ships sailing with a small forward speed. Because we do not make this assumption, we have to reformulate the perturbed expressions for the forces and moments.

First we have to express the pressure on the actual position of the hull in terms of the pressure on the mean position of the hull. Because the motion of the ship is assumed to

be small, the pressure can be expanded in a Taylor series around the mean position of the ship, \bar{H}

$$p_H = p_{\bar{H}} + \bar{\alpha} \cdot \bar{\nabla} p_{\bar{H}} + \frac{1}{2} (\bar{\alpha} \cdot \bar{\nabla})^2 p_{\bar{H}} + \mathcal{O}(|\bar{\alpha}|^3) \quad (1.17)$$

The integral over the wetted part of the hull can be estimated by an integral over the mean wetted surface and an oscillatory disturbance of it. For the force this becomes

$$\bar{F} = \iint_H p \bar{n} dS = \iint_{\bar{H}} p \bar{n} dS + \iint_{H_{osc}} p \bar{n} dS \approx \iint_{\bar{H}} p \bar{n} dS + \int_{wl} \int_{\zeta_s + \alpha_3}^{\zeta} p \bar{n} dz dl \quad (1.18)$$

The oscillatory part of the wetted surface is estimated by the difference between the unsteady wave elevation on the waterline of the ship and the vertical motion of the ship.

We now perturb all flow quantities using the small parameter ϵ , as we did for the potential

$$\begin{aligned} \Phi &= \Phi_s + \epsilon \phi_u^{(1)} + \epsilon^2 \phi_u^{(2)} + \mathcal{O}(\epsilon^3) \\ \zeta &= \zeta_s + \epsilon \zeta_u^{(1)} + \epsilon^2 \zeta_u^{(2)} + \mathcal{O}(\epsilon^3) \\ p_{\bar{H}} &= p_s + \epsilon p_u^{(1)} + \epsilon^2 p_u^{(2)} + \mathcal{O}(\epsilon^3) \\ \bar{X} &= \epsilon \bar{X}^{(1)} + \epsilon^2 \bar{X}^{(2)} + \mathcal{O}(\epsilon^3) \\ \bar{\Omega} &= \epsilon \bar{\Omega}^{(1)} + \epsilon^2 \bar{\Omega}^{(2)} + \mathcal{O}(\epsilon^3) \\ \bar{x} - \bar{x}_g &= \bar{x} - \bar{x}_g + \epsilon \bar{\Omega}^{(1)} \times (\bar{x} - \bar{x}_g) + \epsilon^2 \bar{\Omega}^{(2)} \times (\bar{x} - \bar{x}_g) + \mathcal{O}(\epsilon^3) \\ \bar{\alpha} &= \epsilon \bar{\alpha}^{(1)} + \epsilon^2 \bar{\alpha}^{(2)} + \mathcal{O}(\epsilon^3) \\ \bar{n} &= \bar{n} + \epsilon \bar{\Omega}^{(1)} \times \bar{n} + \epsilon^2 \bar{\Omega}^{(2)} \times \bar{n} + \mathcal{O}(\epsilon^3) \end{aligned}$$

The perturbation series for the pressure and the displacement can be substituted into (1.17), after which the components of the perturbation series for the pressure on the exact position of the hull can be retrieved by collecting equal powers of ϵ

$$\begin{aligned} p_{H_s} &= p_s \\ p_{H_u}^{(1)} &= p_u^{(1)} + \bar{\alpha}^{(1)} \cdot \bar{\nabla} p_s \\ p_{H_u}^{(2)} &= p_u^{(2)} + \bar{\alpha}^{(2)} \cdot \bar{\nabla} p_s + \bar{\alpha}^{(1)} \cdot \bar{\nabla} p_u^{(1)} + \frac{1}{2} (\bar{\alpha}^{(1)} \cdot \bar{\nabla})^2 p_s \end{aligned}$$

The components of the perturbation series of the pressure on the mean position of the ship follow from Bernoulli

$$\begin{aligned} p_s &= -\rho \left(gz + \frac{1}{2} \bar{\nabla} \Phi_s \cdot \bar{\nabla} \Phi_s - \frac{1}{2} U^2 \right) \\ p_u^{(1)} &= -\rho \left(\bar{\nabla} \Phi_s \cdot \bar{\nabla} \phi_u^{(1)} + \frac{\partial \phi_u^{(1)}}{\partial t} \right) \\ p_u^{(2)} &= -\rho \left(\frac{\partial \phi_u^{(2)}}{\partial t} + \frac{1}{2} \bar{\nabla} \phi_u^{(1)} \cdot \bar{\nabla} \phi_u^{(1)} + \bar{\nabla} \Phi_s \cdot \bar{\nabla} \phi_u^{(2)} \right) \end{aligned}$$

When we substitute this perturbation series into (1.18), we obtain an expression for the force on the exact position on the hull in terms of flow quantities on the mean position of the hull. The same can be done for the moments of course. By collecting powers of ϵ , we can find expressions for the steady, the first, and the second-order forces and moments.

1.6.1 Steady forces and moments

The steady forces and moments are given by

$$\vec{F}_s = \iint_{\bar{H}} p_{H_s} \bar{n} dS = \begin{pmatrix} R_w \\ 0 \\ mg \end{pmatrix} \quad \vec{M}_s = \iint_{\bar{H}} p_{H_s} (\bar{x} - \bar{x}_g) \times \bar{n} dS = \begin{pmatrix} 0 \\ 0 \\ 0 \end{pmatrix}$$

R_w is the wave resistance due to the steady forward speed of the ship, which is balanced by the propulsive force of the ship. The vertical pressure force on the ship is balanced by the gravitational force on the ship's mass. According to Archimedes' law, this force also equals the gravitational force on the mass of the displaced water, so $m = \rho\Delta$, where Δ is the volume of the ship below the steady waterline. The steady moment is zero, because the ship is in equilibrium. If the steady moment would be non-zero, a change in dynamic trim and sinkage would see to it that the equilibrium position is reached.

1.6.2 First-order forces and ship motions

The first-order contributions for the forces and moments are given by

$$\begin{aligned} \vec{F}_u^{(1)} = \iint_{\bar{H}} (p_{H_u}^{(1)} \bar{n} + p_{H_s} \bar{n}_u^{(1)}) dS = -\rho \iint_{\bar{H}} \left(\frac{\partial \phi_u^{(1)}}{\partial t} + \bar{\nabla} \Phi_s \cdot \bar{\nabla} \phi_u^{(1)} \right) \bar{n} dS + \\ \iint_{\bar{H}} \left(p_s \bar{\Omega}^{(1)} \times \bar{n} + \left(\bar{X}^{(1)} + \bar{\Omega}^{(1)} \times (\bar{x} - \bar{x}_g) \right) \cdot \bar{\nabla} p_s \bar{n} \right) dS \quad (1.19) \end{aligned}$$

$$\begin{aligned} \vec{M}_u^{(1)} = \iint_{\bar{H}} \left(p_{H_u}^{(1)} (\bar{x} - \bar{x}_g) \times \bar{n} + p_{H_s} \bar{\Omega}^{(1)} \times ((\bar{x} - \bar{x}_g) \times \bar{n}) \right) dS = \\ -\rho \iint_{\bar{H}} \left(\bar{\nabla} \Phi_s \cdot \bar{\nabla} \phi_u^{(1)} + \frac{\partial \phi_u^{(1)}}{\partial t} \right) (\bar{x} - \bar{x}_g) \times \bar{n} dS + \\ \bar{\Omega}^{(1)} \times \vec{M}_s + \iint_{\bar{H}} \left(\bar{X}^{(1)} + \bar{\Omega}^{(1)} \times (\bar{x} - \bar{x}_g) \right) \cdot \bar{\nabla} p_s (\bar{x} - \bar{x}_g) \times \bar{n} dS \quad (1.20) \end{aligned}$$

Note that the contribution containing the steady moment is zero because the ship is in equilibrium. These first-order forces and moments will cause the ship to carry out a first-order rotational and translational motion. This motion is described by Newton's second

law

$$\mathbf{M} \frac{\partial^2 \vec{Y}}{\partial t^2} = \begin{pmatrix} \vec{F}_u^{(1)} \\ \vec{M}_u^{(1)} \end{pmatrix} \quad (1.21)$$

where $\vec{Y} = (X_1^{(1)}, X_2^{(1)}, X_3^{(1)}, \Omega_1^{(1)}, \Omega_2^{(1)}, \Omega_3^{(1)})^T$ is a vector containing the first-order translations and rotations. \mathbf{M} is the mass matrix containing the mass of the ship and the moments of inertia. The forces and moments also depend on the motion, as can be seen in (1.19) and (1.20). A part of them depends directly on the motion, the so-called restoring forces and moments. This motion dependence can be compared with the motion of a mass connected to a string, where the restoring force on the mass is proportional to the displacement of the mass. In order to remove all motion dependencies from the forces, we shift these restoring forces and moments to the left-hand side of (1.21), so they become part of the differential equation. We do this by using restoring-force coefficients $C_{i,j}$, which are defined in the following way

$$\begin{pmatrix} \vec{F}_r \\ \vec{M}_r \end{pmatrix} = -\mathbf{C}\vec{Y}$$

where \mathbf{C} is a 6×6 matrix containing the restoring-force coefficients. The separate entries in this matrix can be obtained by choosing all the entries, but one, in the motion vector \vec{Y} zero, and by calculating the correspondent restoring forces and moments. The resulting coefficients are listed in Appendix A. A part of the first-order forces depends directly on the first-order potential. Implicitly, this part depends on the motion of the ship as well. This can be observed by looking at the hull boundary condition (1.3), that relates the normal fluid velocity at the hull to the motions of the ship. In order to solve the motions of the ship, this dependency has to be removed. We do this by giving the ship a fixed motion in one translational or rotational direction at a certain frequency and by calculating the resulting hydrodynamic first-order forces. These forces now completely depend on the motion of the ship and can be related by using added mass and damping coefficients

$$F_{ij} = -A_{ij} \frac{\partial^2 Y_j}{\partial t^2} - B_{ij} \frac{\partial Y_j}{\partial t}$$

where i is the direction of the force and j the direction of the motion. The same can be done for the moments, of course. The damping coefficients correspond to the part of the force which is out of phase with the motion, while the added-mass coefficients correspond to the part of the force that is in phase with the motion. The damping term is uniquely determined, while the added-mass coefficients could be taken as part of the restoring-force coefficients, because both coefficients correspond to the in-phase part of the force. This is not done because the restoring-force coefficients are independent of frequency while the added-mass coefficients are not. Now, all motion dependence has been removed from the forces and moments and the equation of motion (1.21) can be rewritten into

$$(\mathbf{M} + \mathbf{A}) \frac{\partial^2 \vec{Y}}{\partial t^2} + \mathbf{B} \frac{\partial \vec{Y}}{\partial t} + \mathbf{C}\vec{Y} = \begin{pmatrix} \vec{F}_{inc} \\ \vec{M}_{inc} \end{pmatrix} \quad (1.22)$$

The only remaining force in the equation of motion is the force due to incoming waves. Solving this equation involves three separate simulations. First a simulation has to be run in which the added-mass and damping coefficients are calculated. This means the ship is given a motion while no incoming waves are considered. Second, incoming waves are taken into account without any ship motions, from which the forces and moments in (1.22) can be calculated. Third, the equation of motion can be solved and the simulation has to be run one more time to obtain the fluid characteristics with incoming waves and ship motions. The disadvantage of equation (1.22) is that it is a frequency-dependent equation, which means that the incoming-wave force may only contain one frequency at a time. In a realistic sea state this of course never happens. This can be overcome by using an equation of motion that is independent of frequency, derived by Ogilvie [26]

$$(\mathbf{M} + \overline{\mathbf{A}}) \frac{\partial^2 \vec{Y}}{\partial t^2} + \overline{\mathbf{B}} \frac{\partial \vec{Y}}{\partial t} + \mathbf{C} \vec{Y} + \int_0^t \mathbf{K}(t-s) \frac{\partial \vec{Y}}{\partial s}(s) ds = \begin{pmatrix} \vec{F}_{inc} \\ \vec{M}_{inc} \end{pmatrix} \quad (1.23)$$

In this equation $\mathbf{K}(t)$ is the step-response matrix, which entries are the step-response functions K_{ij} . These are oscillating, rapidly-decaying functions which account for the memory part of the equation of motion. The relations between the frequency-dependent added-mass and damping coefficients and the step-response functions are

$$\mathbf{A}(\omega) = \overline{\mathbf{A}} - \frac{1}{\omega} \int_0^{\infty} \mathbf{K}(t) \sin(\omega t) dt \quad \mathbf{B}(\omega) = \overline{\mathbf{B}} + \int_0^{\infty} \mathbf{K}(t) \cos(\omega t) dt \quad (1.24)$$

$$\mathbf{K}(t) = \frac{2}{\pi} \int_0^{\infty} (\mathbf{B}(\omega) - \overline{\mathbf{B}}) \cos(\omega t) d\omega \quad (1.25)$$

which follow immediately from applying the Fourier transform to (1.23). Although these step-response functions are not used in any of the calculations in this thesis, they can easily be programmed to simulate random seas. The step-response functions can be determined with a method developed by Prins [28], who matched them with Laguerre polynomials, but it is not certain that this method can also be used for moderate and high speeds. In that case, they have to be determined by calculating the frequency-dependent damping coefficients, and by substituting these in equation (1.25).

1.6.3 Second-order forces and moments

The first-order forces are harmonic if the incoming waves are harmonic, so these forces have a mean value which is zero. The drifting of a ship can therefore only be explained by the existence of second-order forces. These forces contain products of first-order quantities and have a mean value which is non-zero. The second-order contributions in our perturbation series for the forces are

$$\vec{F}^{(2)} = \iint_{\overline{H}} (p_{H_s} \vec{n}_u^{(2)} + p_{H_u}^{(1)} \vec{n}_u^{(1)} + p_{H_u}^{(2)} \vec{n} dS) + \frac{1}{\epsilon^2} \int_{\omega t}^{\zeta_s + \epsilon \zeta_u^{(1)}} \int_{\zeta_s + \epsilon \alpha_3^{(1)}} (p_s + \epsilon p_u^{(1)}) \vec{n} dz dl$$

Since we only want to know the average value of these forces, we leave out the terms that have zero mean value. This leads to

$$\begin{aligned} \langle \bar{F}^{(2)} \rangle = & \left\langle -\frac{1}{2}\rho \iint_{\bar{H}} \bar{\nabla} \phi_u^{(1)} \cdot \bar{\nabla} \phi_u^{(1)} \bar{n} dS + \iint_{\bar{H}} \left(\bar{\Omega}^{(1)} \times \left(\bar{\Omega}^{(1)} \times (\bar{x} - \bar{x}_g) \right) \right) \cdot \bar{\nabla} p_s \bar{n} dS \right. \\ & - \rho \iint_{\bar{H}} \left(\bar{\alpha}^{(1)} \cdot \bar{\nabla} \right) \left(\bar{\nabla} \Phi_s \cdot \bar{\nabla} \phi_u^{(1)} + \frac{\partial \phi_u^{(1)}}{\partial t} \right) \bar{n} dS + \bar{\Omega}^{(1)} \times \left(M \frac{\partial^2 \bar{X}^{(1)}}{\partial t^2} \right) \\ & \left. + \rho g \int_{wl} \zeta_u^{(1)} \left(\zeta_u^{(1)} - \alpha_3^{(1)} \right) \bar{n} dl + \frac{1}{2} \int_{wl} \frac{\partial p_s}{\partial z} \Big|_{z=\zeta_s} \left(\zeta_u^{(1)2} - \alpha_3^{(1)2} \right) \bar{n} dl \right\rangle \quad (1.26) \end{aligned}$$

The waterline integral is derived by expanding the steady pressure in a Taylor series around the steady free surface

$$p_s = p_s|_{z=\zeta_s} + (z - \zeta_s) \frac{\partial p_s}{\partial z} \Big|_{z=\zeta_s} + \mathcal{O}((z - \zeta_s)^2)$$

Because the steady pressure is zero on the steady free surface, a first-order expression remains. If we furthermore realize that $p_u^{(1)} = \rho g \zeta_u^{(1)}$, the second-order expression in (1.26) is obtained.

The same can be done for the moments, which results in

$$\begin{aligned} \langle \bar{M}^{(2)} \rangle = & \left\langle \iint_{\bar{H}} p_s \left(\left(\bar{\Omega}^{(1)} \times (\bar{x} - \bar{x}_g) \right) \times \left(\bar{\Omega}^{(1)} \times \bar{n} \right) - \bar{\Omega}^{(1)} \times \left(\bar{\Omega}^{(1)} \times ((\bar{x} - \bar{x}_g) \times \bar{n}) \right) \right) dS \right. \\ & - \frac{1}{2}\rho \iint_{\bar{H}} \bar{\nabla} \phi_u^{(1)} \cdot \bar{\nabla} \phi_u^{(1)} (\bar{x} - \bar{x}_g) \times \bar{n} dS + \iint_{\bar{H}} \left(\bar{\Omega}^{(1)} \times \left(\bar{\Omega}^{(1)} \times (\bar{x} - \bar{x}_g) \right) \right) \cdot \bar{\nabla} p_s (\bar{x} - \bar{x}_g) \times \bar{n} dS \\ & - \rho \iint_{\bar{H}} \left(\bar{\alpha}^{(1)} \cdot \bar{\nabla} \right) \left(\frac{\partial \phi_u^{(1)}}{\partial t} + \bar{\nabla} \Phi_s \cdot \bar{\nabla} \phi_u^{(1)} \right) (\bar{x} - \bar{x}_g) \times \bar{n} dS + \bar{\Omega}^{(1)} \times \left(M \frac{\partial^2 \bar{\Omega}^{(1)}}{\partial t^2} \right) \\ & \left. + \rho g \int_{wl} \zeta_u^{(1)} \left(\zeta_u^{(1)} - \alpha_3^{(1)} \right) (\bar{x} - \bar{x}_g) \times \bar{n} dl + \frac{1}{2} \int_{wl} \frac{\partial p_s}{\partial z} \Big|_{z=\zeta_s} \left(\zeta_u^{(1)2} - \alpha_3^{(1)2} \right) (\bar{x} - \bar{x}_g) \times \bar{n} dl \right\rangle \end{aligned}$$

We see that to determine the average value of the second-order forces and moments, we only have to solve first-order quantities. Therefore, from now on, we drop the superscript '1' in these quantities, and also the subscript u if it is obvious that an unsteady quantity is involved. So $\phi_u^{(1)}$ becomes ϕ , $\Omega^{(1)}$ becomes Ω , $\zeta_u^{(1)}$ becomes ζ_u etcetera.

1.7 Solving the Laplace equation

There are a number of ways to solve the Laplace equation in the fluid domain. Mostly boundary-integral methods are used, but finite-element, finite-volume and finite-difference

methods can be used as well. These field methods have the disadvantage that it can be quite difficult to generate their three-dimensional grid, especially near curving boundaries like the free surface, or the hull of the ship. Grid generation for the boundary-integral method is very easy, because only the boundaries of the fluid domain have to be discretized. The disadvantage is, however, that difficult integrals of the Green function have to be evaluated. Fortunately, this evaluation has already been done in the past by other researchers working with boundary-integral methods. Still, it takes a lot of time to determine all these integrals on a computer. The computational time required to solve the system of equations obtained by field methods is larger than the time required to solve the system of equations obtained by a boundary-integral method. The boundary-integral method requires more memory, however, as shown by Raven [29]. Because we develop a time-domain code, the time aspect is more important than the memory aspect.

For these reasons we choose a boundary-integral method, which is based on Green's second identity, to solve Laplace's equation. We apply Green's second identity to the velocity potential ϕ in the fluid domain Ω with boundary $\partial\Omega$ and the following Green function

$$G(\vec{x}, \vec{\xi}) = -\frac{1}{4\pi r} - \frac{1}{4\pi r'} \quad r = |\vec{x} - \vec{\xi}| \quad r' = |\vec{x} - \vec{\xi}'|$$

where $\vec{\xi}'$ is the mirror image of ξ with respect to the bottom, B . This Green function satisfies the bottom boundary condition, which implies that we do not have to distribute sources on the bottom. After applying Green's identity we find

$$T\phi(\vec{x}) = \iint_{\partial\Omega \setminus B} \left(\frac{\partial\phi}{\partial n_\xi}(\vec{\xi}) G(\vec{x}, \vec{\xi}) - \phi(\vec{\xi}) \frac{\partial G}{\partial n_\xi}(\vec{x}, \vec{\xi}) \right) dS_\xi \quad (1.27)$$

where

$$T = \begin{cases} 1 & \text{if } \vec{x} \in \Omega \setminus \partial\Omega \text{ or } \vec{x} \in B \\ \frac{1}{2} & \text{if } \vec{x} \in \partial\Omega \setminus B \\ 0 & \text{if } \vec{x} \notin \Omega \end{cases}$$

We assume that in the second case, \vec{x} is on a smooth part of the boundary; otherwise the factor $\frac{1}{2}$ changes, depending on the local space angle of the boundary. The normal in (1.27) is pointing into the fluid domain. Therefore, some care must be taken when we calculate the forces and moments on the ship. In that case we have to use the normal pointing into the ship, so out of the fluid domain. Because Green's identity must be applied to a closed boundary, the integral in (1.27) is not only over the free surface and the hull, but also over a boundary at infinity that connects the free surface and the bottom as can be seen in figure 1.10. The integral over the last boundary vanishes if the potential is only the perturbation of the incoming potential, because according to Prins [28] the asymptotic behaviour of the potential is of $\mathcal{O}\left(\frac{1}{\sqrt{r}}\right)$. The integral equation can be solved by prescribing the potential, its normal derivative, or a linear combination of both in a finite number of collocation points on the boundary. The relation between the potential and its normal derivative is given by the boundary conditions. A set of linear equations is

then found for the potential or its normal derivative, which can be solved with standard numerical techniques.

To obtain the pressure distribution on the hull, the velocity must be determined, which might be done by numerical differentiation of the potential. Because this easily leads to errors at curved parts of the hull, we decided to use another boundary-integral formulation from which derivatives can be calculated directly.

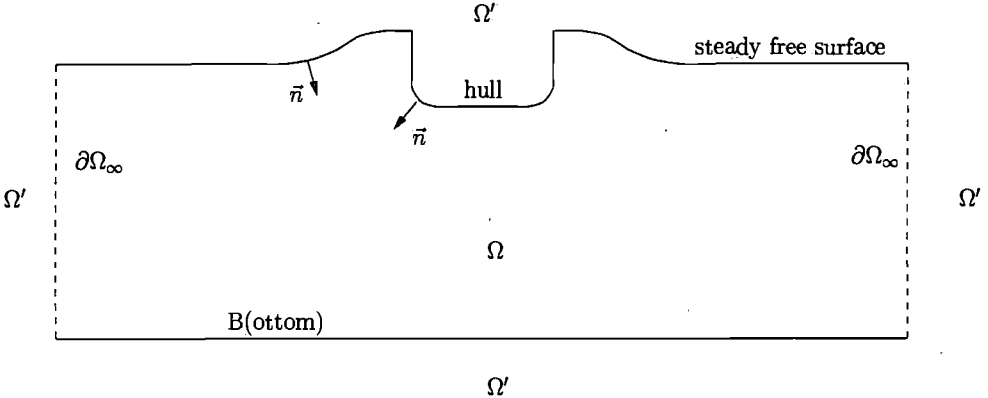


Figure 1.10: Cross section of fluid domain and boundaries used in Green's theorem.

We suppose a potential field ϕ' exists in a virtual domain Ω' above the free surface, inside the hull and below the bottom. This domain is bounded by the boundaries of Ω and by boundaries at infinity. If we apply Green's theorem to this virtual domain we obtain

$$T' \phi'(\vec{x}) = - \iint_{\partial\Omega \setminus B} \left(\frac{\partial \phi'}{\partial n_\xi}(\vec{\xi}) G(\vec{x}, \vec{\xi}) - \phi'(\vec{\xi}) \frac{\partial G}{\partial n_\xi}(\vec{x}, \vec{\xi}) \right) dS_\xi$$

where

$$T' = \begin{cases} 1 & \text{if } \vec{x} \in \Omega' \setminus \partial\Omega \text{ or } \vec{x} \in B \\ \frac{1}{2} & \text{if } \vec{x} \in \partial\Omega \setminus B \\ 0 & \text{if } \vec{x} \notin \Omega' \end{cases}$$

The minus sign occurs because the inner normal in the virtual domain is minus the inner normal in the fluid domain. The integrals over boundaries at infinity disappear again, and when we add this equation to equation (1.27) we find

$$T\phi + T'\phi' = \iint_{\partial\Omega \setminus B} \left(\left(\frac{\partial \phi}{\partial n_\xi} - \frac{\partial \phi'}{\partial n_\xi} \right) G - (\phi - \phi') \frac{\partial G}{\partial n_\xi} \right) dS_\xi$$

Because Ω' is a virtual domain, we can choose any boundary condition we want. If we choose $\phi' = \phi$ on the boundary $\partial\Omega$, the only contribution in the boundary integral comes

from the jump in the normal velocity, $\sigma = \frac{\partial\phi}{\partial n_\xi} - \frac{\partial\phi'}{\partial n_\xi}$, resulting in a source-only formulation. It is also possible to use a dipole distribution on the boundaries but then, the influence coefficients that are involved are more difficult to determine. An advantage of the use of dipoles is that lifting surfaces can be modeled, but these are not considered in this thesis. The same can be done to derive an integral equation for the velocity. If \vec{x} is inside the fluid domain, on the hull, or on the free surface, this results in

$$\phi(\vec{x}) = \iint_{\partial\Omega \setminus B} \sigma(\vec{\xi}) G(\vec{x}, \vec{\xi}) dS_\xi \quad (1.28)$$

$$\vec{\nabla}\phi(\vec{x}) = (1 - T)\sigma(\vec{x})\vec{n} + \iint_{\partial\Omega \setminus B} \sigma(\vec{\xi}) \vec{\nabla}_{\vec{x}}G(\vec{x}, \vec{\xi}) dS_\xi \quad (1.29)$$

So when the source strength is known, the velocities can be computed directly. A disadvantage of this approach is that $3N_{fs}N_h$ extra influence coefficients have to be calculated, where N_{fs} is the number of panels on the free surface and N_h the number of panels on the hull. Furthermore, these coefficients have to be stored in the computer's memory, because the pressure on the hull must be evaluated in each time step.

Chapter 2

Numerical formulation

In this chapter we discretize the mathematical model that we derived in chapter 1. A panel method is used to discretize the boundary integral, and difference schemes are used to discretize the tangential space derivatives and the time derivatives in the free-surface condition. Difference schemes are introduced to obtain derivatives of the steady velocities on the free surface and on the hull. The velocity potential is split in a symmetrical and an asymmetrical part, and calculated separately using symmetry relations. Finally, an outline is given of the parallelization of the computer code.

2.1 Introduction

With analytical methods, a solution of the model that was presented in the previous chapter cannot be found. Therefore, it is necessary to construct a numerical approximation of this solution that must be as close as possible to it. To accomplish this, we have to discretize the integral equation and the boundary conditions.

We use a first-order panel method to discretize the boundary integral. This means that we divide the boundaries into small quadrilateral panels with constant source strength. The free-surface boundary condition contains tangential space derivatives and time derivatives. The tangential space derivatives are discretized with upwind difference schemes to guarantee numerical stability. The space derivatives in the normal direction can be obtained directly from the integral equation. The time derivatives are obtained with backward difference schemes that relate the potential at a certain time level to the potential at previous time levels, so we have to recalculate the potential on each time level in a time-stepping procedure. It is also possible to use a frequency-domain approach. In that case, the wave pattern is assumed to be harmonic in time at a certain frequency, and no time stepping is required. A disadvantage, however, is that waves, oscillating at more than one frequency at a time cannot be simulated. It is well known that incoming waves with several frequencies cause slowly varying drift forces. The low-frequency part of these drift forces causes large ship motions if this low frequency is near the resonance frequency of the ship. Another disadvantage is that frequency-domain models are not suitable for modeling non-linear effects. If we use a time-domain model, we may be able to extend our

model to a non-linear one sometime in the future, when computer power has increased sufficiently.

The discrete boundary conditions are applied to a set of collocation points. This leads to a set of equations for the source strengths, which we solve in each time step with Gaussian elimination. The number of panels has to be as small as possible, because the computing time is of third order in the number of panels. To accomplish this we make use of symmetry relations. We split up the wave pattern in a symmetrical and an asymmetrical part and calculate both parts separately by using mirror sources. Although the simulation has to be run twice now, the total simulation time will decrease because the number of panels is reduced by a factor 2.

We used this numerical model to write a computer program that simulates the motions of and calculates the forces on a ship sailing in waves. To save time, and to make efficient use of memory, we wrote a parallel computer code, using the PVM package.

2.2 Discretization of the boundary integral

The discretization of the boundary integral consists of two parts. First, we have to divide a part of the steady free surface and the entire hull into panels. Second, we have to choose a certain shape for the source function σ . This can be done in a number of ways, ranging from a very simple first-order approximation of flat panels and constant sources on each panel, to a higher-order approximation that, for example, uses splines to describe the geometry of a panel and the shape of the source function. A first-order approximation leads to a relatively easy evaluation of influence coefficients, and to a number of unknown source strengths that equals the number of panels. A higher-order approximation leads to a more difficult evaluation of the influence coefficients, and to a larger number of unknowns per panel. Although the panels can be taken larger due to the higher accuracy, this mostly increases the size of the leading matrix.

We use a linearization method in which the non-linear steady flow is used to approximate the unsteady flow. The non-linear steady flow is calculated by RAPID with a first-order panel method, so the steady velocities may contain first-order errors, and derivatives of velocities errors of even lower order. It is impossible to get a higher accuracy for the unsteady flow, because the inaccuracies in the steady flow affect the unsteady solution as well. Therefore, we will use a first-order panel method in our model. If RAPID would have used a higher-order method, or if we would have used a non-linear approach instead of a linearization about a steady base flow, it would have been worthwhile to use a higher-order panel method. Especially in non-linear methods, where waves can get close to breaking, it is recommended to use a higher-order panel method.

Several authors, for example Bertram [4], Nakos [24], Prins [28] and van 't Veer [36], also used first-order panel methods to solve diffraction problems, and got good agreement between their calculations and measurements. Our decision to use a first-order panel method is therefore not only based on restrictions due to the linearization, but also on

some very promising results from the recent past.

We assume that each panel consists of two flat triangles, forming a quadrilateral, which allows us to use non-flat panels. With non-flat panels, curved parts of the boundary can easier be discretized. This is important, because the steady free surface as well as the hull have curved parts. The normal on a panel, however, is not uniquely determined if the panel is not flat. We therefore define the average normal on a panel to be the normalized outer product of the two diagonals of the quadrilateral panel. One of these diagonals may not be inside the panel, as illustrated in figure 2.1. The steady free surface

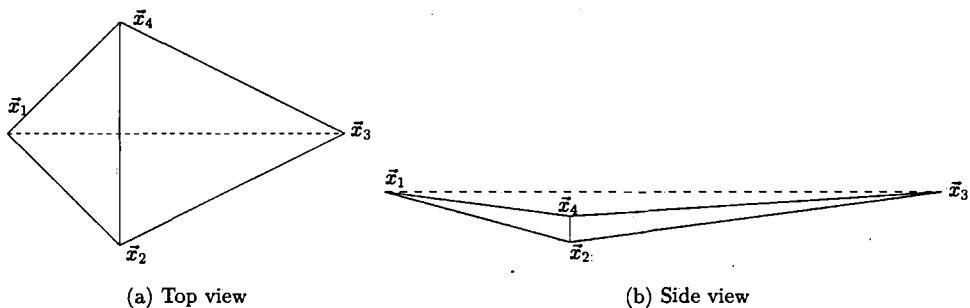


Figure 2.1: Top view and side view of a quadrilateral panel consisting of two triangles. The diagonals are used to determine the average normal.

is divided into a number of these panels. Because we use an artificial-damping zone, outgoing waves are damped and will vanish, so we only have to use a small part of the free surface near the ship, which we will refer to as the computational free surface. The size of the computational free surface depends on the length of the unsteady waves. If the frequency of the waves and the speed of a ship is such that $\tau > 0.25$, waves do not propagate in upstream direction. In that case only a small part of the free surface on the upstream side of the ship has to be taken into account. Otherwise, a damping zone is required, the length of which depends on the length of the upstream waves.

On the downstream side of the ship, the size of the computational free surface depends on the length of the downstream waves. If $\tau > 0.25$, this size can be chosen quite small, because waves that reflect against the free-surface truncation behind the ship cannot propagate back to the ship, so in this case no damping zone behind the ship is needed. If $\tau < 0.25$, this size must be chosen in the order of the largest wavelength, and some artificial damping must be added to the free-surface condition. Along the side of the ship, the size of the computational free surface should be chosen in the order of the length of one transverse wave, and artificial damping should always be added to the free-surface condition in that area. Of course, we must realize that the wavelength depends on the direction of propagation, so longitudinal waves have a length that differs from the length of transverse waves.

A typical example of a free-surface grid is shown in figure 2.2. As can be seen, we use a

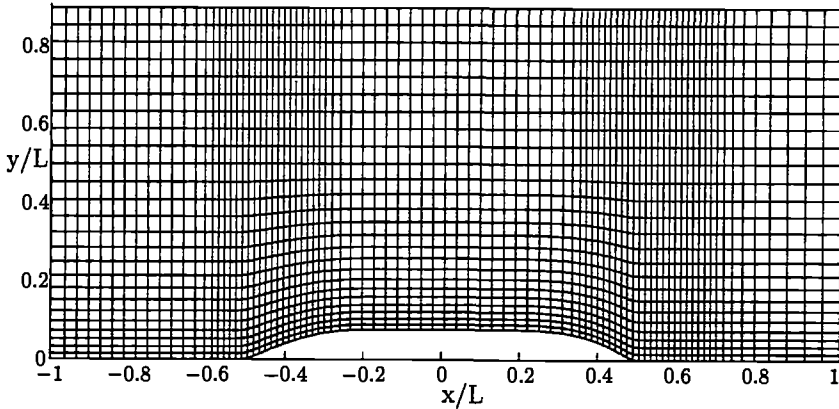


Figure 2.2: Example of free-surface grid in our code.

grid that approximately follows the streamlines of the steady flow. This makes it easier to obtain derivatives in the direction of the steady flow, as we shall see later. The grid size in the y -direction is small near the ship, and relatively large further away from the ship, because accuracy is less important there. The quotient of the largest and smallest panel size is about a factor 3. In the x -direction, the grid size is small near the bow and the stern of the ship, and somewhat larger in the midship region, in front of the ship, and behind the ship. The reason for this is that near the bow and the stern, the gradients of the fluid velocity are expected to be largest.

Like the free surface, the hull is also divided into panels. We use a structured grid in our calculations. This means that the hull is divided into segments along the x -axis, and each segment is divided into the same number of panels. The panel corners coincide with panel corners of adjacent segments. This makes it easier to find the nearest panels, which are required to obtain the derivatives of velocities on the hull. The size of the panels must be such that even the smallest waves we are interested in can be represented on them. In general, the size of the panels on the bow and on the stern will be smaller than in the midship region, because the gradients of the fluid velocity are expected to be largest near the bow and the stern.

Now that the free surface and hull have been divided into panels, we can discretize the source function σ on these panels. The simplest option is to assume that it has constant strength per panel. The boundary integral for the potential (1.28) then turns into a sum over all panels, of source strength times an influence coefficient $G_{i,j}$. If we have N panels on the hull and free surface together, the potential in a collocation point \vec{x}_i becomes

$$\phi(\vec{x}_i) = \sum_{j=1}^N \sigma_j \iint_{\partial\Omega_j} G(\vec{x}_i, \vec{\xi}) dS_{\xi} = \sum_{j=1}^N \sigma_j G_{i,j} \quad (2.1)$$

When the collocation point and the panel are close to each other, the influence coefficients $G_{i,j}$ are calculated with analytical formulas listed by Prins [28]. When the distance between the collocation point and the panel is large, these coefficients are calculated numerically. The same procedure can be applied to discretize the boundary integral for the velocity (1.29)

$$\vec{\nabla}\phi(\vec{x}_i) = (1-T)\sigma_i\vec{n} + \sum_{j=1}^N \sigma_j \iint_{\partial\Omega_j} \vec{\nabla}_x G(\vec{x}_i, \vec{\xi}) dS_\xi = (1-T)\sigma_i\vec{n} + \sum_{j=1}^N \sigma_j \vec{dG}_{i,j} \quad (2.2)$$

To obtain the influence coefficients $\vec{dG}_{i,j}$, we split up the unit vectors \vec{e}_1 , \vec{e}_2 and \vec{e}_3 into a direction normal to the panel, and a direction tangential to the panel. The integral of the normal derivative of G over a panel is obtained with analytical formulas again, which are listed by Prins [28]. The integral of the tangential derivative of G over a panel is obtained with formulas derived by Fang [13]. When the collocation point and the panel are far away from each other, numerical integration is used again.

Romate [30] showed that the use of a constant-source formulation with a linear panel description leads to a truncation error of order Δ^2 for equation (2.1), and of order Δ for equation (2.2), where Δ is the maximum panel size. This means that, in theory, second derivatives of the potential contain errors of order zero, meaning that these derivatives do not converge when the panel size is reduced. In practice, fortunately, the velocity distribution is usually sufficiently smooth, especially for small panel sizes, to obtain a convergent prediction of the second derivative.

2.2.1 Raised panels

The singularity distribution does not have to be located on the free surface itself; it can also be located at a short distance above the free surface, as long as the collocation points, where the boundary condition has to be satisfied, stay on the free surface. This raised-panel approach has become rather popular lately, especially in non-linear methods. Beck *et al.* [9] used a raised singularity distribution to determine the non-linear unsteady waves near a vertical mounted or truncated cylinder. Beck's arguments for the use of raised singularities were that they make it possible to calculate the influence coefficients with simple numerical quadratures, and that the velocities in the fluid and on the boundaries can be calculated directly from the source distribution. Raven [29] used raised singularities to solve the non-linear steady problem. He also lists a number of advantages of this approach, some of which also apply to our problem. First, the velocity field induced in the fluid is much smoother than with a free-surface singularity method. Second, like Beck also indicates, the integrals of Green functions over panels are desingularized because the collocation points are not located inside the panels, which is easier to evaluate. Third, it is easier to extend our model to a non-linear one. In the non-linear case, the position of the free surface changes in time and, with the raised-panel method, only the position of the collocation points has to be updated in each time step. The position of the singularities is fixed, which is much simpler and more stable. Fourth, numerical damping and dispersion

is reduced when raised panels are used, which will be shown in chapter 3. Jensen [19], like Raven, successfully used a desingularized method to compute the non-linear steady waves around ship hulls. However, he did no theoretical study on the accuracy of his method. His non-linear results were used in a seakeeping program developed by Bertram [5] that uses raised singularities as well. The disadvantage of the use of raised singularities is that it reduces the conditioning of the matrix. Therefore, the distance between the singularities and the free surface must be kept relatively small. In practice, a distance of maximal three times the longitudinal size of a panel is possible.

Because of these considerations, we include the possibility to use raised panels in our model. Of course the panels can also be placed on the free surface as usual. When raised panels are used, the hull of the ship has to be extended to the singularity plane to obtain a closed boundary, as shown in figure 2.3. Therefore, a part of the hull is located above the steady waterline, and a boundary condition must be applied there. Because this is a non-physical domain, we can choose any boundary condition we want, as long as the boundary conditions on the steady free surface and on the mean position of the hull are not violated. We therefore choose the easiest solution, and let the source strength on the hull be zero above the steady waterline.

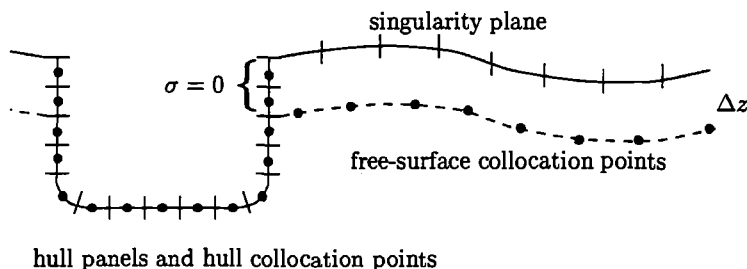


Figure 2.3: Free-surface and hull singularity plane if raised panels are used.

2.3 Discretization of the free-surface condition

The boundary integral has now been discretized, and what remains to be done is to determine the source strengths σ_j . At first sight it might be thought that this can be done by substituting the discretized boundary integrals (2.1) and (2.2) into the free-surface condition (1.12) and the hull condition (1.14), and satisfy them in a set of collocation points. If this can be carried out, only errors arise from the discretization of the boundary integral, and spatial derivatives in (1.12) are calculated free from any other errors. Unfortunately, this approach does not work, because some numerical damping is required to suppress instabilities that occur in the time integration of the free-surface condition. An extensive investigation on stability, numerical damping and numerical dispersion is presented in chapter 3. There, it is shown that our numerical scheme can be made stable

by using upwind difference schemes for the first and second tangential derivatives of the potential in (1.12). Therefore, we first discretize the tangential space derivatives and the time derivatives in (1.12), and then substitute the discretized boundary integrals.

Linear, time-dependent flow problems are mostly solved in the frequency domain. Then, it is assumed that one characteristic frequency describes the time dependence of the flow, so time derivatives can be obtained exactly, and only the spatial behaviour of the flow has to be determined. The disadvantage of this approach is that non-linear effects can never be included. The ultimate research goal is to be able to calculate the non-linear free-surface flow around a freely-sailing commercial ship. Our research may be extended to deal with these non-linearities, so a time-domain approach is followed. Furthermore, by using step-response functions it is possible to simulate general, non-harmonic time signals.

If a time-domain approach is used, the time derivatives that occur in the free-surface condition (1.12) have to be discretized. We use a uniform time step, Δt , and second-order difference schemes for the first, and second derivatives of ϕ

$$\frac{\partial^2 \phi^i}{\partial t^2} = \frac{1}{(\Delta t)^2} (2\phi^i - 5\phi^{i-1} + 4\phi^{i-2} - \phi^{i-3}) + \mathcal{O}((\Delta t)^2) \quad (2.3)$$

$$\frac{\partial \phi^i}{\partial t} = \frac{1}{\Delta t} \left(\frac{3}{2}\phi^i - 2\phi^{i-1} + \frac{1}{2}\phi^{i-2} \right) + \mathcal{O}((\Delta t)^2) \quad (2.4)$$

We see that the potential on the three previous time levels has to be stored to calculate the potential at the current time level, after which we proceed to the next time level.

The discretization of the unsteady potential's space derivatives is more difficult. To see how to proceed, we rewrite the free-surface condition (1.12), where we also use the difference schemes for the time derivatives, (2.3) and (2.4).

$$\begin{aligned} \phi^i \left(\frac{2}{(\Delta t)^2} - \frac{T}{gS} \frac{3}{2\Delta t} \right) + \vec{\nabla} \Phi_s \cdot \vec{\nabla} (\vec{\nabla} \Phi_s \cdot \vec{\nabla} \phi^i) + \left(2 \frac{3}{2\Delta t} - \frac{T}{gS} \right) \vec{\nabla} \phi^i \cdot \vec{\nabla} \Phi_s \\ + g \frac{\partial \phi^i}{\partial z} + \frac{1}{2} \left(\frac{\partial \phi^i}{\partial x} \frac{\partial}{\partial x_\zeta} + \frac{\partial \phi^i}{\partial y} \frac{\partial}{\partial y_\zeta} \right) \|\vec{\nabla} \Phi_s\|^2 = f \quad \text{on } z = \zeta_s \end{aligned} \quad (2.5)$$

where T is the transfer term

$$T = \frac{\partial}{\partial z} \left(\frac{1}{2} \left(\frac{\partial \Phi_s}{\partial x} \frac{\partial}{\partial x_\zeta} + \frac{\partial \Phi_s}{\partial y} \frac{\partial}{\partial y_\zeta} \right) \|\vec{\nabla} \Phi_s\|^2 + g \frac{\partial \Phi_s}{\partial z} \right) \quad \text{on } z = \zeta_s \quad (2.6)$$

and S is an abbreviation for

$$S = 1 + \frac{1}{2g} \frac{\partial}{\partial z} \|\vec{\nabla} \Phi_s\|^2 \quad (2.7)$$

f is a function that depends on the history of the potential

$$f = \frac{5\phi^{i-1} - 4\phi^{i-2} + \phi^{i-3}}{(\Delta t)^2} + \left(2\vec{\nabla}\Phi_s \cdot \vec{\nabla} - \frac{T}{gS} \right) \frac{(2\phi^{i-1} - \frac{1}{2}\phi^{i-2})}{\Delta t}$$

First, we will look in detail at the derivative of ϕ in the direction of the steady velocity, $\vec{\nabla}\Phi_s$. Because the steady velocity is parallel to the steady free surface, this is a tangential derivative. Although the collocation points lie on the curved, steady free surface, $z = \zeta_s$, this derivative can be obtained by numerical differentiation in the flat x, y -plane. To make this clear, we make use of the partial derivative $\frac{\partial}{\partial x_{\zeta_s}}$ and $\frac{\partial}{\partial y_{\zeta_s}}$ (see chapter 1, section 2), and rewrite the derivative into

$$\vec{\nabla}\Phi_s \cdot \vec{\nabla}\phi = \frac{\partial\Phi_s}{\partial x} \frac{\partial\phi}{\partial x} + \frac{\partial\Phi_s}{\partial y} \frac{\partial\phi}{\partial y} + \left(\frac{\partial\zeta_s}{\partial x} \frac{\partial\Phi_s}{\partial x} + \frac{\partial\zeta_s}{\partial y} \frac{\partial\Phi_s}{\partial y} \right) \frac{\partial\phi}{\partial z} = \frac{\partial\Phi_s}{\partial x} \frac{\partial\phi}{\partial x_{\zeta_s}} + \frac{\partial\Phi_s}{\partial y} \frac{\partial\phi}{\partial y_{\zeta_s}}$$

where we used the steady kinematic free-surface condition in the first step. So, if we consider the potential on the free surface to be a function of x and y only, the tangential derivative can be obtained by means of very simple difference schemes for a flat plane. To determine $\vec{\nabla}\Phi_s \cdot \vec{\nabla}\phi$, we use a second-order upwind difference scheme. In this difference scheme, only collocation points are used that are upstream of the collocation point where the derivative is required, and of course that collocation point itself. This ensures a numerically-stable time integration. In chapter 3 we show that central difference schemes mostly lead to instable schemes, whereas upwind schemes never do.

The difficulty in obtaining this derivative is that the collocation points are mostly not in the direction of the steady flow, because our grid only approximately follows the steady stream lines, as shown in figure 2.4. For simplicity, we assume here that the panels are rectangular, and all have the same size. To obtain two values of the potential in the direction of the steady flow, we interpolate the potential from two nearby collocation points with the same x -coordinate, which results in the values of the potential with second-order accuracy on the positions marked with an 'o' in figure 2.4. Higher-order interpolation does not lead to higher-order accuracy, because the accuracy of the potential is only of second order in a first-order panel method. In the difference scheme we now use the potential in the point \vec{x} itself, and in the points where we interpolated the potential, $\vec{x}_1 = \vec{x} - \Delta s \frac{\vec{\nabla}\Phi_s}{\|\vec{\nabla}\Phi_s\|}$ and $\vec{x}_2 = \vec{x} - 2\Delta s \frac{\vec{\nabla}\Phi_s}{\|\vec{\nabla}\Phi_s\|}$, which results in

$$\vec{\nabla}\Phi_s \cdot \vec{\nabla}\phi = \|\vec{\nabla}\Phi_s\| \frac{\frac{3}{2}\phi(\vec{x}) - 2\phi(\vec{x}_1) + \frac{1}{2}\phi(\vec{x}_2)}{\Delta s} + \mathcal{O}((\Delta s)^2) \quad (2.8)$$

This is a second-order scheme if the potentials are free of errors. Unfortunately, the potentials contain errors due to the discretization of the source distribution, the discretization of the boundaries, and the interpolation. This error is of second order in the panel size, which means that the derivative (because of dividing by Δs) contains a first-order error. Because in each interpolation two collocation points are used, the final difference scheme includes maximal 5 of the N_{f_s} free-surface collocation points, so it looks like

$$\vec{\nabla}\Phi_s \cdot \vec{\nabla}\phi(\vec{x}_i) = \sum_{j=1}^{N_{f_s}} \alpha_{ij} \phi(\vec{x}_j) \quad (2.9)$$

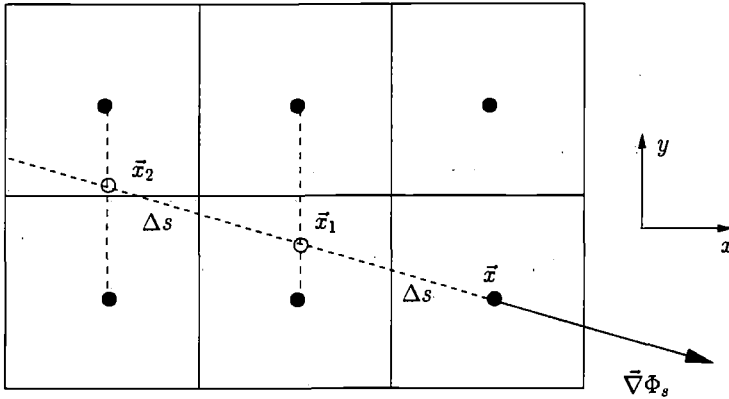


Figure 2.4: Example of the method to determine the difference scheme for $\nabla\bar{\Phi}_s \cdot \nabla\bar{\phi}$.

If i is kept constant, at most 5 of the α_{ij} are non-zero. If panels of non-rectangular shape are used, equation (2.8) slightly changes, but the idea remains the same. Because our computational free surface is limited in size, this method cannot be applied on the last row of panels on its upstream edge. Because there are no upstream panels, it is not possible to use an upwind difference scheme. If $\tau > \frac{1}{4}$, this can easily be solved by imposing the condition $\phi = 0$ on these panels, because waves cannot propagate in the upstream direction. Therefore, apart from incoming waves, no waves exist. If $\tau < \frac{1}{4}$, waves can also propagate in upstream direction. In that case, the condition $\phi = 0$ can also be imposed, as long as a damping zone, that damps the waves sufficiently, is placed between the ship and the upstream edge of the computational domain. In that case, the waves have vanished by the time they have reached the last row of panels, and the condition $\phi = 0$ makes sense. This means that, if $\tau < \frac{1}{4}$, the size of the computational domain in front of the ship may have to be quite large because the appropriate damping zone has to fit. If the speed of the ship is sufficiently small, central or downwind difference schemes can also be used. No special condition has to be imposed on the last row of panels in that case. The meaning of “sufficiently small” will be investigated in chapter 3.

Second, an expression is required that describes the derivative of ϕ in the direction of

$$\vec{l} = \left(\frac{1}{2} \frac{\partial \|\nabla\bar{\Phi}_s\|^2}{\partial x_{\zeta_s}}, \frac{1}{2} \frac{\partial \|\nabla\bar{\Phi}_s\|^2}{\partial y_{\zeta_s}}, g \right)^T$$

To accomplish this, we split up the vector \vec{l} into two parts. One is in the direction of the steady velocity, and the other is perpendicular to that direction, so

$$\vec{l} = \alpha \nabla\bar{\Phi}_s + \vec{r} \quad \text{with} \quad \vec{r} \cdot \nabla\bar{\Phi}_s = 0$$

Upwind difference schemes are used again to deal with the derivative in the direction of $\nabla\bar{\Phi}_s$. We obtain the remaining derivative, in the direction of \vec{r} , by calculating it directly

from the source distribution, so by taking the inner product of equation (2.2) with \vec{r} . Because this derivative has no component in the direction of the steady velocity, no instabilities will appear.

Third, we have to determine the second derivative of ϕ in (2.5). We obtain this derivative by applying the difference scheme for the first derivative twice, so

$$\vec{\nabla}\Phi_s \cdot \vec{\nabla} \left(\vec{\nabla}\Phi_s \cdot \vec{\nabla}\phi \right) (\vec{x}_i) = \sum_{j=1}^{N_{fs}} \alpha_{ij} \vec{\nabla}\Phi_s \cdot \vec{\nabla}\phi (\vec{x}_j) = \sum_{j=1}^{N_{fs}} \alpha_{ij} \sum_{k=1}^{N_{fs}} \alpha_{jk} \phi (\vec{x}_k) = \sum_{k=1}^{N_{fs}} \gamma_{ik} \phi (\vec{x}_k)$$

where $\gamma_{ik} = \sum_{j=1}^{N_{fs}} \alpha_{ij} \alpha_{jk}$

It can be shown that, if i is kept constant, at most 21 of the γ_{ik} are non-zero, but mostly this number is much smaller. When this scheme is applied far away from the ship, where $\Phi_s = Ux$, it reduces to

$$\frac{U^2}{(\Delta x)^2} \left(\frac{9}{4} \phi (\vec{x}_i) - 6\phi (\vec{x}_i - \Delta x) + \frac{11}{2} \phi (\vec{x}_i - 2\Delta x) - 2\phi (\vec{x}_i - 3\Delta x) + \frac{1}{4} \phi (\vec{x}_i - 4\Delta x) \right)$$

Again, problems are encountered on the panels that are close to the upstream edge of the computational free surface. On the last two rows of panels, it is not possible to use an upwind difference scheme for the second derivative. This means that we have to impose the condition $\phi = 0$ on the second row of panels as well.

In equation (2.5), all quantities can now be expressed in terms of the unknown source strengths. The tangential derivatives of the potential are expressed in terms of the potential itself; the potential is related to the source strengths by expression (2.1), and the derivative in the direction of \vec{r} by expression (2.2). The discretized free-surface condition is now applied to all free-surface collocation points. These collocation points are located on the steady free surface in the centre of a panel, or, in case of raised panels, below the centre of a panel. This results in N_{fs} equations for the $N = N_{fs} + N_h$ unknown source strengths, where N_h is the number of panels on the hull. The remaining N_h equations are obtained by applying the hull boundary condition (1.14) to the hull collocation points, that are located in the centre of a panel again. The normal derivative in (1.14) can be related to the source strengths by taking the inner product of equation (2.2) with the normal vector of the appropriate panel. This results in a further N_h equations, which completes the set of equations. Finally, this set of equations is solved with Gaussian elimination.

2.4 Derivatives of the steady velocity

In the linearized free-surface condition and the hull boundary condition, several derivatives of the steady velocity field occur. Because RAPID only calculates the velocity field, we

have to use difference schemes to obtain these derivatives. A problem that occurs is that, in theory, the velocities are obtained with an accuracy of the order of the panel size, because RAPID uses a first-order panel method. This means that, when these velocities are used in a difference scheme, the error is amplified and may be of order zero. Fortunately, the error in the velocity is often not randomly distributed, but is a smooth function of space. This means that we may write for the steady velocity in the x -direction

$$\frac{\partial \Phi_s}{\partial x} = \frac{\partial \tilde{\Phi}_s}{\partial x} - \Delta x f(x)$$

The exact velocity, on the left-hand side of this equation, is expressed in terms of the velocity calculated by RAPID, $\frac{\partial \tilde{\Phi}_s}{\partial x}$, and a certain error of $\mathcal{O}(\Delta x)$. We now differentiate this RAPID velocity in the x -direction with a first-order scheme, which results in

$$\frac{\partial^2 \tilde{\Phi}_s}{\partial x^2}(x) = \frac{\frac{\partial \tilde{\Phi}_s}{\partial x}(x) - \frac{\partial \tilde{\Phi}_s}{\partial x}(x - \Delta x)}{\Delta x} = \frac{\partial^2 \Phi_s}{\partial x^2}(x) - \frac{\Delta x}{2} \frac{\partial^3 \Phi_s}{\partial x^3}(x) + \Delta x \frac{\partial f}{\partial x}(x) + \mathcal{O}((\Delta x)^2)$$

So if the function f is smooth and has a bounded first derivative and if $\frac{\partial^3 \Phi_s}{\partial x^3}$ exists, we may assume that the error in the derivative of the velocity is of the order of the panel size as well. If the first derivative of the error function f is also smooth, it can be shown that the second derivative of the velocity can be calculated with first-order accuracy as well. In general, the error function will be smooth if the velocity field is smooth. This means that it may be difficult to calculate the derivatives of the velocity field near the ship's bow and stern, because smoothness cannot be guaranteed in those regions. For the moment we assume, however, that all derivatives can be calculated, and we therefore concentrate on the construction of appropriate difference schemes.

2.4.1 The derivatives of the squared velocity

In order to calculate

$$\left(\frac{\partial \phi}{\partial x} \frac{\partial}{\partial x_{\zeta_s}} + \frac{\partial \phi}{\partial y} \frac{\partial}{\partial y_{\zeta_s}} \right) \|\vec{\nabla} \Phi_s\|^2 \quad \text{on } z = \zeta_s$$

we need to know the partial derivatives of the squared steady velocity along the steady free surface in the x - and in the y -direction. The derivative in the direction of the steady velocity is known from the non-linear steady free-surface condition (1.5). This means that the derivative in one more direction is required. Because the largest component of the steady-velocity vector is generally in the x -direction, the other direction is taken to be the y -direction. The derivative in this direction is obtained with a difference scheme. Finally, from the derivatives in the y -direction and in the direction of the steady velocity, the derivative in the x -direction can be obtained.

To calculate the first-order wave elevation, we need to know the vertical derivative of the squared velocity that occurs in the function S (2.7). We obtain this vertical derivative by calculating the steady velocity on two extra surfaces below the free surface, at distances Δz and $2\Delta z$, as shown in figure 2.5.

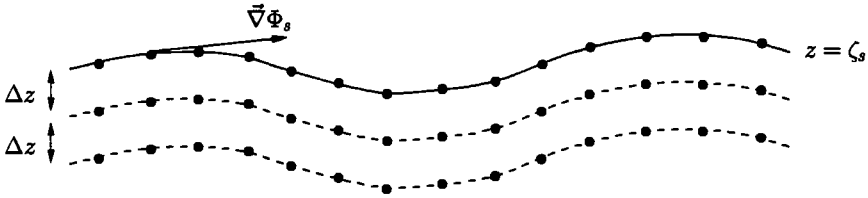


Figure 2.5: Steady free surface and the two levels below it that are used to obtain the vertical derivative.

This can easily be done once the source strengths in RAPID are known, and it only requires the calculation of some extra influence coefficients. The derivative of the squared velocity in the z -direction can now be obtained by means of a second-order difference scheme, similar to the one used for the time derivative (2.4), so

$$\frac{1}{2g} \frac{\partial}{\partial z} \|\vec{\nabla} \Phi_s\|^2 = \frac{\frac{3}{2} \|\vec{\nabla} \Phi_s\|^2(\zeta_s) - 2 \|\vec{\nabla} \Phi_s\|^2(\zeta_s - \Delta z) + \frac{1}{2} \|\vec{\nabla} \Phi_s\|^2(\zeta_s - 2\Delta z)}{2g\Delta z} + \mathcal{O}((\Delta z)^2)$$

The required size of the vertical distance can be estimated by applying the difference scheme to a very simple first-order approximation of the steady velocity

$$\vec{\nabla} \Phi_s = \vec{e}_1 (U - Ae^{kz} \sin kx) + \vec{e}_3 Ae^{kz} \cos kx \quad \text{with } A = \mathcal{O}(U) \quad \text{and } k = \frac{g}{U^2} \quad (2.10)$$

This means that $\|\vec{\nabla} \Phi_s\|^2 = U^2 - 2UAe^{kz} \sin kx + A^2 e^{2kz}$. When this expression is substituted in the difference scheme, it can be derived that the error, ϵ , can be estimated by

$$|\epsilon| \leq \frac{1}{3} (\Delta z)^2 \frac{1}{2g} (2U|A|k^3 + 8A^2k^3)$$

Because $A = \mathcal{O}(U)$, we have to demand that $k^2 (\Delta z)^2 \ll 1$ to have a high accuracy. This means that when the wave number increases (so the wavelength decreases), the vertical distance Δz has to be chosen smaller to obtain the same accuracy.

2.4.2 The transfer term

Because the position of the time-dependent free surface is not known, we linearized the free-surface condition about the steady free surface by using a Taylor expansion. This transfer from the time-dependent free surface to the steady free surface lead to an extra term in the linearized free-surface condition, which we have called the transfer term, see (2.6). The vertical derivative in this transfer term is obtained again with a difference scheme that includes points on the free surface, and on two levels below the free surface, as shown in figure (2.5). This means that at these three levels, we have to determine

$$q(x, y, z) = \frac{1}{2} \left(\frac{\partial \Phi_s}{\partial x} \frac{\partial}{\partial x_{\zeta_s}} + \frac{\partial \Phi_s}{\partial y} \frac{\partial}{\partial y_{\zeta_s}} \right) \|\vec{\nabla} \Phi_s\|^2 + g \frac{\partial \Phi_s}{\partial z} \quad (2.11)$$

On the free surface, this function q should be zero if the exact steady velocities are used. In practice it is non-zero because the velocities $\vec{\nabla}\Phi_s$ satisfy the discretized counterpart of (2.11) that is programmed in RAPID. Therefore, we do not set q zero, but calculate it with the same difference scheme that we will use to determine q on the two surfaces below the free surface. If the errors on all three surfaces are about the same, they will cancel each other out when the vertical derivative is calculated. If q would have been set zero on the steady free surface, the discretization error on the two surfaces below it would have been amplified by $\frac{1}{\Delta z}$. Therefore, we need a difference scheme to obtain the derivative of the squared velocity in (2.11) on all three levels. To accomplish this, we select five collocation points on the free surface that are located close to the point (x_i, y_i, ζ_i) where the transfer term has to be calculated. In this total of six points, the squared velocity is calculated and fitted with a polynomial

$$\|\vec{\nabla}\Phi_s\|^2 = a_1 + a_2(x - x_i) + a_3(y - y_i) + a_4(x - x_i)(y - y_i) + a_5(x - x_i)^2 + a_6(y - y_i)^2 \quad (2.12)$$

The six coefficients are determined such that in the six collocation points, this polynomial takes on the exact values of $\|\vec{\nabla}\Phi_s\|^2$. The derivatives $\frac{\partial}{\partial x_{\zeta_s}}$ and $\frac{\partial}{\partial y_{\zeta_s}}$ can be found by differentiating the polynomial and substituting x_i and y_i , so

$$\frac{\partial}{\partial x_{\zeta_s}} \|\vec{\nabla}\Phi_s\|^2 = a_2 \quad \text{and} \quad \frac{\partial}{\partial y_{\zeta_s}} \|\vec{\nabla}\Phi_s\|^2 = a_3$$

The same can be done on the two surfaces below the free surface. On all these levels the vertical steady velocity is also known, so the function q can be calculated.

A criterion for the vertical distance can be obtained by substituting (2.10) into the function q , which results in

$$q = \frac{1}{2}UA^2ke^{2kz} \sin 2kx$$

If this function is substituted in the difference scheme for the vertical derivative, it can be shown that the error, ϵ , satisfies

$$|\epsilon| \leq \frac{4}{3} (\Delta z)^2 UA^2 k^4$$

This error has dimension ms^{-3} , like the transfer term. To be able to say something about the error, we have to make it dimensionless. If we multiply with $\frac{L}{gU}$ we find

$$|\bar{\epsilon}| = \frac{L}{gU} |\epsilon| \leq \frac{4}{3} (\Delta z)^2 L \frac{A^2}{g} k^4$$

If we assume that $A = \mathcal{O}(U)$, it follows that the restriction $(\Delta z)^2 L k^3 \ll 1$ must be fulfilled in order to get an accurate approximation of the transfer term.

2.4.3 Derivatives of the velocity on the hull

Both the hull boundary condition (1.14) and the formula for the drift forces (1.26) contain derivatives of velocities on the hull. Therefore, we have to develop a method that determines the derivatives of both the steady and the unsteady velocity field on the hull. Only the velocity is known on the hull, so we have to construct a difference scheme to obtain these derivatives. A problem is that three or more hull collocation points generally do not lie in a straight line, so the difference scheme has to take into account the curvature of the hull.

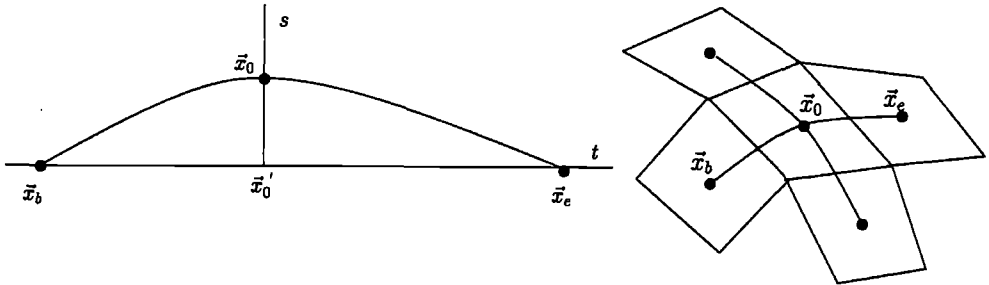


Figure 2.6: Method to determine derivatives of velocities on the hull.

If, at collocation point \vec{x}_0 , the derivatives of the velocities are required, we proceed as follows. Two nearby collocation points \vec{x}_b and \vec{x}_e are selected such that, when we connect the three points with two straight lines, the angle between these lines is as close as possible to 180 degrees (a straight line). These three points are used to define a new, two-dimensional coordinate system (t, s) , as shown in figure 2.6. The relation between these coordinates and the old space coordinates $\vec{x} = (x, y, z)^T$ is

$$\vec{x} = \vec{x}_0' + t \frac{\vec{x}_e - \vec{x}_0'}{\|\vec{x}_e - \vec{x}_0'\|} + s \frac{\vec{x}_0 - \vec{x}_0'}{\|\vec{x}_0 - \vec{x}_0'\|}$$

where \vec{x}_0' is the projection of \vec{x}_0 on the line through \vec{x}_b and \vec{x}_e . It can be found with

$$\vec{x}_0' = \vec{x}_b + \frac{(\vec{x}_0 - \vec{x}_b)^T (\vec{x}_e - \vec{x}_b)}{\|\vec{x}_e - \vec{x}_b\|^2} (\vec{x}_e - \vec{x}_b)$$

In this coordinate system, a parabola $s(t) = a + bt + ct^2$ is fitted through the points \vec{x}_b , \vec{x}_0 and \vec{x}_e . When we differentiate, for example, the velocity in the x -direction, u , with respect to t we obtain

$$\frac{d}{dt}u(t, s(t)) = \frac{\partial u}{\partial t} + \frac{\partial u}{\partial s} \frac{ds}{dt} = \frac{\partial u}{\partial x} \frac{\partial x}{\partial t} + \frac{\partial u}{\partial y} \frac{\partial y}{\partial t} + \frac{\partial u}{\partial z} \frac{\partial z}{\partial t} + \frac{ds}{dt} \left(\frac{\partial u}{\partial x} \frac{\partial x}{\partial s} + \frac{\partial u}{\partial y} \frac{\partial y}{\partial s} + \frac{\partial u}{\partial z} \frac{\partial z}{\partial s} \right) =$$

$$\vec{\nabla} u \cdot \left(\frac{\vec{x}_e - \vec{x}_0'}{\|\vec{x}_e - \vec{x}_0'\|} + \frac{ds}{dt} \frac{\vec{x}_0 - \vec{x}_0'}{\|\vec{x}_0 - \vec{x}_0'\|} \right)$$

With a simple central difference scheme, we can obtain this derivative in the desired point \bar{x}_0 , so in $t = 0$. If we also differentiate the velocities in the y -direction (v) and in the z -direction (w) with respect to t , we obtain three equations for the unknowns $\bar{\nabla}u$, $\bar{\nabla}v$ and $\bar{\nabla}w$. The number of unknowns can be reduced if we use the following relations

$$\frac{\partial v}{\partial x} = \frac{\partial u}{\partial y} \quad \frac{\partial w}{\partial x} = \frac{\partial u}{\partial z} \quad \frac{\partial w}{\partial y} = \frac{\partial v}{\partial z}$$

So only six unknowns remain. Another three equations are found by applying the same procedure to the collocation point and two other points, see figure 2.6. These two points are selected such that the direction in which these points lie is different from the direction belonging to the first two points, and preferably orthogonal or nearly orthogonal to it. Furthermore, the curvature has to be small again. This way we obtain six equations for the six unknowns. We must be careful when we try to solve this system of equations, because it only contains information on tangential derivatives. No information is included on the normal derivative of the normal velocity, for example, which means that the system of equations might become singular. This can be avoided by adding the Laplace equation to the system of equations, which is then solved with a least-squares method.

The main difficulty is to find the surrounding points in such a way that they satisfy the demands of small curvature and near-orthogonality. Sometimes, on parts of the hull with high curvature, it is just not possible to find such points. In that case, we must fall back on simple first-order schemes, or even just set the derivatives to zero to avoid large errors.

2.4.4 Interpolation of steady velocities and derivatives

Because the steady problem and the unsteady problem both have their own characteristics like wavelength, wave amplitude and direction of wave propagation, the grid used in RAPID mostly differs from the grid used in our code. We therefore calculate the derivatives of the steady velocity on the RAPID grid, and interpolate the velocities and the derivatives to our grid. In general, the resolution (number of panels per steady wavelength) will be less in our code than in RAPID. After all, we only have to model the influence of the steady flow on the unsteady waves (which are mostly longer), whereas RAPID actually has to resolve the steady flow. The interpolation can therefore be done very accurately and works as follows: Near each collocation point on our grid, six collocation points on the RAPID grid are selected, and the velocities, their derivatives and the steady wave elevation are approximated by polynomials like (2.12). The values on our grid can then be obtained by substituting the appropriate coordinates into these polynomials.

When we choose the size of our panels, the main criterion is the number of panels per unsteady wavelength. However, we must also make sure that the steady wave is still represented accurately. This may give problems when a long unsteady wave propagates over a relatively small steady wave. Because the number of panels that we can use is limited, high accuracy cannot be guaranteed in this case.

2.5 Incoming waves

We model incoming waves by using an incoming-wave potential that satisfies the Kelvin condition (1.13), the bottom boundary condition and the Laplace equation, so

$$\phi_{inc} = -\frac{g\zeta_a}{\omega_0} \sin(\omega t - kx \cos \theta - ky \sin \theta) \frac{\cosh(k(z+h))}{\cosh(kh)} \quad (2.13)$$

where ζ_a is the wave amplitude, ω_0 the wave frequency in the earth-fixed frame of reference, k the wave number, θ the wave angle and ω the wave frequency in the ship-fixed frame of reference (the encounter frequency). The wave number and the frequencies relate as

$$\omega = \omega_0 + Uk \cos \theta \quad k \tanh(kh) = \frac{\omega_0^2}{g}$$

Far away from the ship, where the steady flow is uniform, the Kelvin condition holds and this wave propagates undisturbed. When it comes close to the ship, it will be disturbed by the presence of the ship and the steady waves around it. The difference between this disturbed wave and the incoming wave is called the diffracted wave. There are two possibilities to incorporate this diffracted wave in our model. First, we can calculate the total wave (incoming plus diffracted wave) by imposing a condition on the edge of the computational domain that will generate incoming waves. Second, we can in advance split up the wave potential in an incoming-wave part (2.13) and a diffracted part and only calculate the latter. If we abbreviate the boundary conditions on the free surface ($i = 1$) and the hull ($i = 2$) into $L_i \phi = 0$, where L_i is a linear operator, and substitute $\phi = \phi_{inc} + \phi_{dif}$, the following relation holds

$$L_i \phi_{dif} = -L_i \phi_{inc}$$

This means that we have to apply the linear operators to the incoming-wave potential (2.13), which now become forcing functions on the right-hand side of the boundary conditions, and we only have to calculate the diffracted potential. In addition to the diffracted and incoming waves, radiated waves exist as well, of course, but these can be calculated independent of the method that we use to simulate the incoming waves. In chapter 4 we will apply the two methods to a test ship, compare them, and decide which is best.

2.6 Symmetry relations

Because the ship is symmetrical about its center plane, $y = 0$, we can make use of symmetry relations to calculate the flow field. This reduces the number of panels by a factor two, since the flow field only has to be calculated on one side of the ship. Because the computational cost for the LU-decomposition is of third order in the number of panels, this decomposition will become eight times faster. The decomposition, however, has to be done for both the symmetrical and the asymmetrical part of the flow field (except for head and following waves, since the asymmetrical part is zero then), so the total computational cost for the decomposition will be reduced a factor four. The computational cost for the

time iteration is of second order in the number of panels. Therefore, when the number of panels is halved, the time iteration will become four times as fast. The total time required for the iterations will be reduced by a factor two, since both the symmetrical part and the asymmetrical part of the flow field have to be calculated. We therefore split up the potential in a symmetrical part, ϕ^s , and an asymmetrical part, ϕ^a , according to

$$\phi = \phi^s + \phi^a \quad \phi^s = \frac{1}{2} (\phi(y) + \phi(-y)) \quad \phi^a = \frac{1}{2} (\phi(y) - \phi(-y))$$

To calculate the added mass and damping, we have to look separately at the symmetrical motions, surge, heave and pitch, and the asymmetrical motions, sway, roll and yaw. The first three result in symmetrical waves and the last three in asymmetrical waves. To calculate the diffracted wave, we have to split the incoming wave into a symmetrical and an asymmetrical part, which are given by

$$\phi_{inc}^s = -\frac{g\zeta_a}{\omega_0} \cos(ky \sin \theta) \sin(\omega t - kx \cos \theta) \frac{\cosh(k(z+h))}{\cosh(kh)}$$

$$\phi_{inc}^a = \frac{g\zeta_a}{\omega_0} \sin(ky \sin \theta) \cos(\omega t - kx \cos \theta) \frac{\cosh(k(z+h))}{\cosh(kh)}$$

If the incoming wave is symmetrical, for head waves for example, the diffracted wave will also be symmetrical, and the corresponding forces and moments on the ship result in surge, heave and pitch motions only. A similar statement holds for the asymmetrical part, that only results in sway, roll and yaw motions. There is no wave angle at which the symmetrical part of the wave is zero, so in any wave condition the surge, heave and pitch motion are involved. By calculating both parts separately, and adding them afterwards, we can find the total diffracted wave and all ship motions.

The symmetry or asymmetry can be imposed upon the potential by making use of mirror panels, like we did to fulfill the bottom boundary condition (see chapter 1, section 7). This time, the panels are mirrored in the plane $y = 0$ instead of in the bottom. If the source strength on these mirror panels is the same as on the original panels, the potential is symmetrical. If it changes sign, the potential is asymmetrical, so

$$\phi(\vec{x}_i) = \sum_{j=1}^N \sigma_j \left(\iint_{\partial\Omega_{j+}} G(\vec{x}_i, \vec{\xi}) dS_{\xi} \pm \iint_{\partial\Omega_{j-}} G(\vec{x}_i, \vec{\xi}) dS_{\xi} \right) \quad (2.14)$$

where $\partial\Omega_{j+}$ is a panel with positive y -coordinate, and $\partial\Omega_{j-}$ the reflection of this panel in the plane $y = 0$. This reduces the number of influence coefficients we have to calculate by a factor two. A similar formula holds for the gradient of the potential. By first reflecting the ship and free surface in the bottom of the water, and then in the plane $y = 0$, four panel surfaces are obtained, as shown in figure 2.7. This means that per panel we have to evaluate four influence coefficients for the potential, and twelve for the gradient. The panels that are reflected in the bottom are in general far away from the

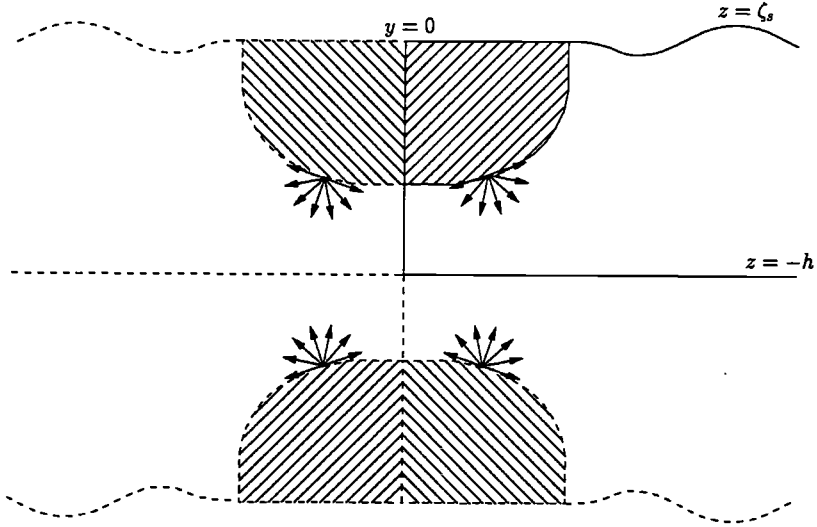


Figure 2.7: Panel surfaces reflected in the bottom and the plane $y = 0$.

collocation points, so the corresponding influence coefficients can be evaluated numerically quite fast. When the forces and moments on the ship have been calculated, we integrate pressure and normal over the starboard side of the ship only, and multiply it by two for symmetrical/symmetrical and asymmetrical/asymmetrical pressure-normal combinations. Symmetrical/asymmetrical combinations yield zero. The expression for the hydrodynamic part of the first-order force, for example, becomes

$$\vec{F}^{(1)} = -\rho \iint_{\bar{H}} \left(\frac{\partial \phi}{\partial t} + \vec{\nabla} \Phi_s \cdot \vec{\nabla} \phi \right) \bar{n} dS = -2\rho \iint_{\bar{H}_+} \begin{pmatrix} \left(\frac{\partial \phi^s}{\partial t} + \vec{\nabla} \Phi_s \cdot \vec{\nabla} \phi^s \right) \bar{n}_1 \\ \left(\frac{\partial \phi^a}{\partial t} + \vec{\nabla} \Phi_s \cdot \vec{\nabla} \phi^a \right) \bar{n}_2 \\ \left(\frac{\partial \phi^s}{\partial t} + \vec{\nabla} \Phi_s \cdot \vec{\nabla} \phi^s \right) \bar{n}_3 \end{pmatrix} dS$$

This formula shows that there is no coupling between symmetrical and asymmetrical modes, so a symmetrical motion will generate no force in the y -direction, or moments around the x - and z -axes, and vice versa. The calculation of the second-order force is more complicated because the second-order force contains products of the potential. The first term in the drift-force formula (1.26), for example, becomes

$$-\frac{1}{2}\rho \iint_{\bar{H}} \vec{\nabla} \phi \cdot \vec{\nabla} \phi \bar{n} dS = -\rho \iint_{\bar{H}_+} \begin{pmatrix} \left(\vec{\nabla} \phi^s \cdot \vec{\nabla} \phi^s + \vec{\nabla} \phi^a \cdot \vec{\nabla} \phi^a \right) \bar{n}_1 \\ 2\vec{\nabla} \phi^s \cdot \vec{\nabla} \phi^a \bar{n}_2 \\ \left(\vec{\nabla} \phi^s \cdot \vec{\nabla} \phi^s + \vec{\nabla} \phi^a \cdot \vec{\nabla} \phi^a \right) \bar{n}_3 \end{pmatrix} dS$$

Because the symmetrical and asymmetrical parts are calculated separately, the first one that is calculated has to be stored. In head or following waves, the asymmetrical part is

zero, so here storing is not necessary.

We may conclude that it is very profitable to use symmetry relations. The total time needed for the LU-decompositions is reduced by a factor four, for the calculation of the influence coefficients by a factor two, and for the time iteration also by a factor two, whereas only some extra storage is required to calculate several drift-force terms.

2.7 Parallelization of the computer code

The numerical model we described is translated in a computer program, written in Fortran. The package PVM (Parallel Virtual Machine) is used to parallelize the code, so that efficient use can be made of the memory of several computers. Furthermore, a decrease in computational time was obtained by spreading the calculation of the influence coefficients over the available computers.

Because we solve the source strengths, in each time step we have to determine the velocity potential and the velocities with four matrix-vector multiplications. The velocity potential is needed to determine the wave height and the pressure on the hull. The velocities are also needed to determine the pressure on the hull. Therefore, we have to store five large matrices in the memory of the computers. First, there is the LU-decomposition of the global matrix, second there is a matrix with influence coefficients with which we can determine the velocity potential from the source strengths, and finally, there are three matrices with influence coefficients with which we can determine the fluid velocity from the source strengths. Each of these matrices is built and stored on a separate computer. The PVM software deals with the interaction between the several processors.

The calculation of the influence coefficients can very easily be spread over the available computers. Therefore, on each of the computers, a part of the influence coefficients is calculated and stored on file. The computer on which a matrix with influence coefficients is built then scans all the computers and reads the influence coefficients from these files. Mostly, the same grid, and therefore the same influence coefficients, are used for several simulations with different lengths of the incoming wave. Therefore, in later simulations, the influence coefficients only have to be read from file. The calculation of the influence coefficients accounts for a large part of the total computational time, so this parallelization speeds up the simulation enormously.

A typical, double precision case with 3500 panels, run on 8 parallel HP 735 workstations is still quite time consuming. Calculating all influence coefficients takes about 3 hours. The LU-decomposition takes about 40 minutes (this is not parallelized) and each of the three time iterations takes 30 minutes if 300 time steps are used (also not parallelized). Of course in case of oblique waves the LU-decomposition and the time iterations have to be repeated for the asymmetrical part of the flow. This shows the limitations of the method.

Chapter 3

Accuracy and stability analysis

In this chapter we investigate the accuracy and stability of the numerical scheme that we described in chapter 2. To accomplish this we consider the simplified case of a wave propagating at a certain angle of incidence over a uniform flow. We compare the dispersion relation in the continuous case with the dispersion relation that holds after discretizing the free surface and the free-surface condition. Differences between the two relations indicate inaccuracies in the numerical scheme. The stability is related to the magnitude of the growth rate. This investigation is an extension of the work of Nakos [24], Raven [29] and Sierevogel [31].

3.1 Introduction

A mathematical model cannot always be solved exactly. Although a unique solution might exist, usually this solution cannot be expressed in terms of elementary functions. Therefore, a numerical model must be used which describes the mathematical model accurately, and which gives an approximation of the real solution. Unfortunately, this approximation is never free of errors, moreover, sometimes the model even becomes unstable, in which case no solution is found at all. Of course it is important to know the magnitude of the error, because without it the approximation is useless, and whether instabilities can appear.

These considerations apply to our model as well. We use a panel method to solve the Laplace equation with linear conditions on the boundaries, and make approximations by dividing the boundaries into panels, by assuming that the source strength is constant on a panel, and by discretizing the free-surface condition. Therefore, the solution we find will differ from the unknown solution of the non-discretized problem and will contain errors.

Because we try to simulate water waves it is best to talk about errors in terms of wrongly predicted wavelengths and wave amplitudes. An error in wavelength is called a dispersion error, and an error in wave amplitude is called a damping error (or amplification error). We will investigate the dependence of these errors on some of the discretization parameters in the numerical model, such as grid size and raised-panel distance. Furthermore, the influence of several difference schemes on these errors will be investigated. We do this by

considering a harmonic wave at a fixed wave frequency that propagates over an infinitely large free surface that has a constant grid size. By deriving a discrete dispersion relation, the length and amplitude of this wave can be found and compared with the exact values which follow from the continuous dispersion relation.

To investigate the stability, we have to look at the waves the other way round. We consider a wave with a certain length, and from the discrete dispersion relation we can find the rate at which the amplitude grows in each time step, and derive a stability criterion.

Similar investigations have been carried out by Nakos [24], Raven [29] and Siervogel [31]. We combine and extend their work so that it is applicable to our numerical scheme. Büchmann [7] also made a stability analysis for his numerical scheme and checked whether his predictions correspond to the actual behaviour of his scheme. It turns out that, due to simplifications in the stability analysis, it gives a necessary but non-sufficient condition for stability.

In order to make a general statement about the accuracy and stability of the numerical scheme, we have to make some simplifications. We approximate the steady flow by a uniform flow, which means that our analysis is only valid far away from the ship where the sea is undisturbed. When we substitute the uniform-flow potential Ux for the steady potential Φ_s in the free-surface condition (1.12), we obtain the well-known Kelvin condition (1.13). Apart from the assumption that the uniform flow can be used, we also assume that the free surface is infinitely large, and that the free-surface panels are rectangular and all have the same size.

As described earlier, we can solve the Laplace equation by placing a source distribution on the boundaries of the domain; the raised-panel surface ($\partial\Omega_1$) and the hull ($\partial\Omega_2$)

$$\phi(\vec{x}, t) = \iint_{\partial\Omega_1} \sigma(\vec{\xi}, t) G(\vec{x}, \vec{\xi}) d\vec{\xi} + \iint_{\partial\Omega_2} \sigma(\vec{\xi}, t) G(\vec{x}, \vec{\xi}) d\vec{\xi}$$

If we substitute this boundary integral for the potential in the Kelvin condition, we obtain

$$\begin{aligned} \iint_{\partial\Omega_1} \left(\frac{\partial^2 \sigma}{\partial t^2} G + 2U \frac{\partial \sigma}{\partial t} \frac{\partial G}{\partial x} + U^2 \sigma \frac{\partial^2 G}{\partial x^2} + g\sigma \frac{\partial G}{\partial z} \right) d\vec{\xi} = \\ - \iint_{\partial\Omega_2} \left(\frac{\partial^2 \sigma}{\partial t^2} G + 2U \frac{\partial \sigma}{\partial t} \frac{\partial G}{\partial x} + U^2 \sigma \frac{\partial^2 G}{\partial x^2} + g\sigma \frac{\partial G}{\partial z} \right) d\vec{\xi} \quad \text{on } z = 0 \end{aligned} \quad (3.1)$$

Because we only consider errors that are caused by discretizing the raised surface and the free-surface boundary condition, we assume that the source strength on the hull is known. We then obtain an integral equation for the source strength on the raised surface only, which can be written as

$$W(x, y, t)\sigma = RHS \quad (3.2)$$

The right-hand side contains, for example, information about the motion of the hull, and can be used to generate waves. When we solve this integral equation, we obtain the source strength and can then find the potential. Because we are interested in the wave-like behaviour of the potential, it is convenient to write the potential as a superposition of elementary waves, which can be achieved with Fourier transforms. First, we will apply the continuous Fourier transform to equation (3.1). The integral equation (3.2) then becomes

$$\widetilde{W}(k, \theta, \omega) \widetilde{\sigma}(k, \theta, \omega) = \widetilde{RHS}(k, \theta, \omega)$$

The zeros of the transformed integral operator \widetilde{W} give the wave-like behaviour of the potential. The equation $\widetilde{W} = 0$ is called the continuous dispersion relation. Second, we will divide the raised surface into panels and discretize the Kelvin condition. We can then apply the discrete Fourier transform to the discretized equations and will find a transformed integral equation

$$\widehat{W}(k, \theta, \omega) \widehat{\sigma}(k, \theta, \omega) = \widehat{RHS}(k, \theta, \omega)$$

In the ideal situation, the discrete dispersion relation $\widehat{W} = 0$ will have exactly the same solutions as the continuous dispersion relation. In practice, unfortunately, differences always occur. By comparing the solutions of the two relations, a statement on the discretization error can be made. From the discrete dispersion relation, a stability criterion can be derived as well.

3.2 The continuous dispersion relation

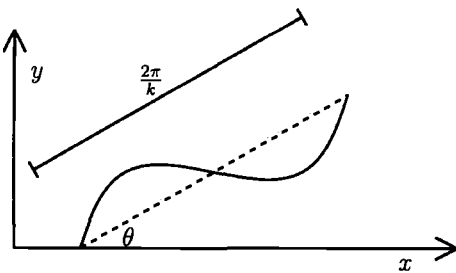


Figure 3.1: Wave with wave number k and angle of incidence θ .

An elementary surface wave with wave number k , frequency ω and angle of incidence θ can be written as follows:

$$\phi(x, y, t) = \Re\{Ae^{i(\omega t - kx \cos \theta - ky \sin \theta)}\}$$

If the cosine of the angle of incidence is positive, this wave propagates in positive x-direction; if it is zero, this wave is a beam wave, and if it is negative this wave propagates in negative x-direction. This is shown in figure 3.1. We can decompose any linear wave into a number of these elementary

waves, according to the following variant of the Fourier transform

$$\phi(x, y, t) = \frac{1}{(2\pi)^3} \int_{-\infty-\pi 0}^{\infty} \int_{-\infty-\pi 0}^{\pi} \int_{-\infty-\pi 0}^{\infty} \widetilde{\phi}(k, \theta, \omega) e^{i(\omega t - kx \cos \theta - ky \sin \theta)} k dk d\theta d\omega \quad (3.3)$$

The “strength” of each elementary wave, $\tilde{\phi}$, can be found from

$$\tilde{\phi}(k, \theta, \omega) = \int_{-\infty}^{\infty} \int_{-\infty}^{\infty} \int_{-\infty}^{\infty} \phi(x, y, t) e^{-i(\omega t - kx \cos \theta - ky \sin \theta)} dx dy dt \quad (3.4)$$

To obtain the Fourier transform of equation (3.1) we use the convolution theorem, which states that the Fourier transform of a convolution is the product of the transforms of the convoluted terms. Because equation (3.1) contains convolutions of the source distribution (or its time derivatives) with the Green function (or its space derivatives) we need their transforms. The transform of the source distribution will be called $\tilde{\sigma}$. The Fourier transform of the Green function G and its vertical derivative $\frac{\partial G}{\partial z}$ are derived in Appendix B and equal

$$\tilde{G} = -\frac{e^{-z_f k}}{2k} \quad \frac{\partial \tilde{G}}{\partial z} = -\frac{e^{-z_f k}}{2} = k \tilde{G} \quad (3.5)$$

z_f is the distance from the free surface, $z = 0$, to the raised surface, $z = z_f$. The Fourier transforms of the other terms in (3.1) follow immediately from differentiating the definition of the inverse transform (3.3). Combining all the terms, we finally find the continuous Fourier transform of equation (3.1)

$$\widetilde{W} \tilde{\sigma} = \tilde{G} (-\omega^2 + 2Uk\omega \cos \theta - U^2 k^2 \cos^2 \theta + gk) \tilde{\sigma} = \widetilde{RHS} \quad (3.6)$$

This expression gives us the Fourier transform of the source strength. The Fourier transform of the potential follows from $\tilde{\phi} = \tilde{\sigma} \tilde{G}$ and can be used to find the potential itself from the inverse transform (3.3) in terms of a superposition of elementary waves

$$\phi(x, y, t) = \frac{1}{(2\pi)^3} \int_{-\infty}^{\infty} \int_{-\pi}^{\pi} \int_0^{\infty} \frac{\widetilde{RHS} \tilde{G}}{\widetilde{W}} e^{i(\omega t - kx \cos \theta - ky \sin \theta)} k dk d\theta d\omega \quad (3.7)$$

From complex-integration theorems it follows that the zeros of the integrand in this expression give the wave-like contributions of the potential. We therefore have to solve the continuous dispersion relation

$$-\omega^2 + 2Uk\omega \cos \theta - U^2 k^2 \cos^2 \theta + gk = 0,$$

which relates the wave number, wave angle, wave frequency and speed of the uniform flow. If three of these quantities are known, the fourth can be determined. Here, we will assume that all quantities are known except the wave number, which follows from solving the dispersion relation. It can be shown that the behaviour of the solution depends on the value of $\tau = \frac{\omega U}{g}$. If $\tau \leq \frac{1}{4}$, the dispersion relation has two real roots for all values of θ . Physically, this means that waves can propagate in all directions because the speed of

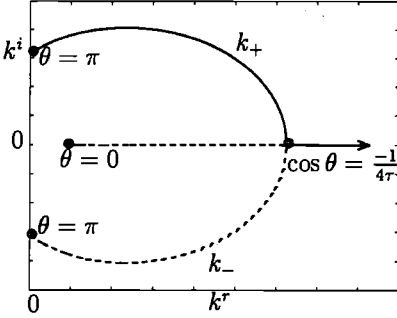


Figure 3.2: Wave numbers $k_{\pm} = k_{\pm}^r + ik_{\pm}^i$ in the complex plane for $\tau = \frac{1}{2}$, $Fn = 0.4$.

propagation of the upstream waves is greater than the speed of the ship. If $\tau > \frac{1}{4}$, and $1 + 4\tau \cos \theta \geq 0$, the dispersion relation has two real roots, else it has two complex-conjugate roots with non-zero imaginary parts. In the latter case the waves are evanescent, which means that they are exponentially decreasing in amplitude along the direction of propagation, which can only happen if the wave propagates in upstream direction. The integration contours in (3.7) can always be chosen such that the radiation condition is fulfilled, see for example Wehausen and Laitone [37].

The two solutions of the dispersion relation are

$$k_{\pm} = \begin{cases} \frac{g}{4U^2 \cos^2 \theta} (1 \pm \sqrt{1 + 4\tau \cos \theta})^2 & \text{if } 1 + 4\tau \cos \theta \geq 0, \\ \frac{g}{4U^2 \cos^2 \theta} (1 \pm i\sqrt{-1 - 4\tau \cos \theta})^2 & \text{if } 1 + 4\tau \cos \theta < 0. \end{cases} \quad (3.8)$$

In the next section we will derive the dispersion relation that holds after discretization of the Kelvin condition, the raised surface and the source distribution. The solutions of this discrete dispersion relation will be compared with the solutions of the continuous dispersion relation.

3.3 The discrete dispersion relation

The dispersion relation will change if the propagating wave no longer satisfies the continuous equations, but now satisfies the discretized ones. We will investigate the influence of the discretization of the raised surface, the source distribution and the Kelvin condition on the dispersion relation. We assume that the unbounded raised surface, located at a distance z_{fs} above the free surface, is divided into an infinite number of rectangular panels with size $\Delta x \times \Delta y$, as shown in figure 3.3. The vertical distance z_{fs} is related to the panel size by $z_{fs} = \mu\sqrt{\Delta x \Delta y}$. On each panel the source strength is assumed to be constant. The collocation points with coordinates (x_m, y_n) are located below the middle of a panel on the free surface $z = 0$. With these assumptions, the boundary integral for the potential in a collocation point (x_m, y_n) becomes

$$\begin{aligned} \phi(x_m, y_n, 0, t) &= \sum_{i=-\infty}^{\infty} \sum_{j=-\infty}^{\infty} \sigma_{i,j}(t) \int_{(i-\frac{1}{2})\Delta x}^{(i+\frac{1}{2})\Delta x} \int_{(j-\frac{1}{2})\Delta y}^{(j+\frac{1}{2})\Delta y} \frac{-dx_0 dy_0}{4\pi \sqrt{(x_m - x_0)^2 + (y_n - y_0)^2 + z_{fs}^2}} = \\ &= \sum_{i=-\infty}^{\infty} \sum_{j=-\infty}^{\infty} \sigma_{i,j} G_{m-i, n-j} \end{aligned} \quad (3.9)$$

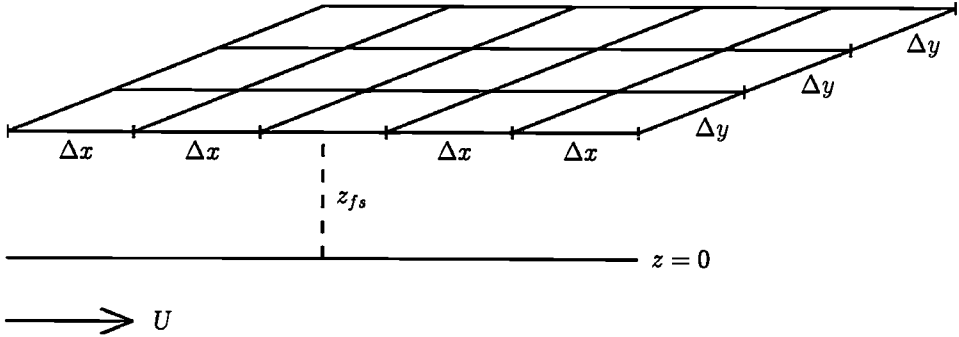


Figure 3.3: Uniformly-spaced grid on the raised-panel surface

What remains to be discretized are the derivatives of the potential in the Kelvin condition. For the space derivatives that are tangential to the free surface, either upwind or central difference schemes can be used. Central difference schemes have the advantage that they are very accurate, whereas upwind difference schemes have the advantage that they usually lead to stable numerical schemes. In general, the derivatives can be written as follows

$$\frac{\partial \phi}{\partial x}(x_m) = \frac{1}{\Delta x} \sum_{j=-\infty}^{\infty} d_j^{(x)} \phi(x_{m-j}) \quad \frac{\partial^2 \phi}{\partial x^2}(x_m) = \frac{1}{(\Delta x)^2} \sum_{j=-\infty}^{\infty} d_j^{(xx)} \phi(x_{m-j}) \quad (3.10)$$

where, generally, almost all coefficients are zero. The time derivatives are obtained with difference schemes that can be written as

$$\frac{\partial \phi}{\partial t}(t_n) = \frac{1}{\Delta t} \sum_{j=-\infty}^{\infty} d_j^{(t)} \phi(t_{n-j}) \quad \frac{\partial^2 \phi}{\partial t^2}(t_n) = \frac{1}{(\Delta t)^2} \sum_{j=-\infty}^{\infty} d_j^{(tt)} \phi(t_{n-j}) \quad (3.11)$$

where, again, almost all coefficients are zero. Looking at the Kelvin condition, we see that the only term we have not discussed is $\frac{\partial \phi}{\partial z}$. We obtain this term from the boundary integral for ϕ by taking the vertical derivative

$$\begin{aligned} \frac{\partial \phi}{\partial z}(x_m, y_n, 0, t) &= \sum_{i=-\infty}^{\infty} \sum_{j=-\infty}^{\infty} \sigma_{i,j}(t) \int_{(i-\frac{1}{2})\Delta x}^{(i+\frac{1}{2})\Delta x} \int_{(j-\frac{1}{2})\Delta y}^{(j+\frac{1}{2})\Delta y} \frac{-z_{fs} dx_0 dy_0}{4\pi ((x_m - x_0)^2 + (y_n - y_0)^2 + z_{fs}^2)^{\frac{3}{2}}} = \\ &= \sum_{i=-\infty}^{\infty} \sum_{j=-\infty}^{\infty} \sigma_{i,j} Q_{m-i, n-j} \end{aligned} \quad (3.12)$$

Now that we have discretized the Kelvin condition, the source distribution and the raised surface, the discrete dispersion relation can be derived. This is done by introducing a discrete Fourier transform and its inverse, defined by the following pair of equations

$$\widehat{\phi}(k, \theta, \omega) = \Delta x \Delta y \Delta t \sum_{m=-\infty}^{\infty} \sum_{n=-\infty}^{\infty} \sum_{p=-\infty}^{\infty} \phi(x_m, y_n, t_p) e^{-i(\omega p \Delta t - km \Delta x \cos \theta - kn \Delta y \sin \theta)} \quad (3.13)$$

$$\phi(x_m, y_n, t_p) = \frac{1}{(2\pi)^3} \int_{-\frac{\pi}{\Delta t}}^{\frac{\pi}{\Delta t}} \int_{-\frac{\pi}{\Delta y}}^{\frac{\pi}{\Delta y}} \int_{-\frac{\pi}{\Delta x}}^{\frac{\pi}{\Delta x}} \hat{\phi}(k, \theta, \omega) e^{i(\omega p \Delta t - k m \Delta x \cos \theta - k n \Delta y \sin \theta)} d(k \cos \theta) d(k \sin \theta) d\omega \quad (3.14)$$

Note that in the limit case, $\Delta x, \Delta y, \Delta t \rightarrow 0$, the discrete transform becomes the continuous transform. The discrete Fourier transform of equations (3.9) and (3.12) can be obtained by relating it to the continuous transforms \tilde{G} and $\frac{\partial \tilde{G}}{\partial z}$ (3.5) with the aliasing theorem. This theorem relates the discrete Fourier transform of discrete values of a function to the continuous Fourier transform of the function itself. If we also use the discrete convolution theorem, the discrete dispersion relation can be derived, which is done in Appendix B. We only mention the final result for the discrete dispersion relation, which is

$$\widehat{W} = \frac{1}{(\Delta t)^2} \sum_{j=-\infty}^{\infty} d_j^{(tt)} e^{-i\omega_j \Delta t} + \frac{2U}{\Delta x \Delta t} \sum_{j=-\infty}^{\infty} d_j^{(x)} e^{ik_j \Delta x \cos \theta} \sum_{j=-\infty}^{\infty} d_j^{(t)} e^{-i\omega_j \Delta t} + \frac{U^2}{(\Delta x)^2} \sum_{j=-\infty}^{\infty} d_j^{(xx)} e^{ik_j \Delta x \cos \theta} + g \frac{\widehat{Q}}{\widehat{G}} = 0$$

where \widehat{G} and \widehat{Q} are the discrete Fourier transforms of $G_{i,j}$ (3.9), and $Q_{i,j}$ (3.12). They are listed in appendix B, equations (B.16) and (B.17).

Unlike the continuous dispersion relation, this discrete dispersion relation cannot be solved exactly. A numerical procedure as, for example, the method of Newton has to be used to find the roots of the discrete dispersion relation in the complex plane. Usually, these roots differ from the roots of the continuous dispersion relation (3.8), which indicates an error due to the discretizations. In the next section we will investigate the dependence of this error on a number of discretization factors.

3.4 Damping and dispersion

There are a number of ways to look at the discrete dispersion relation. In this section we assume that the flow has reached a steady-state time-harmonic limit, so the wave frequency is assumed to be known, as well as the propagation angle θ . From the discrete dispersion relation, a discrete wave number k_d can be found with numerical techniques. We compare it with the corresponding solution of the continuous dispersion relation, k_c , by relating them as follows

$$k_d = k_c (1 + C_r + iC_i)$$

k_c is assumed to be real, so we consider non-evanescent waves. If the terms C_r and C_i are both zero, the two roots are equal and there is no discretization error. If C_r is positive, the predicted wave number is too large, which means that the wavelength is too small. If C_r is negative the predicted wavelength is too large. In both cases we speak of

numerical dispersion. A negative C_i corresponds to numerical damping and a positive C_i corresponds to numerical amplification, as can be derived from (3.14).

Source-discretization effects

First, we will study only source-discretization effects, so we assume that the time and space derivatives of ϕ in the Kelvin condition are obtained exactly, without any error, which leaves us with the following discrete dispersion relation

$$-\omega^2 + 2Uk\omega \cos \theta - U^2 k^2 \cos^2 \theta + g \frac{\hat{G}}{Q} = 0.$$

In our analysis we will only consider the root with the '-' sign and omit the root with the '+' sign (see equation (3.8)) because the latter usually corresponds to a short wave which cannot be represented accurately on the free-surface grids that we use and will damp very fast. The only discretizations left are the panel size and the distance from the raised-panel surface to the free surface, z_{fs} . It turns out that if the collocation points are chosen below the centre of a panel like we chose them, the numerical damping is zero. Numerical damping is very useful to suppress instabilities, so we will introduce damping by choosing appropriate difference schemes. Damping can also be introduced by shifting the collocation points upstream like Raven [29] did, but that is not done here. Because the damping is zero, we will only study the effect of the source discretization on the dispersion.

Figure 3.4 shows what happens to the dispersion of several downstream waves when we increase the distance $z_{fs} = \mu\sqrt{\Delta x \Delta y}$ from the free surface to the raised-panel surface for several values of τ and a fixed Froude number $Fn = 0.4$. The reference length L in this Froude number is taken to be one in all the calculations in this chapter. We introduce the non-dimensional longitudinal and transverse wave numbers $\hat{\alpha}$ and $\hat{\beta}$

$$\hat{\alpha} = \frac{k\Delta x \cos \theta}{2\pi} \quad \hat{\beta} = \frac{k\Delta y \sin \theta}{2\pi}$$

$\hat{\alpha} = 0.05$ means we use 20 panels per longitudinal wavelength. κ is the ratio of transverse panel size Δy and longitudinal panel size Δx . It seems that, when μ increases, the dispersion becomes less in all cases and eventually approaches zero. This was also observed by Raven [29] for the steady case. Figure 3.6 shows the same, but now for several upstream waves with wave angle $\theta = \pi$ and a lower Froude number of 0.2. The Froude number was lowered because otherwise only low-frequency upstream waves with a very long wavelength exist, which is not very realistic. It can be seen that the dispersion becomes less if μ increases, like in the downstream case. We may conclude that it is sufficient to use $\mu = 1$ in our calculations, because for all τ and wave angles shown, the dispersion is very small compared to the $\mu = 0$ case.

Figure 3.5 shows what happens to the dispersion of a wave with length $\lambda = 1$ at various downstream angles if we increase the ratio $\kappa = \frac{\Delta y}{\Delta x}$ and keep Δx constant. We see that for waves with zero wave angle, so for waves propagating along the x-axis, it does not matter how large the transverse panel size Δy is. When we increase the wave angle to

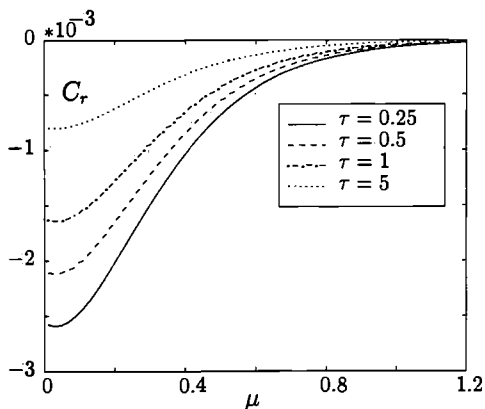


Figure 3.4: Dispersion for increasing μ and several τ . $Fn = 0.4, \theta = 0, \kappa = 1, \hat{\alpha} = 0.05$.

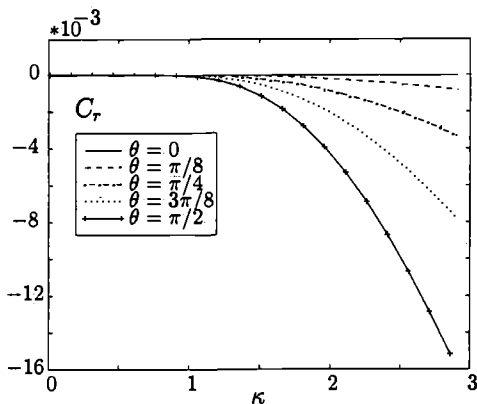


Figure 3.5: Dispersion for increasing κ and several θ . $Fn = 0.4, \hat{\alpha} = 0.05, \mu = 1, \lambda = 1$.

$\frac{\pi}{2}$ with steps of $\frac{\pi}{8}$, the dispersion depends more and more on the transverse panel size, which could be expected since $\theta = \frac{\pi}{2}$ corresponds to a transverse wave. Figure 3.7 shows the same, but now for a number of upstream waves with wave angles ranging from $\frac{\pi}{2}$ to π in steps of $\frac{\pi}{8}$, with length $\lambda = 3$ and at a Froude number of 0.2. Again we see that a small transverse panel size is only important for (nearly) transverse waves. It seems that $\kappa = 1$ is a good choice; little dispersion in all cases and yet it is not too small, so the number of transverse panels will not be too large.

Effect of the difference schemes

The choice of a difference scheme is very important to obtain an accurate prediction of the wave pattern near a sailing ship. Some choices lead to instable solutions and some lead to a lot of damping and dispersion. Unfortunately, a stable difference scheme without any damping or dispersion does not exist. What we can do is investigate a few different schemes and select the one which is stable and minimizes damping and dispersion.

First of all we need difference schemes for the time derivatives in (1.13). When, at a certain time level, the first or second derivative of the potential must be determined, only the potential at the current or previous time levels can be used in the difference scheme, because the future potential is not yet known. Therefore, we must use a backward difference scheme. The more time levels are used in this scheme, the more accurate the scheme is. A drawback, however, is that the use of more time levels requires more memory because the history of the potential has to be stored. We will investigate first-order, second-order and third-order difference schemes for the time derivatives according to the following formulas

$$\frac{\partial \phi}{\partial t}(t_n) = \frac{1}{\Delta t} \left(d_0^{(t)} \phi(t_n) + d_1^{(t)} \phi(t_{n-1}) + d_2^{(t)} \phi(t_{n-2}) + d_3^{(t)} \phi(t_{n-3}) \right),$$

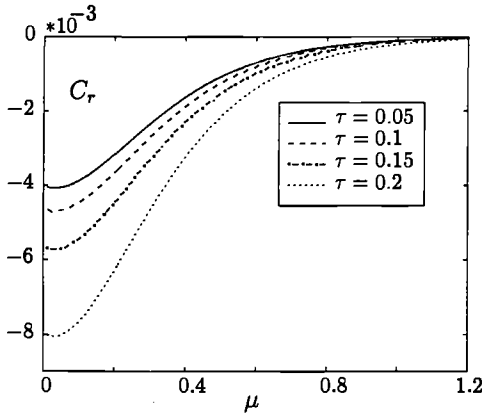


Figure 3.6: Dispersion for increasing μ and several τ . $F_n = 0.2, \theta = \pi, \kappa = 1, \hat{\alpha} = 0.05$.

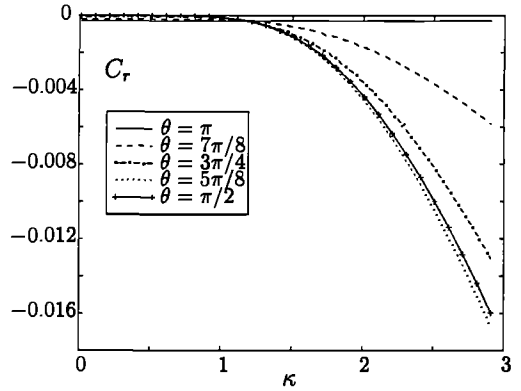


Figure 3.7: Dispersion for increasing κ and several θ . $F_n = 0.2, \hat{\alpha} = 0.05, \mu = 1, \lambda = 3$.

where the coefficients $d_0^{(t)}, d_1^{(t)}, d_2^{(t)}$ and $d_3^{(t)}$ are

	$d_0^{(t)}$	$d_1^{(t)}$	$d_2^{(t)}$	$d_3^{(t)}$
First-order scheme	1	-1	0	0
Second-order scheme	$\frac{3}{2}$	-2	$\frac{1}{2}$	0
Third-order scheme	$\frac{11}{6}$	-3	$\frac{3}{2}$	$-\frac{1}{3}$

$$\frac{\partial^2 \phi}{\partial t^2}(t_n) = \frac{1}{\Delta t^2} \left(d_0^{(tt)} \phi(t_n) + d_1^{(tt)} \phi(t_{n-1}) + d_2^{(tt)} \phi(t_{n-2}) + d_3^{(tt)} \phi(t_{n-3}) + d_4^{(tt)} \phi(t_{n-4}) \right),$$

where the coefficients $d_0^{(tt)}, d_1^{(tt)}, d_2^{(tt)}, d_3^{(tt)}$ and $d_4^{(tt)}$ are

	$d_0^{(tt)}$	$d_1^{(tt)}$	$d_2^{(tt)}$	$d_3^{(tt)}$	$d_4^{(tt)}$
First-order scheme	1	-2	1	0	0
Second-order scheme	2	-5	4	-1	0
Third-order scheme	$\frac{35}{12}$	$-\frac{26}{3}$	$\frac{19}{2}$	$-\frac{56}{12}$	$\frac{11}{12}$

In all three cases, we investigate the dependence of damping and dispersion on the dimensionless parameter

$$\hat{\omega} = \frac{\omega \Delta t}{2\pi}$$

which corresponds to one, divided by the number of time steps per period.

Figure 3.8 shows the dispersion C_r for a downstream wave at wave angle $\theta = 0$ which, as expected, increases in absolute value if the time step increases. With the first-order scheme, the predicted wavelength is too long; with the second-order scheme the predicted wavelength is too short. The third-order scheme much reduces dispersion compared with

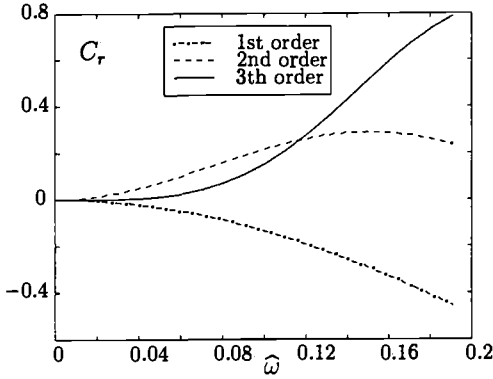


Figure 3.8: Dispersion for increasing $\hat{\omega}$ and several difference schemes. $\tau = 0.5$, $Fn = 0.4$, $\mu = 1$, $\kappa = 1$, $\theta = 0$, $\hat{\alpha} = 0.05$.

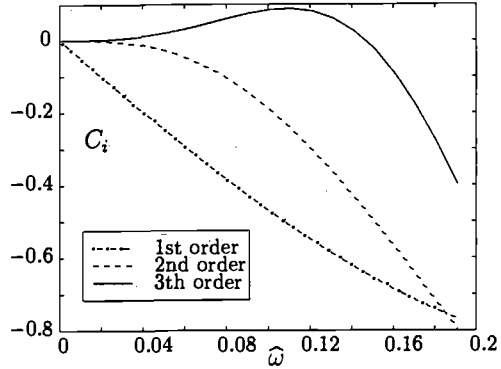


Figure 3.9: Damping for increasing $\hat{\omega}$ and several difference schemes. $\tau = 0.5$, $Fn = 0.4$, $\mu = 1$, $\kappa = 1$, $\theta = 0$, $\hat{\alpha} = 0.05$.

the other two schemes, so speaking strictly from a dispersive point of view the third-order scheme is best. Figure 3.9 shows the damping term C_i , which is negative if a first-order or second-order scheme is used. If a third-order scheme is used, this term becomes slightly positive, which means there is some numerical amplification instead of damping. This can lead to instabilities, so a first-order or second-order scheme is preferred. Since the second-order scheme has the least damping, it is the best choice.

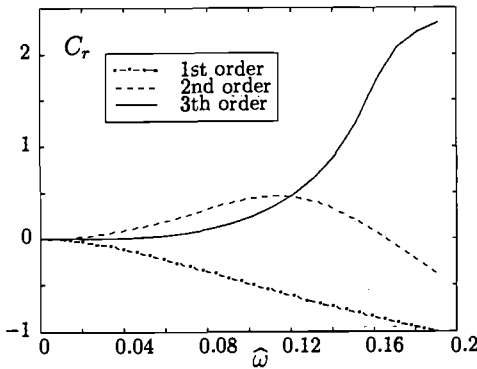


Figure 3.10: Dispersion for increasing $\hat{\omega}$ and several difference schemes. $\tau = 0.2$, $Fn = 0.2$, $\mu = 1$, $\kappa = 1$, $\theta = \pi$, $\hat{\alpha} = 0.05$.

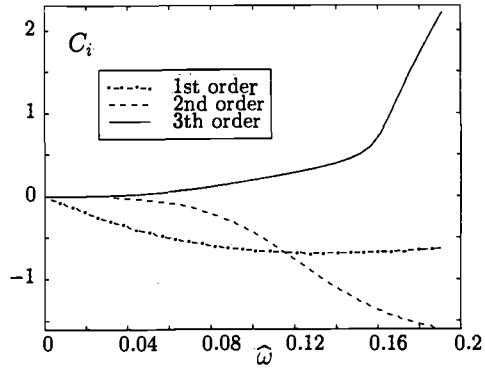


Figure 3.11: Damping for increasing $\hat{\omega}$ and several difference schemes. $\tau = 0.2$, $Fn = 0.2$, $\mu = 1$, $\kappa = 1$, $\theta = \pi$, $\hat{\alpha} = 0.05$.

Figures 3.10 and 3.11 show damping and dispersion for an upstream wave with angle $\theta = \pi$. Again it can be seen that the third-order scheme has the least dispersion for small time steps, but also has some numerical amplification. It is also noticeable that the

third-order scheme leads to more damping and dispersion than the other schemes if a large time step is used. This can be explained by the fact that the five points in the third-order difference scheme are then distributed over a large part of the period of the potential. If less points are used, a quite accurate derivative can still be obtained, even for a large time step. From these examples we may conclude that it is best to use the second-order scheme.

We also need difference schemes for the tangential space derivatives of the potential in (1.13). We will again investigate the dependence of damping and dispersion on some difference schemes. These can be divided in two classes: upwind difference schemes and central difference schemes. In an upwind difference scheme, only points are used that are on the upwind (in aerodynamics) or in our case upstream side of the point where the derivative is required. In a central difference scheme, points are used that are on both sides of the point where the derivative is required. Although, generally, central difference schemes are more accurate than upwind difference schemes, they have the disadvantage that they often lead to instabilities. Upwind difference schemes, however, are well known for their stabilizing properties. Physically this can be explained by the fact that new information on the wave pattern mainly comes from the upstream side, especially at high speeds, whereas the downstream side only contains old information. The difference scheme for the first derivative of ϕ to x can be written as follows

$$\frac{\partial \phi}{\partial x}(x_i) = \frac{1}{\Delta x} \left(d_3^{(x)} \phi(x_{i-3}) + d_2^{(x)} \phi(x_{i-2}) + d_1^{(x)} \phi(x_{i-1}) + d_0^{(x)} \phi(x_i) + d_{-1}^{(x)} \phi(x_{i+1}) \right),$$

where the coefficients are given in the following table.

	$d_3^{(x)}$	$d_2^{(x)}$	$d_1^{(x)}$	$d_0^{(x)}$	$d_{-1}^{(x)}$
First-order upwind scheme	0	0	-1	1	0
Second-order upwind scheme	0	$\frac{1}{2}$	-2	$\frac{3}{2}$	0
Third-order upwind scheme	$-\frac{1}{3}$	$\frac{3}{2}$	-3	$\frac{11}{6}$	0
Second-order central scheme	0	0	$-\frac{1}{2}$	0	$\frac{1}{2}$

Table 3.1: Coefficients for first derivatives.

A similar formula holds for the second derivative of ϕ to x

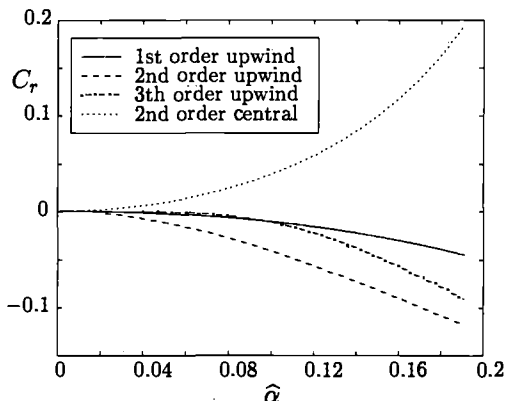
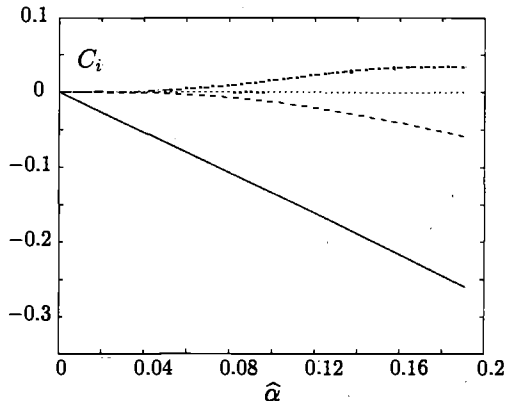
$$\frac{\partial^2 \phi}{\partial x^2}(x_i) = \frac{1}{\Delta x^2} \left(d_4^{(xx)} \phi(x_{i-4}) + d_3^{(xx)} \phi(x_{i-3}) + d_2^{(xx)} \phi(x_{i-2}) + d_1^{(xx)} \phi(x_{i-1}) + d_0^{(xx)} \phi(x_i) + d_{-1}^{(xx)} \phi(x_{i+1}) \right)$$

These coefficients are given in table 3.2.

First, we will investigate the influence of these four difference schemes on the damping and dispersion of some downstream waves when we vary the number of panels per wavelength. Calculations were done for the cases $\tau = 0.5$ and $\tau = 1.5$. In all calculations we used the Froude number $Fn = 0.4$, the angle of incidence $\theta = 0$, the relative height of the panel surface $\mu = 1$, the relative width of a panel $\kappa = 1$ and $\hat{\omega} = 0.005$, so 200 time steps per

	$d_4^{(xx)}$	$d_3^{(xx)}$	$d_2^{(xx)}$	$d_1^{(xx)}$	$d_0^{(xx)}$	$d_{-1}^{(xx)}$
First-order upwind scheme	0	0	1	-2	1	0
Second-order upwind scheme	$\frac{1}{4}$	-2	$\frac{11}{2}$	-6	$\frac{9}{4}$	0
Third-order upwind scheme	$\frac{35}{12}$	$-\frac{26}{3}$	$\frac{19}{2}$	$-\frac{56}{12}$	$\frac{11}{12}$	0
Second-order central scheme	0	0	0	1	-2	1

Table 3.2: Coefficients for second derivatives.

Figure 3.12: Dispersion for several difference schemes, increasing $\hat{\alpha}$ and $\tau = 0.5$.Figure 3.13: Damping for several difference schemes, increasing $\hat{\alpha}$, and $\tau = 0.5$. Legend as in figure 3.12.

period. A large number of time steps per period was used to make sure that the error is mainly caused by the use of the spatial difference scheme.

Figure 3.12 shows the dispersion for $\tau = 0.5$ and increasing $\hat{\alpha}$ (so the number of panels per wavelength decreases) for the four difference schemes. If upwind difference schemes are used, the dispersion term C_r is negative, so the predicted wavelength is too long. If the central difference scheme is used, the predicted wavelength is too short. It is interesting to see that, for small $\hat{\alpha}$, the first-order upwind scheme has less dispersion than the second-order scheme and about the same as the third-order scheme. It is also remarkable that the use of the central difference scheme leads to more dispersion than the use of the upwind schemes. Figure 3.13 shows the damping for $\tau = 0.5$ and increasing $\hat{\alpha}$. Unlike the dispersion, the damping is largest if the first-order upwind scheme is used. The second-order upwind scheme also has some damping, but much less and the third-order scheme even has some numerical amplification. The damping is nearly zero if the central scheme is used. From these two figures we might conclude that it is best to use a central difference scheme.

The next two figures, however, show that this statement is false. Figures 3.14 and 3.15 show the damping and dispersion again, but now for $\tau = 1.5$, corresponding to a higher frequency and a smaller wavelength. We see that the upwind difference schemes produce results similar to the $\tau = 0.5$ case. If central difference schemes are used, a problem

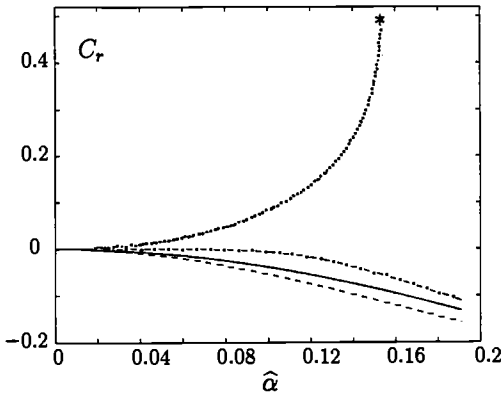


Figure 3.14: Dispersion for several difference schemes, increasing $\hat{\alpha}$ and $\tau = 1.5$. Legend as in figure 3.12.

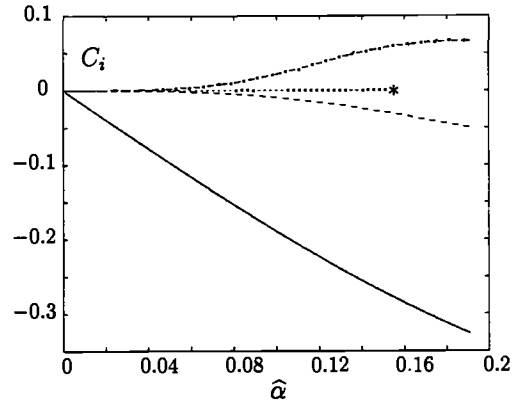


Figure 3.15: Damping for several difference schemes, increasing $\hat{\alpha}$ and $\tau = 1.5$. Legend as in figure 3.12.

occurs at $\hat{\alpha} = 0.155$ and higher, because the discrete dispersion relation has no longer a root near the solution of the continuous dispersion relation, but only a so-called spurious root, which has a large real part (short wave) and a positive imaginary part. These short waves will amplify rapidly and cause numerical instabilities. It is quite difficult to find the point at which this happens, so we will study numerical stability in a different way in the next section.

This investigation indicates that it is tempting to use central difference schemes because of their high accuracy, but that using these schemes is also dangerous because, when the speed of the flow and the frequency of the wave is increased, a point is reached where the numerical scheme becomes unstable.

3.5 Temporal stability

In the previous section we made the assumption that the flow has reached a steady-state time-harmonic limit, from which the corresponding wave number could be found. In this section we will investigate what happens, as time goes by, to a wave at a certain angle θ and with a certain length λ . Thus something can be said about the stability of the numerical scheme, because a wave amplitude that remains bounded in time indicates a stable scheme, whereas an unbounded wave amplitude indicates an unstable scheme. From the definition of the inverse discrete Fourier transform (3.14) it can be seen that when we go from one time level to the next, each frequency component of the potential is multiplied by the growth rate $Z = e^{i\omega\Delta t}$. An obvious criterion for stability is that the modulus of this growth rate should be less or equal to one. If it exceeds one, the potential will become unbounded, indicating an unstable numerical scheme. This stability will be referred to as temporal stability according to the definitions of Kim, Kring and Sclavounos [20].

If second-order difference schemes are used to approximate the time derivatives of the potential, the discrete dispersion relation can be written as a third-order polynomial in Z

$$\widehat{W} = \left(\frac{2}{(\Delta t)^2} + \frac{3}{2} \frac{2U}{\Delta x \Delta t} D^{(x)} + \frac{U^2}{(\Delta x)^2} D^{(xx)} + g \frac{\widehat{Q}}{G} \right) Z^3 + \left(-\frac{5}{(\Delta t)^2} - 2 \frac{2U}{\Delta x \Delta t} D^{(x)} \right) Z^2 + \left(\frac{4}{(\Delta t)^2} + \frac{1}{2} \frac{2U}{\Delta x \Delta t} D^{(x)} \right) Z - \frac{1}{(\Delta t)^2} = 0 \quad (3.15)$$

where $D^{(x)} = \sum_{j=-\infty}^{\infty} d_j^{(x)} e^{ikj\Delta x \cos \theta}$ and $D^{(xx)} = \sum_{j=-\infty}^{\infty} d_j^{(xx)} e^{ikj\Delta x \cos \theta}$, so a choice for a spatial difference scheme has not yet been made. A third-order polynomial has three roots in the complex plane. The numerical scheme is temporally stable if all these roots are inside the unit circle in the complex plane. If one or more of the three roots is outside the unit circle, the potential will exponentially increase in time and become unbounded.

First, we will investigate the temporal stability when central difference schemes are used to approximate the spatial derivatives. The coefficients for these schemes are listed in table (3.1) and (3.2). From equation (3.15), it can easily be derived that the coefficients in the third-order polynomial are periodic in the longitudinal wave number $\alpha = k \cos \theta$ with period $\frac{2\pi}{\Delta x}$ and in the transverse wave number $\beta = k \sin \theta$ with period $\frac{2\pi}{\Delta y}$. Therefore, we only have to investigate the temporal stability for waves with wave numbers and wave angles that satisfy

$$-\frac{1}{2} < \widehat{\alpha} \leq \frac{1}{2} \quad \cup \quad -\frac{1}{2} < \widehat{\beta} \leq \frac{1}{2} \quad (3.16)$$

When central difference schemes are used this area can even be reduced further, because the coefficients in the dispersion polynomial are even functions of $\widehat{\alpha}$ and $\widehat{\beta}$. This means that the area we have to investigate is the rectangular area $0 \leq \widehat{\alpha} \leq \frac{1}{2}$ and $0 \leq \widehat{\beta} \leq \frac{1}{2}$. Straight lines starting in the origin of the $\widehat{\alpha}, \widehat{\beta}$ -plane correspond to waves with the same wave angle, circles around the origin correspond to waves with the same wave number. Given a wave number and wave angle that lie in this area, the three roots of the dispersion polynomial can be calculated, after which we can conclude whether the temporal-stability criterion is satisfied. It is not possible to calculate all three roots of the polynomial analytically, so first one root is approximated by using Newton's method, after which the two remaining roots can be calculated. The temporal stability, at fixed values of $\widehat{\alpha}$ and $\widehat{\beta}$, only depends on the non-dimensional parameters

$$Fn = \frac{U}{\sqrt{gL}}, \quad Fn_{\Delta x} = \frac{U}{\sqrt{g\Delta x}}, \quad \widehat{T} = \sqrt{\frac{L}{g\Delta t^2}}, \quad \kappa = \frac{\Delta y}{\Delta x}, \quad \mu = \frac{z_{fs}}{\sqrt{\Delta x \Delta y}}$$

It turns out that the last two parameters have hardly any influence on the temporal stability, so we will only use $\kappa = 1$ and $\mu = 1$ here.

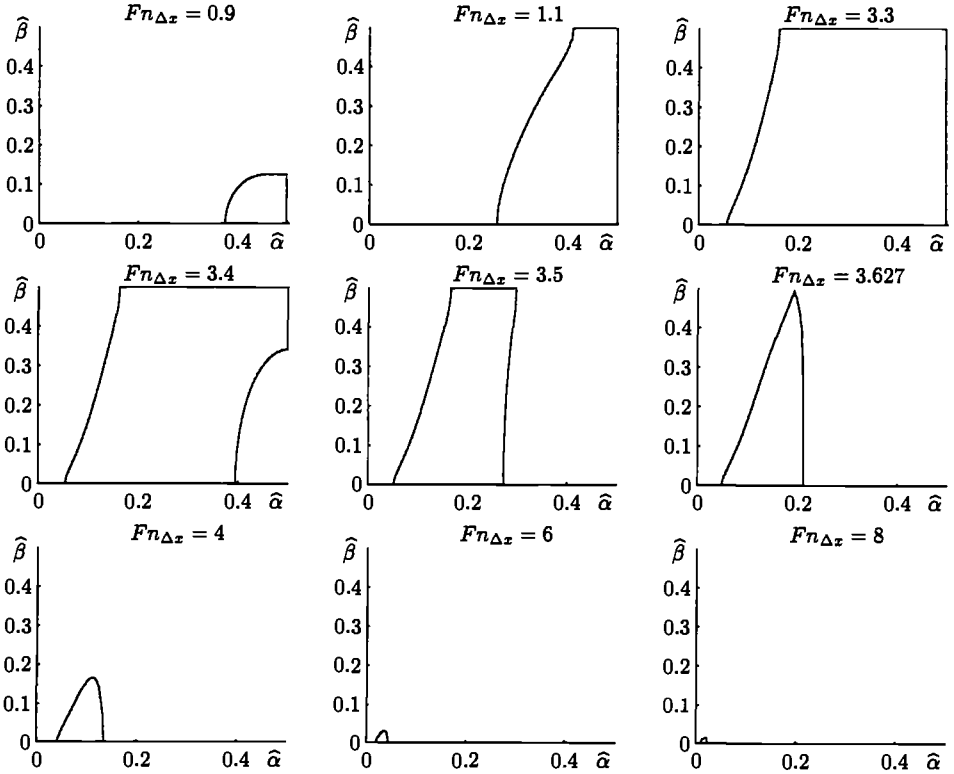


Figure 3.16: Regions in the $\hat{\alpha}, \hat{\beta}$ -plane in which the dispersion relation has at least one root with modulus larger than one, for $F_n = 0.2$, $\Delta t = 0.01$ and several grid Froude numbers.

Figure 3.16 shows the stability regions for several grid Froude numbers $F_{n\Delta x}$, a Froude number of 0.2 and a time step $\Delta t = 0.01$. In the shaded regions one or more roots were found with modulus larger than one, so the shaded regions indicate instable wave numbers and wave directions. When the grid Froude number is very small (so a large panel size), no instabilities are found because almost all information about the waves is lost and they damp very fast. When the grid Froude number is increased, a small region appears where instabilities are found. This region first becomes larger when the grid Froude number increases and finally disappears when the grid Froude number is very large, corresponding to an extremely small panel size that can never be used in practice. It can be concluded that the use of central difference schemes at a Froude number of 0.2 always leads to instabilities at some wave number and wave angle, except for extremely coarse or fine grids. Of course there is also a dependence on the time step, which will be examined later. A numerical scheme is defined to be temporally stable if in the total

region (3.16) no points occur where the dispersion polynomial has a root with modulus larger than one. This means that in figure 3.16 all shown grid Froude numbers lead to an instable numerical scheme.

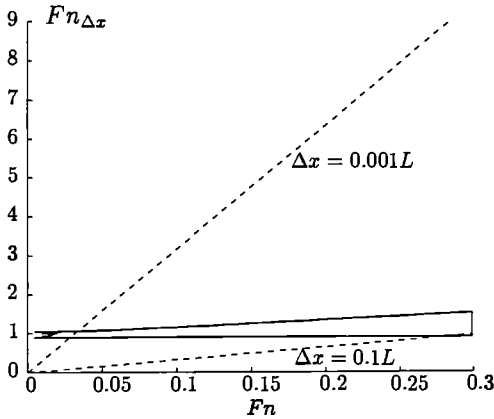


Figure 3.17: Instability region for $\Delta t = 0.1$ if we use central difference schemes.

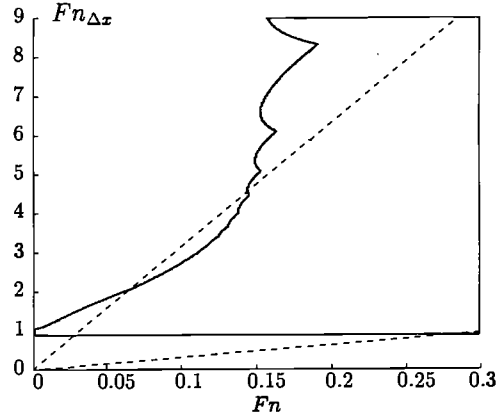


Figure 3.18: Instability region for $\Delta t = 0.01$ if we use central difference schemes.

It is possible to repeat this calculation for several Froude numbers and grid Froude numbers at a certain value of the time step Δt (or \hat{T}). If we shade the region where, for at least one value of $\hat{\alpha}$ and $\hat{\beta}$, instabilities are found, we obtain an instability region that only depends on the time step. We did this for three values of the time step, namely $\Delta t = 0.1$, $\Delta t = 0.01$ and $\Delta t = 0.001$. The results are shown in figures 3.17, 3.18 and 3.19. In these figures the two straight broken lines combine points that have panel size $\Delta x = 0.1L$ and $\Delta x = 0.001L$. These lines have been drawn because in practice the panel size always lies between these two values, so the area between these two lines is our area of interest. $\Delta x = 0.1L$ corresponds to a very coarse grid with only 10 panels along the waterline of the ship. $\Delta x = 0.001L$ corresponds to a very fine grid with 1000 panels along the waterline of the ship. When the time step is large, $\Delta t = 0.1$, the instability region is quite small. This can be explained by the fact that only low-frequency waves can be represented accurately, so the high-frequency waves damp fast. When the time step is decreased to $\Delta t = 0.01$, more instabilities are found which are for a large part located in our area of interest. Finally, if the time step is reduced further to $\Delta t = 0.001$, almost every choice of Froude number and grid Froude number leads to instabilities. From these figures we may conclude that it is completely safe to use central difference schemes up to a Froude number of 0.03. Above that, fine discretizations lead to instabilities. It seems that, independent of the time step, the numerical scheme becomes unstable at a grid Froude number $F n_{\Delta x} \approx 0.9$.

In the final figure we see what happens when we use 50% central and 50% upwind difference schemes with a time step $\Delta t = 0.001$. The instability region becomes smaller, but is still very large. It turns out that, no matter how small the contribution of the central

difference scheme is, its use always causes instabilities for large Froude numbers. If only upwind difference schemes are used, no instabilities are found at all.

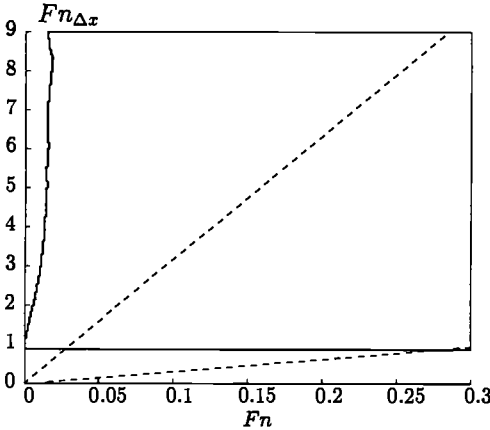


Figure 3.19: Instability region for $\Delta t = 0.001$ if we use central derivatives.

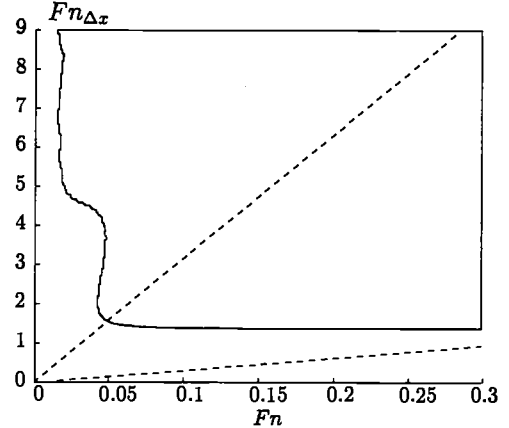


Figure 3.20: Instability region for $\Delta t = 0.001$ if we use 50% central and 50% upwind difference schemes.

3.6 Summary and conclusions

For a simplified model, in which we approximated the steady flow by the uniform flow instead of the non-linear flow, we derived a continuous and discrete dispersion relation. The solutions of these dispersion relations say something about the length and the amplitude of the predicted waves. Any differences between the solutions of the continuous dispersion relation and those of the discrete dispersion relation indicate errors due to the discretization of the free surface, the source distribution and the free-surface condition. Therefore, these differences tell us how accurate our numerical scheme is.

Besides the accuracy, the temporal stability of the numerical scheme can be investigated by considering the rate at which the solution grows in each time step. If the rate of growth is larger than one, the numerical scheme is temporally unstable, else it is temporally stable. This growth rate can be derived from the discrete dispersion relation. It turns out that, if central difference schemes are used, the numerical scheme easily becomes temporally unstable, especially for moderate and high speeds, whereas the use of upwind difference schemes never leads to instabilities. Because of these considerations, we will only use upwind difference schemes in the calculations in chapter 4 and chapter 5.

Chapter 4

Test case

In this chapter we test the model with a fictitious test ship, sailing at a Froude number of 0.35, which hull paneling is described analytically with a formula. The grid dependence of the steady free-surface velocities and their derivatives is investigated, as well as the grid dependence of the unsteady wave elevation and its dependence upon the time step. Also, the dependence of the time-dependent force on the hull paneling is considered. A comparison is made between two methods for simulating incoming waves of which the best is used in the remaining calculations in this thesis. Finally, the effect of the transfer term on the wave pattern and on the drift forces and moments is investigated.

4.1 Introduction

Before we simulate the behaviour of a commercial tanker in waves, we apply our algorithm to a fictitious test ship. This way any possible errors in our model can be eliminated, and it can be tested under severe conditions. Because this ship does not really exist, we cannot compare the predictions with measurements, so the calculations in this chapter do not say anything about the ability of our model to simulate reality.

By reducing the grid size on the hull or the free surface, we can investigate the convergence of the solution, both in the steady and the unsteady case. In the steady case we investigate the convergence of the free-surface velocities, calculated by RAPID, and the derivatives of these velocities, calculated with the difference schemes that were introduced in chapter 2. In the unsteady case we investigate the convergence of the wave pattern when the free-surface grid and the time step are refined, and the convergence of the unsteady forces on the ship in waves when the hull grid is refined.

The ship that we use in these test simulations is generated by the formulas in figure 4.1 where L is the length of the ship, B its breadth and d its draught. The use of this formula makes it easy to generate the grid and to differentiate numerically over the hull. In all calculations in this chapter we use the following values of length, breadth and draught

$$L = 1 \quad B = 0.2 \quad d = 0.1$$

Every transverse cross-section of the ship is an ellipse, and the intersection of the ship with the calm-water plane is a fourth-order polynomial, such that its tangent is parallel

$$\left(\frac{z}{d}\right)^2 + \left(\frac{y}{b(x)}\right)^2 = 1$$

$$b(x) = \frac{B}{2} \left(1 - 8 \left(\frac{x}{L}\right)^2 + 16 \left(\frac{x}{L}\right)^4\right)$$

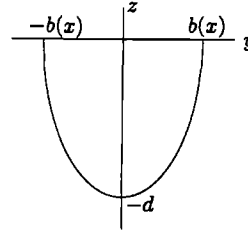


Figure 4.1: Cross section of the test ship

to the x -axis at $x = \pm \frac{L}{2}$ and $x = 0$. Of course this ship does not exist in reality and therefore we will not try to predict the motions of the ship when it freely floats in waves. We are not sure what will happen to this ship anyway when it sails in waves. It may even be unstable and capsize the moment a wave hits the ship. We will only use this ship to test whether our numerical algorithm is correct and whether the predicted steady, diffracted and incoming waves and the forces converge.

With this formula, a hull paneling was generated that has 40 panels along the (starboard) waterline and 17 panels at each of the 40 corresponding transverse cross sections of the ship, resulting in a total of 680 panels.

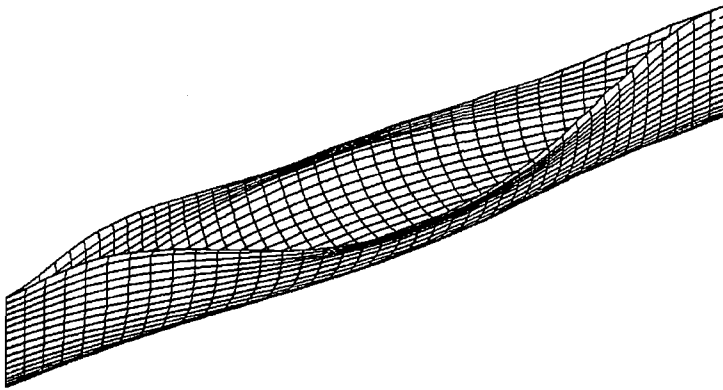


Figure 4.2: Hull paneling of the test ship, $Fn = 0.35$, 680 panels on half hull.

RAPID was used to calculate the steady flow field around this hull at $Fn = 0.35$, which resulted in the adjusted hull paneling shown in figure 4.2. Note that the top 6 panels at each cross section have been stretched or shrunk in order to follow the contour of the steady wave that intersects with the hull. Because RAPID uses raised panels, the top panels are (partly) located above the steady waterline, and used to connect the hull panels and the raised free-surface panels.

Figure 4.3 shows a top view of the steady wave pattern on an area stretching from

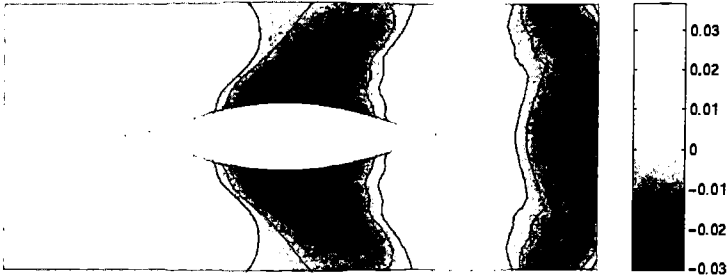


Figure 4.3: Top view of the scaled steady wave pattern, $\frac{\zeta_a}{L}$, at $Fn = 0.35$.

$x = -0.8L$ to $x = 0.9L$, and from $y = -0.4L$ to $y = 0.4L$. RAPID used 16 free-surface strips in the upper half of this area, and each strip had approximately 30 panels per wavelength, resulting in 67 panels per strip. Because of the beak-like shape of the bow, no waves are generated there, but slightly further downstream, where the hull becomes bulbous. This bulbous shape is the reason that very high waves are generated, resulting in a very high wave resistance. This makes the ship useless from a ship builder's point of view, but for testing the convergence of our predictions it is perfect.

4.2 Convergence of steady velocities and their derivatives

Before we calculate the time-dependent flow, it is important to know if the correct steady velocities and their derivatives are used in the free-surface condition (1.12). Therefore, we test whether the velocities, the derivatives of the squared velocity and the transfer term converge by looking at their grid dependence, and the dependence on the vertical distance involved in calculating the vertical derivative. As indicated by Raven [29], the dependence of the steady waves on the hull paneling is very small, so we do not consider refining the grid on the hull. In all the calculations, the Froude number was 0.35, which is about the highest Froude number at which RAPID can calculate a convergent solution for this ship.

We investigate the convergence by comparing the steady flow at two different free-surface grids: one with 30 panels per principal wavelength, $\lambda = 2\pi Fn^2$, and one with 60 panels per principal wavelength. We only refine the grid in the longitudinal direction, because this enables us to compare the results on the same strip of collocation points. If the grid had also been refined in the transverse direction, the collocation points would also have shifted in the transverse direction, making a direct comparison difficult. Moreover, the dependence of the steady velocities on the longitudinal grid size is far more important than the dependence on the transverse grid size because of the numerical differentiation in RAPID along the stream lines. Large differences between the results for the two grids indicate divergence, and the divergent terms must be eliminated from our unsteady free-

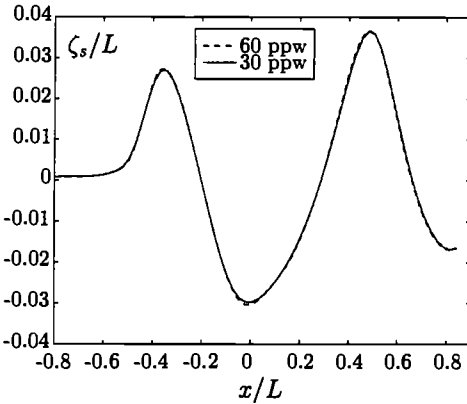


Figure 4.4: Steady wave pattern on strip of collocation points closest to the ship.

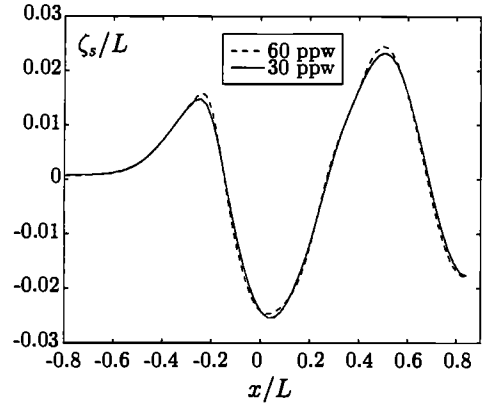


Figure 4.5: Steady wave pattern on strip of collocation points at $\frac{\Delta y}{L} \approx 0.105$.

surface condition because they also introduce errors in the unsteady waves. The dependence of the vertical derivative on the distance Δz between adjacent planes is investigated by halving this distance. This is only done for the coarsest grid.

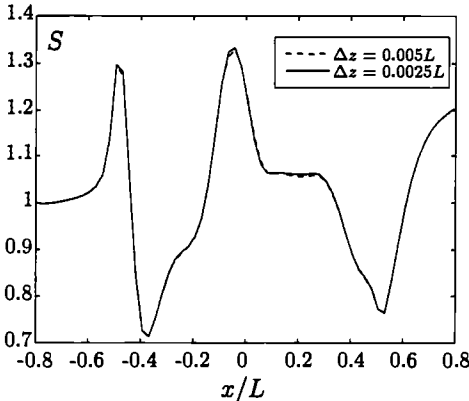


Figure 4.6: The function S on the strip of collocation points closest to the ship for two values of Δz and 30 panels per wavelength.

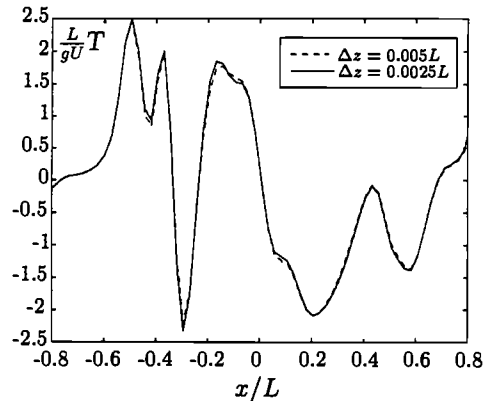


Figure 4.7: The transfer term on the strip of collocation points closest to the ship for two values of Δz and 30 panels per wavelength.

Figure 4.4 shows the steady wave pattern on the strip of collocation points that lies closest to the ship, for both grids. These collocation points lie at a distance of approximately $\Delta y \approx 0.009L$ metres from the ship or the x -axis. Figure 4.5 also shows the steady wave pattern, but now at a distance $\Delta y \approx 0.105L$. In both cases the difference between the two predicted waves is very small. The further away from the ship, the larger the difference in the wave pattern will be due to differences in numerical damping and dispersion between the two grids. This explains why figure 4.5 shows more differences than figure 4.4, especially near the wave crests and wave troughs.

To investigate the dependence of the vertical derivatives on the vertical distance Δz between adjacent planes, see figure 2.5, we calculated the function S (2.7), and the transfer term T (2.6) on the coarsest grid and with two values of Δz , namely $\Delta z = 0.0025L$ and $\Delta z = 0.005L$. In chapter 2 we showed that S and can be calculated accurately if $(k\Delta z)^2 \ll 1$ and T if $(\Delta z)^2 Lk^3 \ll 1$. The mentioned vertical distances easily fulfill this condition. Figure 4.6 shows the function S on the strip of collocation points closest to the ship. Almost no differences can be seen between the two predictions, which indicates that the vertical derivative in (2.7) converges very well if the grid size stays the same. The same holds for the vertical derivative in the transfer term, as can be seen in figure 4.7.

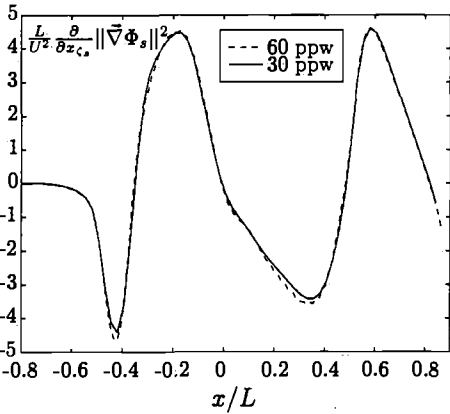


Figure 4.8: Longitudinal derivative of squared velocity on the strip of collocation points closest to the ship.

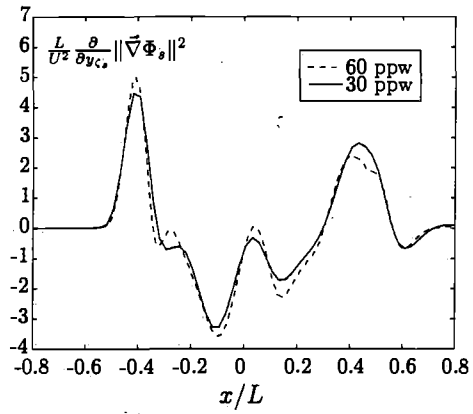


Figure 4.9: Transverse derivative of squared velocity on the strip of collocation points closest to the ship.

Next, we investigate what happens to the derivatives of the steady velocity if the vertical distance Δz is kept constant and the longitudinal grid size is halved. Figure 4.8 shows the longitudinal derivative of the squared velocity when 30 or 60 panels per wavelength are used. Almost no differences can be seen between the two predictions, which indicates a very good convergence of this derivative. Figure 4.9 shows the transverse derivative when 30 or 60 panels per wavelength are used. Unlike in the previous figure, we observe some differences between the two predictions here, especially near the peak values. This may be explained by the fact that we obtained the transverse derivative with a difference scheme, whereas we obtained the longitudinal derivative mainly from the steady free-surface condition (1.5), which method gives more accurate results. However, the differences between the plots are not large, so we can use these derivatives in the unsteady free-surface condition without problems.

Now that we know that the first derivatives of the steady velocities can be calculated quite accurately, it is time to go one step further and to investigate the convergence of the transfer term, which contains a second derivative of the steady velocities. Figure

4.10 shows the transfer term on the strip of collocation points closest to the ship. Unfortunately, large differences between the two predictions can be seen, especially in the midship region. The same holds for the transfer term somewhat further away from the ship. It seems that for this ship, which is of course an extreme case, considering its speed and its bulbous shape, the transfer term cannot be calculated accurately on the entire free surface. If we want to eliminate the transfer term from the unsteady free-surface condition, we have to investigate the influence this term has on the unsteady solution, which will be done later on.

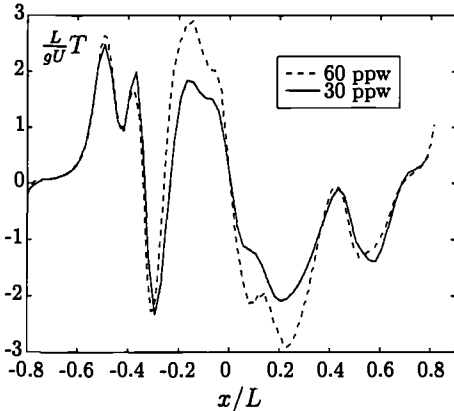


Figure 4.10: The transfer term on the strip of collocation points closest to the ship for 30 and 60 panels per wavelength, $\Delta z = 0.005L$.

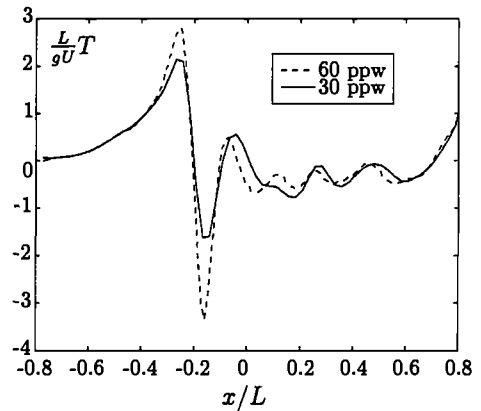


Figure 4.11: The transfer term on $\frac{\Delta y}{L} \approx 0.105$ for 30 and 60 panels per wavelength, $\Delta z = 0.005L$.

4.3 Modeling incoming waves

If we are to calculate the motions of a ship and the drift forces on it, including an accurate description of the incoming waves is very important. There are two methods to simulate the incoming waves, which both have their advantages and their disadvantages. We will compare the two methods by applying them to our model and by looking at the predicted wave elevation. If the predicted wave elevation is almost the same, then both methods can be used and we can choose the one that suits us best.

The first method to simulate incoming waves is to generate them with a numerical wave maker. During the simulation the incoming wave propagates towards the ship, reaches the ship, and at that moment we can determine the motions and the drift forces. The advantage of this approach is that we simulate what happens in reality when a ship sails in calm water and then suddenly encounters incoming waves, and what happens during the measurements in the towing tanks at the MARIN, where wave makers are used to generate waves. Therefore, if the waves do not suffer too severely from numerical damping or dispersion, this approach most likely produces correct results. A disadvantage of this

approach is that a very fine grid has to be used on the side of the ship where the waves come from to avoid numerical errors in the incoming wave before it has even reached the ship. Furthermore, the simulation must be run for quite a long time because it takes some time before the wave reaches the ship. We will refer to this method as the wave-maker method.

The second method is to calculate only the diffracted wave. This means that we assume that, in the entire fluid domain, we can split the time-dependent velocity potential in two separate parts: the undisturbed incoming potential, and a disturbance called the diffracted potential

$$\phi = \phi_{inc} + \phi_{dif}$$

This approach is always used in frequency-domain models. The incoming-wave potential is given in equation (2.13). Of course a radiation potential must be added in case of ship motions, but as said, these are not considered here. If we reduce the boundary conditions on the steady free surface and the hull of the ship into

$$L_i \phi = 0 \quad i = 1, 2$$

where L_i is a linear operator, then these boundary conditions change into

$$L_i \phi_{dif} = -L_i \phi_{inc} \quad i = 1, 2$$

We see that the presence of the incoming wave leads to a forcing function on the right-hand side of the boundary conditions. This means that we have to apply the linear operator L_i to the incoming-wave potential. Far away from the ship, the steady flow is uniform and the incoming-wave potential satisfies the free-surface condition, so the right-hand side of the free-surface condition is then zero. Close to the ship, the steady flow is far from uniform and the incoming-wave potential does not satisfy the free-surface condition at all. In fact, the incoming-wave potential is based on a linearization about the calm-water plane, whereas if we use it near the ship, we apply it to a condition on the non-linear, non-flat, steady wave. It is therefore not sure that using this method is valid. We hope, however, that all inaccuracies that enter our boundary condition are corrected in the diffracted wave. So separately, the diffracted wave and the incoming wave do not represent physical waves near the ship, but the sum of the two probably does. We will refer to this method as the separation method.

Both methods have been implemented in our program and have been applied to the test ship. The wave maker was simulated by letting the unsteady potential equal the incoming-wave potential on the last two rows of collocation points on the upstream edge of the free surface, and on a vertical boundary of sufficient depth that starts at this edge. We only consider head waves in the comparison, but of course both methods are capable of simulating other wave directions as well. In all calculations the same free-surface grid was used, which stretched from $x = -L$ to $x = L$, and from $y = 0$ or the waterline of the ship to $y = 0.75L$. It was divided into 24 strips of 117 panels.

Because we consider incoming waves at one particular length λ and the corresponding encounter frequency ω , eventually the total first-order wave elevation will oscillate at the same frequency. We assume it can be written as

$$\zeta_u^{(1)} = A_c \cos \omega t + A_s \sin \omega t$$

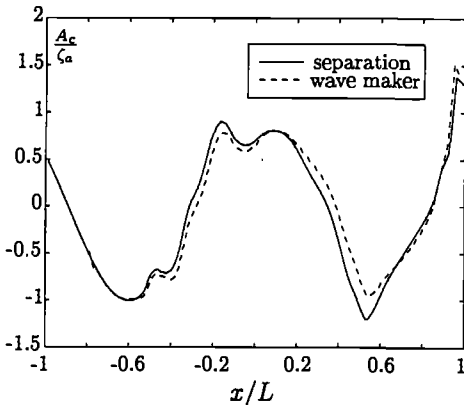


Figure 4.12: Cosine part of the wave on the strip of collocation points closest to the ship when the separation method or the wave-maker method is used, $\lambda = 1.188L$.

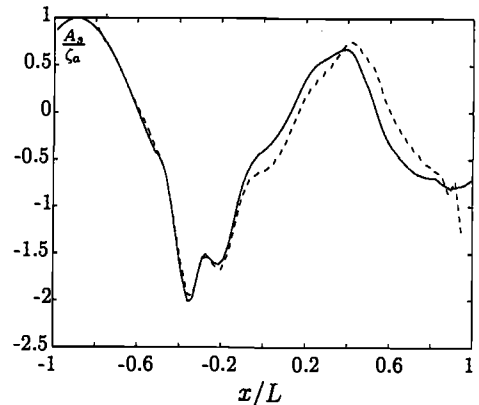


Figure 4.13: Sine part of the wave on the strip of collocation points closest to the ship when the separation method or the wave-maker method is used, $\lambda = 1.188L$. Legend as in figure 4.12.

Figures 4.12 and 4.13 show the cosine part of the wave pattern, A_c , and the sine part, A_s , of the wave pattern near the ship, both scaled with the amplitude of the incoming wave, ζ_a . The incoming wave has length $\lambda = 1.188L$. A good agreement between the two methods is found. When the wave-maker method is used, the incoming wave already contains small errors when it reaches the ship. These errors mount when the wave propagates downstream and this explains why larger differences between the two predicted waves are found further downstream. When the separation method is used, the wave in front of the ship is predicted exactly (in linear theory) and only the diffracted part of the wave suffers from numerical damping and dispersion. On the downstream end of the free surface differences occur due to the sudden truncation, which influences long waves more than short waves. The agreement between the two methods justifies the assumption that both methods can properly simulate the incoming waves.

Figures 4.14 and 4.15 show again the predicted wave pattern, but now for a shorter incoming wave with length $\lambda = 0.764L$. There is more damping and dispersion because the number of panels per wavelength is smaller than in the previous case, so the differences between the predictions are larger than those in the previous case. Again, these become larger as the wave propagates downstream. A shift between the waves can clearly be seen (dispersion) and, especially behind the ship, differences between the wave amplitudes

(damping) can be observed.

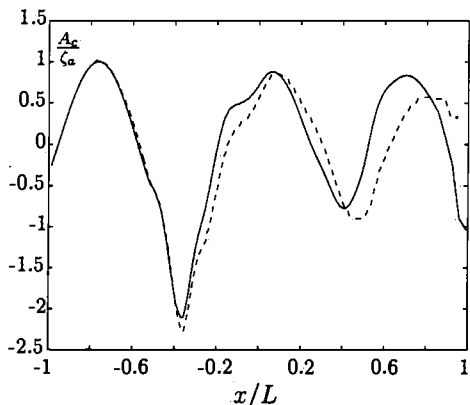


Figure 4.14: Cosine part of the wave on the strip of collocation points closest to the ship when the separation method or the wave-maker method is used, $\lambda = 0.764L$. Legend as in in figure 4.12.

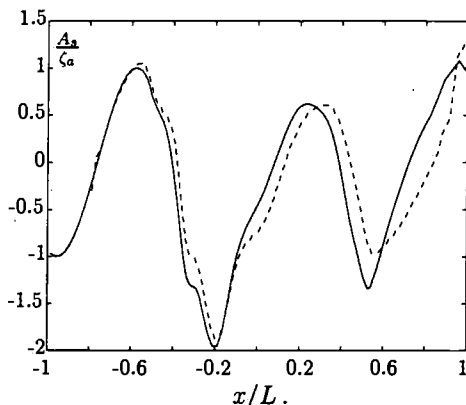


Figure 4.15: Sine part of the wave on the strip of collocation points closest to the ship when the separation method or the wave-maker method is used, $\lambda = 0.764L$. Legend as in in figure 4.12.

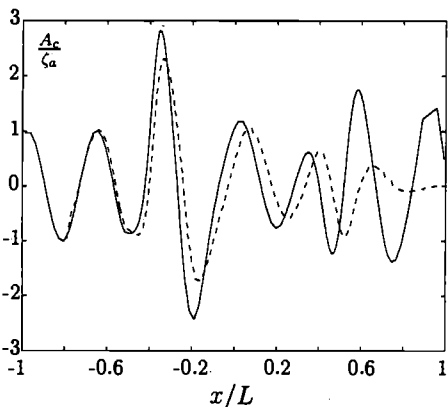


Figure 4.16: Cosine part of the wave on the strip of collocation points closest to the ship when the separation method or the wave-maker method is used, $\lambda = 0.325L$. Legend as in in figure 4.12.

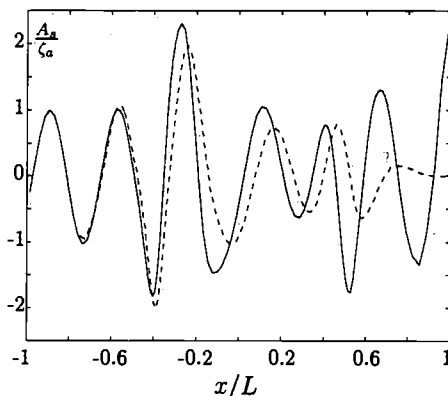


Figure 4.17: Sine part of the wave on the strip of collocation points closest to the ship when the separation method or the wave-maker method is used, $\lambda = 0.325L$. Legend as in in figure 4.12.

Finally, we compare the wave pattern for an incoming wave having length $\lambda = 0.325L$. This is quite a short wave, corresponding to an average of about 19 panels per wavelength. Because the grid is non-uniform, in some areas (midships and downstream of the ship) only 10 panels per wavelength are used, whereas near the bow and the stern about 29

panels per wavelength are used. This explains why in figures 4.16 and 4.17 large differences between the wave patterns can be seen. Both methods give unreliable results for short waves and this can only be solved by using more panels. Unfortunately, this is not possible right now because the memory of the workstations that we use limits the total number of panels to about 3500.

We may conclude that, if sufficient panels per wavelength are used, both methods give similar predictions for the incoming and diffracted waves. If, due to limited computer memory, only a small number of panels per wavelength can be taken into account, both methods result in waves with errors due to numerical damping and dispersion. In that case, the separation method is the most reliable because only the diffracted part of the wave contains numerical errors. Furthermore, the separation method requires less panels because we can use a panel size that is quite large on the upstream side of the ship, and because no vertical boundary is needed to generate waves. Finally, the separation method requires less simulation time than the wave-maker method because the incoming wave does not have to propagate from the wave maker to the ship. Therefore, we use the separation method in the rest of the calculations in this thesis.

4.4 Convergence of unsteady waves and forces

When a numerical method gives a solution, this does not automatically mean that this solution is correct. Errors in discretization or a discretization with a too low accuracy may lead to non-convergence if a finer mesh or time step is used. Therefore, we test whether the numerical solution converges by comparing the unsteady wave elevation computed with several free-surface grids and with several time steps. A convergence test is made for the combination of incoming and diffracted waves near the waterline of the ship and for a transverse wave cut after a forced heave motion. The dependence of the unsteady forces on the hull grid is also investigated. In all calculations the Froude number is 0.35 again.

First, we investigate the dependence of the unsteady wave profile near the hull on the free-surface paneling, without changing the hull paneling. For that purpose, we calculated the wave profile in incoming head waves with a length $\lambda = 1.188L$, then $\lambda = 0.764L$ and finally $\lambda = 0.325L$. In the first two cases use was made of a damping zone on the side of the ship in the area $0.4L < y < 0.75L$, which was divided in eight strips. In the last case, the use of a damping zone was no longer necessary due to the angle of the diffracted waves. This enabled us to refine the grid further. The area between $y = 0$ or the waterline of the ship, and $y = 0.4L$ was divided in 16 free-surface strips. Each strip extended from $x = -L$ to $x = L$. In the first two cases ($\lambda = 1.188L$, $\lambda = 0.764L$), each strip was divided in 115, then in 59 and finally in 32 panels. In the last case ($\lambda = 0.325L$), each strip was divided in 176, then in 115 and finally in 59 panels. On the hull, the paneling shown in figure 4.2 was used, containing 680 panels. As said before, ship motions are not considered.

Figures 4.18 and 4.19 show the cosine part of the wave pattern, A_c , and the sine part, A_s ,

on the strip of collocation points closest to the ship for an incoming wave having length $\lambda = 1.188L$. Because the dispersion relation has two real roots if the wave angle is zero, the diffracted wave has two downstream wave components. One component has length $\lambda = 1.188L$, like the incoming wave, and one has length $\lambda = 0.236L$. Because $\tau \gg 0.25$, waves do not propagate upstream. The coarsest discretization corresponds to an average of 19 panels per incoming-wave length, the discretization with 59 panels to an average of 35 panels per incoming-wave length, and the finest discretization to an average of 68 panels per incoming-wave length. Of course the grid is not uniform, and near the bow and the stern of the ship the panel size is three times as small as that on the upstream and downstream side of the computational domain. Also, we must realize that we need at least 10 to 15 panels per steady wavelength ($2\pi F\tau^2$) to represent the steady wave, and preferably much more. The coarsest discretization has about 12 panels per steady wavelength, so this requirement is only just fulfilled.

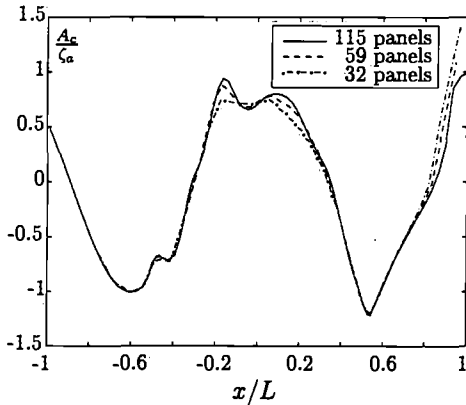


Figure 4.18: Cosine part of the incoming and diffracted wave on the strip of collocation points closest to the ship if 115, 59 and 32 panels are used, $\lambda = 1.188L$.

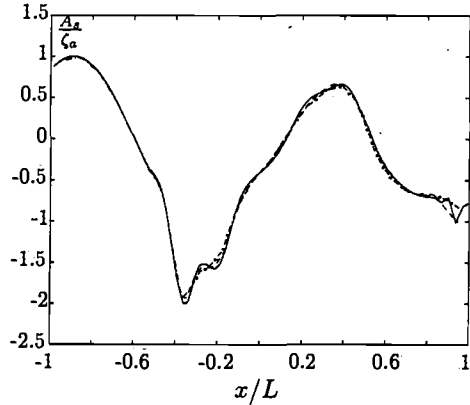


Figure 4.19: Sine part of the incoming and diffracted wave on the strip of collocation points closest to the ship if 115, 59 and 32 panels are used, $\lambda = 1.188L$. Legend as in figure 4.18.

We see that the unsteady wave pattern near the ship converges very well if more panels are used. Small differences between the three predictions can be seen near the peak values at $x = -0.2L$ and $x = 0.2L$, which is not surprising, and at the downstream edge of the computational domain. These last differences occur because the panel size in that area is larger than the average panel size, and because the truncation of the free surface has some influence on the wave pattern, especially for long waves. It seems that the short-wave component is very small because if it had not been, larger differences would have been found in the final refinement step. The incoming wave is undisturbed until it reaches the point $x \approx -0.55L$, which means that the diffracted wave does not propagate upstream, as it would not in reality.

Figures 4.20 and 4.21 show the same as figures 4.18 and 4.19, but for a shorter wavelength $\lambda = 0.764L$. Now, the diffracted wave also contains a component with length $\lambda = 0.192L$. Again, a very good agreement is found between the wave pattern on the coarse and the fine grids. This is remarkable because the coarsest grid corresponds to an average of only 12 panels per incoming-wave length. The other two grids correspond to 23 and 44 panels per incoming-wave length. Our numerical scheme is apparently very accurate and only a small number of panels per unsteady-wave length have to be taken into account, as long as the steady wave is represented accurately as well. Notice that the further downstream, the larger the differences between the two waves become because the errors mount. Due to damping and dispersion, the error becomes larger when the distance over which the wave propagates becomes larger. Again, the short-wave component seems to be very small.

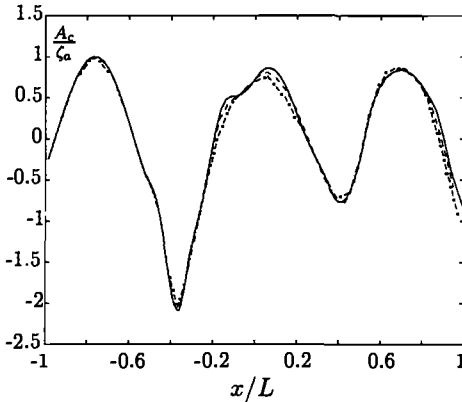


Figure 4.20: Cosine part of the incoming and diffracted wave on the strip of collocation points closest to the ship if 115, 59 and 32 panels are used, $\lambda = 0.764L$. Legend as in in figure 4.18.

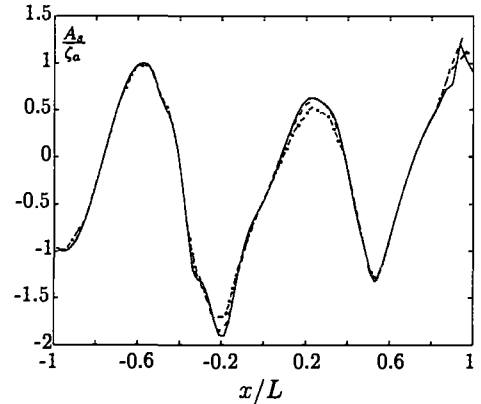


Figure 4.21: Sine part of the incoming and diffracted wave on the strip of collocation points closest to the ship if 115, 59 and 32 panels are used, $\lambda = 0.764L$. Legend as in in figure 4.18.

We also calculated the incoming and diffracted wave for an incoming wave having length $\lambda = 0.325L$. Because this is a short wave, we used more panels in the convergence study. To accomplish this, we had to remove the damping zone and use these extra panels to refine the grid further. The damping zone is redundant at this wavelength because the wave angle of the diffracted waves will be small, so any possible reflections will end up far behind the ship. Figures 4.22 and 4.23 show the resulting wave pattern when 24 strips of 59, 115 and 176 panels are used. The coarsest paneling, corresponding to 10 panels per incoming-wave length, results in large differences between the predicted waves in comparison with the other two cases, which correspond to 19 and 29 panels per wavelength. The differences between the last two cases are much smaller. Although the number of panels per wavelength is about the same, the differences between the three predicted waves at wavelength $\lambda = 0.325L$ seem to be much larger than the differences between the three predicted waves at the two longer wavelengths. This can be explained by the fact that the error in the wave depends upon the distance, relative to the wavelength,

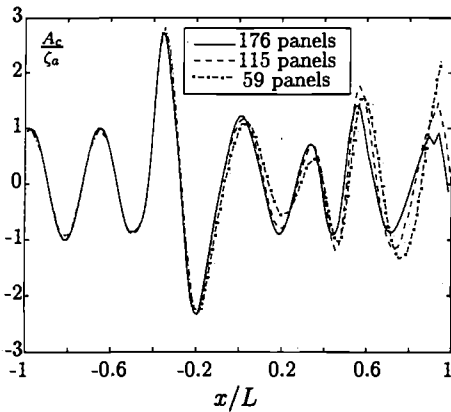


Figure 4.22: Cosine part of the incoming and diffracted wave on the strip of collocation points closest to the ship if 176, 115 and 59 panels are used, $\lambda = 0.325L$.

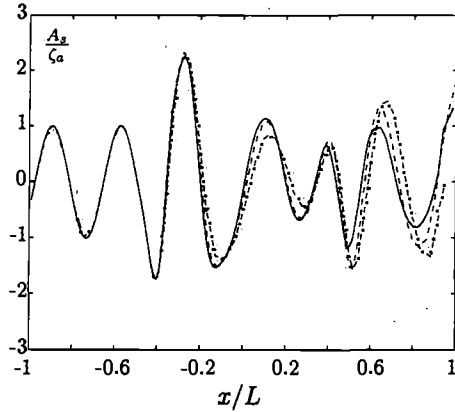


Figure 4.23: Sine part of the incoming and diffracted wave on the strip of collocation points closest to the ship if 176, 115 and 59 panels are used, $\lambda = 0.325L$. Legend as in figure 4.22.

that the wave has traveled. When a wave has traveled one wavelength, the errors in the wave will be the same, regardless its length, if the same number of panels per wavelength is used. Because relatively, a short wave travels a longer distance than a long wave, it will contain a larger error if it travels the same absolute distance.

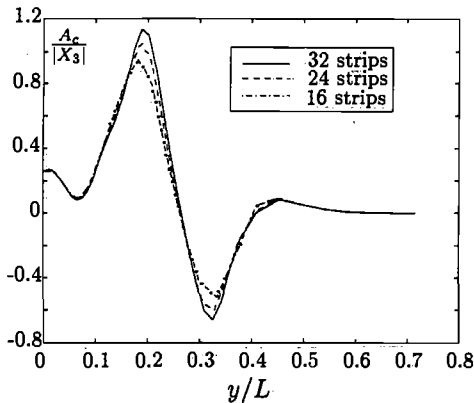


Figure 4.24: Cosine part of the wave elevation in heave at a transverse cut, $x = 0.5L$, if 32, 24 and 16 strips of 70 panels are used, $\tau = 2.01$.

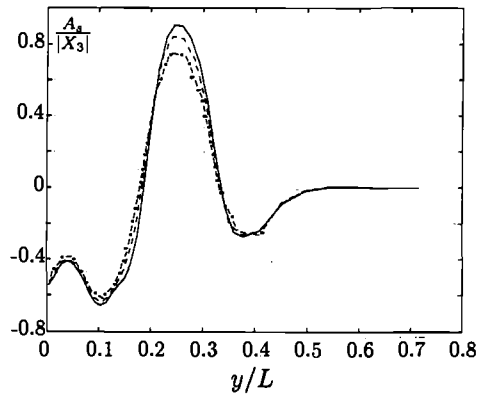


Figure 4.25: Sine part of the wave elevation in heave at a transverse cut, $x = 0.5L$, if 32, 24 and 16 strips of 70 panels are used, $\tau = 2.01$. Legend as in figure 4.24.

To investigate the influence of the transverse panel size, we force the ship to heave at a particular frequency with amplitude $|X_3|$, and look at a transverse wave cut at $x = 0.5L$,

so at the stern of the ship. Figures 4.24 and 4.25 show this transverse wave cut for 8 strips of 70 panels inside the damping zone ($y > 0.4L$), and for 32, then for 24 and finally for 16 strips of 70 panels outside the damping zone. This means that in the damping zone, the transverse panel size is not refined. The frequency of the heave motion was such that $\tau = 2.01$. At a Froude number of 0.35, this corresponds to radiated downstream waves that have a length of $\lambda = 0.764L$ and $\lambda = 0.192L$. In the area near the ship, which is the most important one because we need the wave elevation at the waterline to calculate the drift forces, the wave pattern converges very well. Further away from the ship larger differences between the predicted waves can be seen, especially near the peaks in the wave elevation. The reason for this is that the transverse panel size is not uniformly distributed. Near the ship, the transverse panel size is three times as small as near the damping zone, so less differences occur near the ship when we refine the grid.

Another important parameter in the discretization is the time step Δt . Therefore, we calculated the wave pattern again on the strip of collocation points that lies closest to the ship, with 12, 24 and 48 time steps per period. The length of the incoming wave was $\lambda = 0.5L$. 116 panels were used in longitudinal direction and 24 in transverse direction.

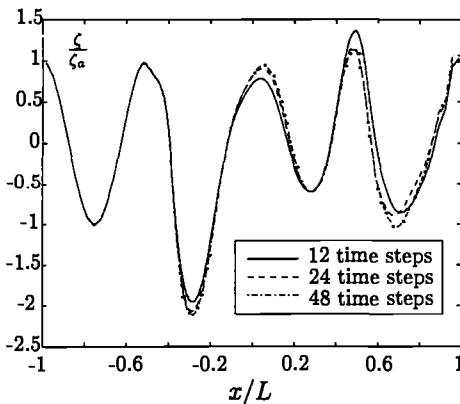


Figure 4.26: Wave pattern at $t = \frac{10\pi}{\omega}$ on the strip of collocation points closest to the ship. $\lambda = 0.5L$, 116×24 panels.

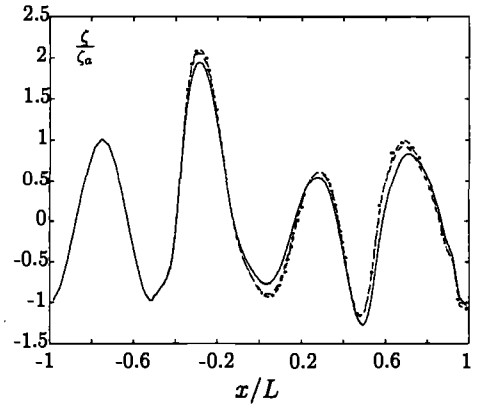


Figure 4.27: Wave pattern at $t = \frac{11\pi}{\omega}$ on the strip of collocation points closest to the ship. $\lambda = 0.5L$, 116×24 panels. Legend as in figure 4.26

Figure 4.26 shows the wave pattern at $t = \frac{10\pi}{\omega}$ and figure 4.27 the wave pattern at $t = \frac{11\pi}{\omega}$. Some small differences can be seen between the largest time step and the two other time steps. Between the two smallest time steps, only behind the ship some differences can be seen. These differences are all due to the effect of the time step on the damping and dispersion. This explains why the further downstream, the larger the differences in the wave pattern are. We also repeated the calculation with 96 time steps, but then there were no visible differences anymore. This shows that it is sufficient to use about 50 time steps per period in the calculations, something which was also observed by Prins [28], who used the same time discretization.

Now that we know the dependence of the wave pattern on the free-surface panel density and the time step, we turn our attention to the influence of hull-panel refinement. We look what happens to the predicted wave elevation and the predicted first-order forces on the ship, sailing in incoming waves, when we use three different hull panelings. First, we use the familiar hull paneling with 40 strips of 17 panels, shown in figure 4.2. We subsequently refine this paneling in the longitudinal direction along the waterline, which results in 80 strips of 17 panels. Finally, we refine the hull paneling in vertical direction, which results in 40 strips of 34 panels. In all the calculations we used the same free-surface grid, consisting of 24 strips of 88 panels in the area $-L < x < L, 0 < y < 0.75L$.

We would like to show the unsteady wave elevation, but found that there were no visible differences between the three cases. It turns out that whereas the size of the free-surface panels greatly affects the wave elevation, the influence of the panel size on the hull is small. This is because refinement of the free-surface paneling reduces damping and dispersion, whereas refinement of the hull paneling merely gives a more accurate prediction of the forces on the ship, without influencing the way the waves propagate around the ship.

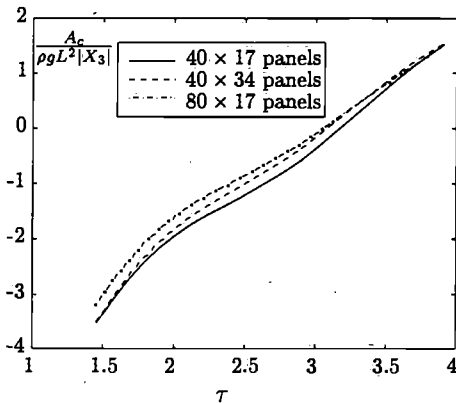


Figure 4.28: Cosine part of the heave force in bow-quartering waves if 40×17 , 40×34 and 80×17 hull panels are used.

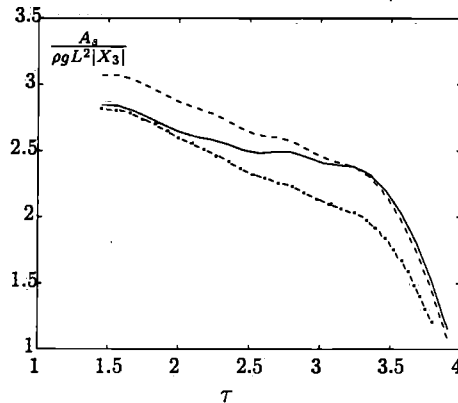


Figure 4.29: Sine part of the heave force in bow-quartering waves if 40×17 , 40×34 and 80×17 hull panels are used. Legend as in figure 4.28.

Therefore, we investigate the dependence of the forces on the hull paneling. Figures 4.28 and 4.29 show the vertical force on the ship in bow-quartering waves (wave angle 45 degrees). On the horizontal axis the value of τ is shown. $\tau = 1.5$ corresponds to a wave with length $\lambda = 0.93L$, $\tau = 4$ to a wave with length $\lambda = 0.24L$. Just as for the wave elevation, we can write for the vertical force

$$F_z = A_c \cos \omega t + A_s \sin \omega t$$

where ω is again the encounter frequency of the incoming wave. Both the cosine part and the sine part of the force show considerable differences at all wavelengths when the hull

paneling is refined. In short waves (high values of τ), the influence of the longitudinal refinement is considerable, whereas in long waves both refinements seem to have some influence. Therefore, it seems necessary to use a very accurate grid on the hull of the ship. A small error in the predicted unsteady forces leads to a similar error in the predicted motions of the ship and a possibly even larger error in the predicted drift forces and moments. Therefore, in the next chapter, we will use a more accurate grid in our calculations for the LNG carrier.

4.5 Influence of the transfer term

When we investigated the convergence of the transfer term (2.6) in section 4.2, we found that reducing the grid size resulted in substantial differences in the transfer term near the waterline of the ship. Therefore, we have to investigate whether this transfer term influences our prediction of the unsteady wave pattern and the drift forces and moments. If the influence is large, then errors in the transfer term will lead to errors in the predicted unsteady waves, so we would have to eliminate the transfer term from our equations, which would leave us with an inconsistent linearization. If the influence is small, then the local errors in the transfer term will hardly influence the wave pattern. In that case, it would be better to include the transfer term in our model because for large parts of the free surface an accurate prediction of the transfer term can still be obtained.

It is especially important to have an accurate prediction of the wave height at the bow and the stern of the ship, because these have a large influence on the predicted added resistance in waves. After all, to calculate the second-order forces and moments, we have to integrate the square of the wave elevation over the steady waterline. This contribution to the drift forces turns out to be the most important one, and a 10-percent error in the wave height can, in theory, lead to a 21-percent error in the quadratic term.

Figures 4.30 and 4.31 show the cosine and the sine part of the wave pattern for an incoming head wave having length $\lambda = 1.188L$. All calculations were done on a grid with 24 strips of 117 panels. We see that, in this case, the influence of the transfer term on the wave pattern is significant. In figure 4.30, the largest difference between the two predicted waves, about 15 percent, is found near the point $x = -0.2L$. In the second figure, a 13-percent difference can be seen near $x = -0.35L$. These are local errors; the differences are much smaller in the other regions, but still large enough to influence the predicted added resistance considerably. As said, an error in the first-order wave elevation leads to an even larger error in the predicted added resistance. Therefore, it is necessary to include the correct transfer term in our calculations. Unfortunately, for this ship and this Froude number, on certain areas on the free surface the transfer term cannot be calculated accurately from the RAPID velocities. Therefore, the predicted wave pattern is not reliable in the places where the transfer term is not reliable.

Figures 4.32 and 4.33 show the same as figures 4.30 and 4.31, but for a smaller wavelength, $\lambda = 0.764L$. Near the bow, a difference of 15 percent occurs again, whereas in other parts

along the waterline the differences are very small, so the same conclusion may be drawn as in the previous case.

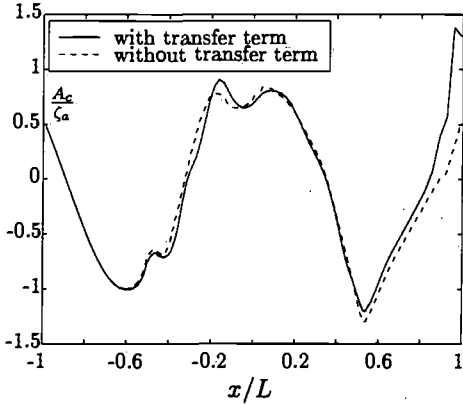


Figure 4.30: Cosine part of the incoming and diffracted wave on the strip of collocation points closest to the ship with and without the transfer term, $\lambda = 1.188L$.

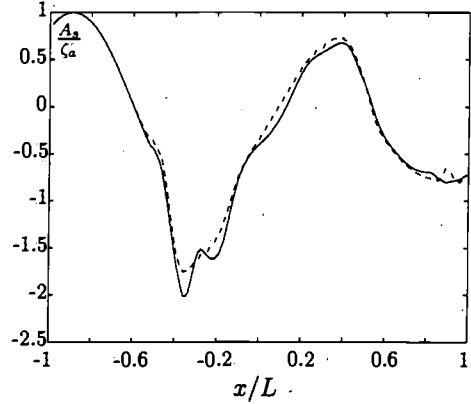


Figure 4.31: Sine part of the incoming and diffracted wave on the strip of collocation points closest to the ship with and without the transfer term, $\lambda = 1.188L$. Legend as in in figure 4.30

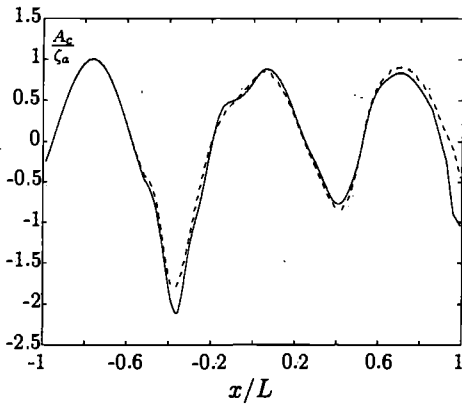


Figure 4.32: Cosine part of the incoming and diffracted wave on the strip of collocation points closest to the ship, with and without the transfer term, $\lambda = 0.764L$. Legend as in in figure 4.30.

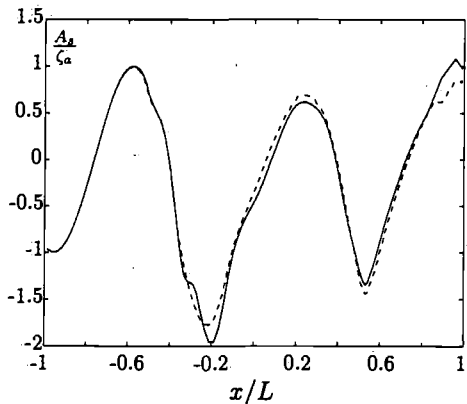


Figure 4.33: Sine part of the incoming and diffracted wave on the strip of collocation points closest to the ship, with and without the transfer term, $\lambda = 0.764L$. Legend as in in figure 4.30.

Finally, figures 4.34 and 4.35 show the wave pattern for an incoming wave having length $\lambda = 0.325L$. It seems that, independent of the length of the wave, neglecting the transfer term leads to a 15-percent difference in the wave elevation at the bow and the stern.

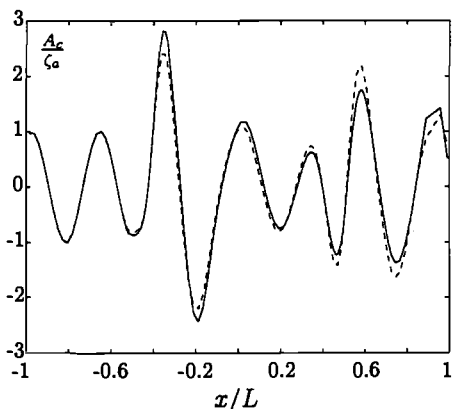


Figure 4.34: Cosine part of the incoming and diffracted wave on the strip of collocation points closest to the ship with and without the transfer term, $\lambda = 0.325L$. Legend as in figure 4.30.

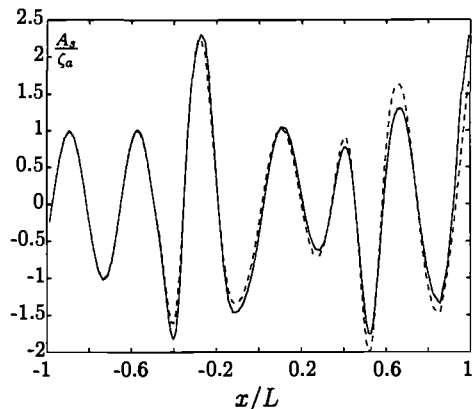


Figure 4.35: Sine part of the incoming and diffracted wave on the strip of collocation points closest to the ship with and without the transfer term, $\lambda = 0.325L$. Legend as in figure 4.30.

We have seen that the wave elevation is significantly influenced if we leave out the transfer term, so it is expected that the waterline integral in equation (1.26) will also be largely influenced if we leave out the transfer term. To investigate the influence of the transfer term on the predicted drift forces and moments, we calculated the added resistance and the pitch drift moment in head waves with and without the transfer term. Again, ship motions are not considered. Therefore, only two drift-force terms remain, namely

$$I : -\frac{1}{2}\rho \iint_{\bar{H}} \bar{\nabla} \phi_u^{(1)} \cdot \bar{\nabla} \phi_u^{(1)} \bar{n} dS, \quad II : \int_{wl} \left(\rho g + \frac{1}{2} \frac{\partial p_s}{\partial z} \Big|_{z=\zeta_s} \right) \zeta_u^{(1)2} \bar{n} dl$$

Similarly, only two drift-moment terms remain. To calculate the waterline integral, the wave elevation on this waterline is required. Because the wave elevation is only known in the collocation points on the steady free surface, we extrapolate from these collocation points to the waterline to obtain the required wave elevation.

Figure 4.36 shows the added resistance in head waves with a length ranging from $\lambda = 0.3L$ to $\lambda = 1.2L$. Because we do not consider ship motions, the added resistance has no resonance peak. Independent of the wavelength, there is a difference between the two predictions of about $\Delta F \approx 0.25$, which is 15 percent of the smallest value and 7 percent of the largest value shown in this figure. Although this is smaller than might be expected, it is still a significant difference. Figure 4.37 shows the pitch drift moment with and without the transfer term, and similar differences between the two can be seen. The heave drift force is not shown because the waterline integral is zero then (the third component of the normal vector is zero on the waterline in case of vertical side walls of the ship). We may therefore conclude that it is absolutely necessary to include an accurate prediction of the transfer term in our model. When the transfer term cannot be calculated accurately, it

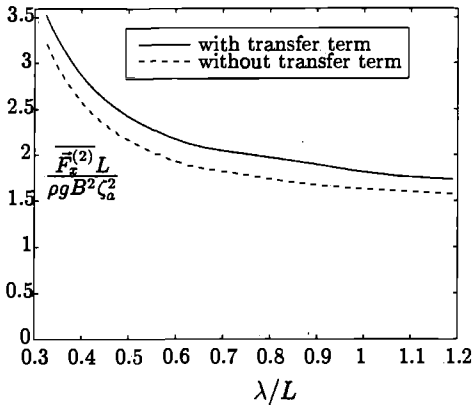


Figure 4.36: Added resistance in head waves, with and without the transfer term.

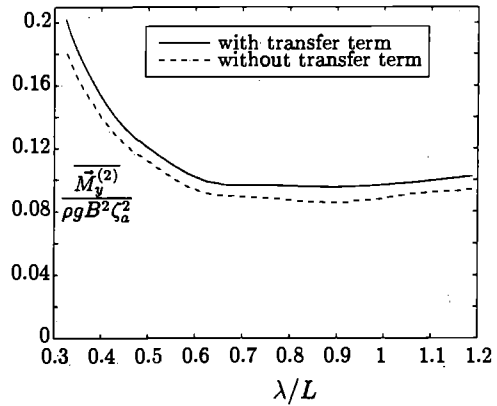


Figure 4.37: Pitch drift moment in head waves, with and without the transfer term.

cannot be left out as this is inconsistent, so the predicted drift forces and moments are simply not reliable.

4.6 Summary and conclusions

We tested our model with a fictitious ship sailing at a Froude number of 0.35. This ship and its speed were chosen such that our model could be tested under severe conditions. Because of the bulbous shape of the ship, it generates high steady waves that disturb the incoming waves significantly. The interaction between the steady and unsteady waves is described by the linearized free-surface condition. In this free-surface condition, an accurate prediction is required of the steady wave, of first derivatives of the steady velocities, and of the transfer term, which contains a second derivative of the steady velocities. Therefore, we carried out a convergence study in which we investigated the dependence of these steady quantities on the number of panels per steady wavelength. It turns out that for this ship, the steady wave pattern and the first derivatives converge very well. The transfer term, however, varies considerably, especially close to the ship, when the number of panels per wavelength is increased. The effect of the transfer term on the predicted unsteady waves and the predicted added resistance was found to be considerable, so a consistent linearization should include an accurate approximation of the transfer term.

There are two methods to simulate incoming waves in the time domain: a wave-maker method, in which waves are generated on the upstream side of the ship, and a separation method, in which only the diffracted wave is calculated. We implemented both methods and they gave similar results, except for short waves. In that case, the damping and dispersion is large for both methods because too few panels per unsteady wavelength are taken into account. Because of the limited computer memory on our workstations, this could not have been avoided. For short waves, we have to switch to a larger and faster

computer, for example the CRAY T3E at the Delft University of Technology. Because in the separation method, only the diffracted wave suffers from damping and dispersion, and because the separation method takes less simulation time and requires less panels, we use it in the remaining calculations in this thesis.

Also, we investigated the convergence of the unsteady waves. A very good agreement was found between the predicted waves when the number of panels per wavelength was increased. The largest differences between the waves occurred when short waves were simulated. The wave pattern also converged very well when we reduced the transverse panel size and the time step. The good convergence suggests that the difference schemes that we use for the space and time derivatives are accurate enough for our purposes.

Chapter 5

Results for an LNG carrier

In this chapter we apply our model to an LNG carrier sailing in water with a depth of 175 metres, at Froude numbers 0.14, 0.17 and 0.2. At the highest Froude number the convergence of the steady velocities and their derivatives is checked. The results for the motions and the drift forces in several wave conditions are compared with measurements carried out at the MARIN. To stress the necessity of our model, we show what happens when the double-body flow or the uniform flow is used instead of the non-linear steady flow.

5.1 Introduction

Natural gas is a bulky form of energy and must be concentrated before it can be transported economically. Over the years, for obvious economic reasons, the use of natural gas has increased most rapidly in zones close to production sites, such as the United States, Russia and Western Europe. This explains why, even today, only 19% of the world gas production is exported. Most exports are transported by pipeline, but gas can also be liquefied and shipped by sea in special carriers. Today, liquefied natural gas (LNG) accounts for 26% of all gas exports, and the stage is set for a large and continuing increase in the use of gas and international gas trade.

The fuel consumption of the LNG carrier accounts for a large part of the costs in this kind of transport. The fuel feeds the engines of the ship to balance the resistance at the desired service speed. In calm water, this resistance consists of a viscous resistance, air drag, and a wave resistance that is related to the excitation of the steady wave pattern. When incoming waves are encountered, the resistance increases considerably. This increase depends on the shape of the hull, the speed of the ship and the frequency, the amplitude and the angle of the incoming waves. Because the LNG carrier is built for intercontinental gas transport, all kinds of sea states may be encountered, so it is important to know the extra, or added, resistance at a wide range of lengths of the incoming wave and angles of incidence.

Therefore, we apply our model to a 125,000 m³ LNG carrier sailing at Froude numbers $F_n = 0.14$, $F_n = 0.17$ and $F_n = 0.2$ in water with a depth $h = 175$ metres. The main

particulars of the LNG carrier are listed in table 5.1. We compare our predictions for the motions of the ship and the added resistance at these Froude numbers with measurements from the MARIN. Calculations will be done for wave angles $\theta = 0$ (head waves), $\theta = \frac{\pi}{4}$ (bow-quartering waves) and $\theta = \frac{\pi}{2}$ (beam waves). We also vary the length of the incoming waves. Before we can start the simulation, we have to check whether the steady velocities and their derivatives converge by investigating their dependence on the grid size used to calculate the steady flow.

Denomination	Symbol	Unit	Value
Length	L	m	273
Breadth	B	m	42
Draught	T	m	11.5
Displacement	Δ	m^3	98740
Block coefficient	$\frac{C_B}{\Delta}$	[-]	0.749
Longitudinal centre of gravity from aft perpendicular	$\frac{AG}{L}$	m	138.66
Centre of gravity above base	$\frac{KG}{L}$	m	13.7
Longitudinal gyradius	k_{yy}	% L	24
Transverse gyradius	k_{xx}	% B	35
Natural heave period	T_z	s	9.4
Natural pitch period	T_θ	s	9.4
Natural roll period	T_ϕ	s	16

Table 5.1 : Main particulars of the LNG carrier.

5.2 Convergence of steady velocities and their derivatives

Just as we did in chapter 4 for the test ship, we investigate the convergence of the steady free-surface velocities and their derivatives by refining the longitudinal grid size. All the calculations are carried out for Froude number 0.2, because convergence at this highest Froude number most likely implies that the velocities and their derivatives also converge at the lower Froude numbers. The steady flow was first calculated on a grid that has 60 panels per steady wavelength in longitudinal direction, and then on a grid that has 120 panels per steady wavelength. To make a comparison possible, the grid size in transverse direction is the same.

Figure 5.1 shows the hull paneling that is used in the calculations. The total carrier was divided into 2380 panels, but because we make use of symmetry relations, we only used the starboard side of the ship in the calculations, leaving 1190 panels. There were 70 panels along the waterline of the ship and 17 at each frame. The panels near the bow and stern are taken smallest in order to make them represent the corresponding waves correctly. In the midship region a somewhat larger segment suffices because the hull has less curvature.

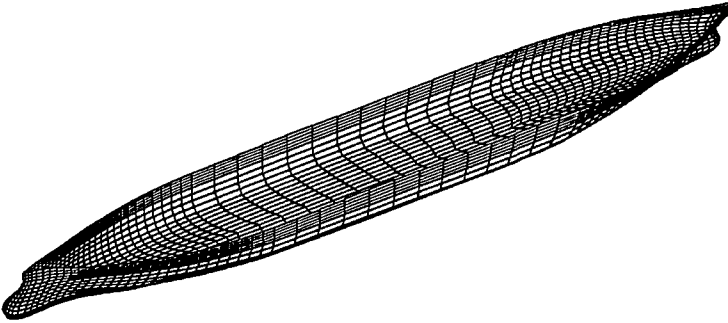


Figure 5.1: Hull paneling of LNG carrier for Froude number 0.2.

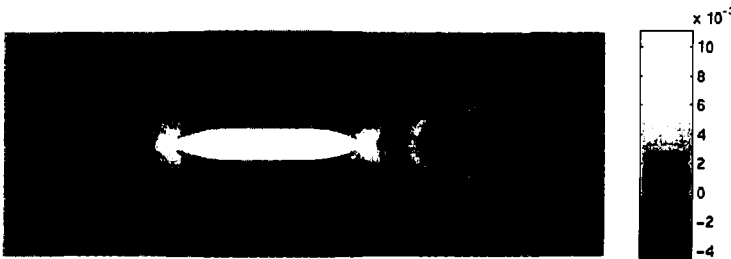


Figure 5.2: Steady wave pattern, scaled with the length of the ship, $F_n = 0.2$.

Figure 5.2 shows the steady wave pattern of the LNG carrier when it sails at Froude number $F_n = 0.2$. To calculate it, RAPID used 60 panels per wavelength, and 14 panels in transverse direction. Light areas correspond to wave crests, dark areas to wave troughs. The principal wave length $\lambda = 2\pi F_n^2$ can clearly be traced, as well as the Kelvin wave angle. By carrying out a pressure integration, one can find an estimation of the wave resistance, which turns out to be $R_w = 357.33kN$. The vertical force and the trimming moment can be used to estimate the sinkage and the trim angle. Besides the influence that trim and sinkage have on the wave resistance and the steady wave pattern, they also affect the zero-speed point of gravity, which is listed in table 5.1. The estimated trim angle of 0.05 degrees and sinkage of 0.37 metres were therefore used to calculate the correct point of gravity at $F_n = 0.2$.

The calculation with 120 panels per wavelength gave almost the same values for the resistance, trim angle and sinkage as the calculation with 60 panels per wavelength, which is a first indication of good convergence. To make sure the differences between the two predictions are indeed small, we compare their wave pattern, their derivatives of the squared velocity and their transfer term.

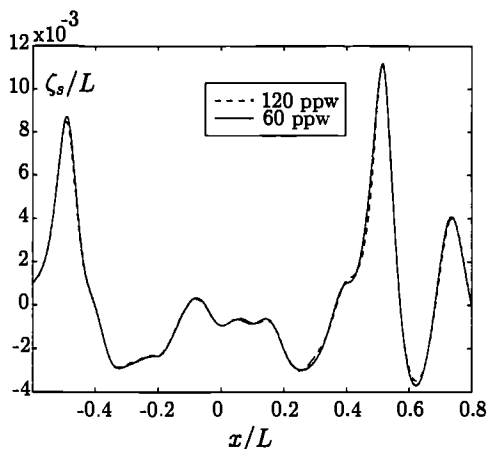


Figure 5.3: Steady wave pattern on the strip of collocation points closest to the ship.

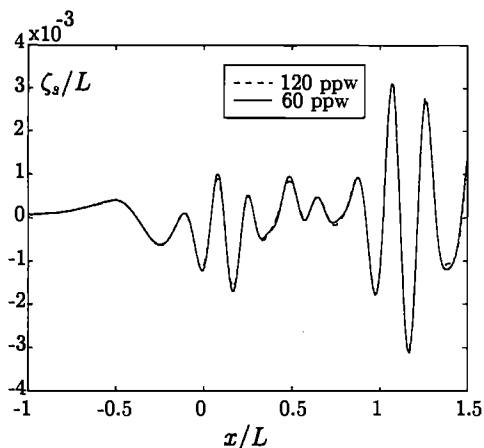


Figure 5.4: Steady wave pattern on the strip of collocation points at $\frac{\Delta y}{L} \approx 0.224$.

Figure 5.3 shows the wave pattern on the strip of collocation points closest to the ship, which lies at a distance of approximately $\Delta y \approx 0.011L$ from the ship or the x -axis. As can be seen there is hardly any difference between the two wave patterns. Only the wave crest at $x = -\frac{1}{2}L$, the wave trough at $x = 0.6L$ and the wave slope starting at $x = 0.25L$ differ a bit.

Figure 5.4 shows the wave pattern on the eighth strip of collocation points, which lies at a distance of about $\Delta y \approx 0.224L$ from the ship or the x -axis. More differences between the two predictions are found here, especially near the peaks but, again, these differences are not large. It turns out that they are mainly caused by differences between the vertical velocities. We may conclude that the wave pattern (and therefore also the steady velocities) converges well when the grid size is reduced.

The free-surface velocities and the velocities on two adjacent planes at distances Δz and $2\Delta z$ from the free surface are used to determine the vertical derivative in the function S (2.7). To investigate whether this derivative converges, we calculate this expression for two values of Δz , namely $\Delta z = 0.00051L$ and $\Delta z = 0.00102L$. In chapter 2 we showed that the vertical derivative can be calculated accurately if $(k\Delta z)^2 \ll 1$. The mentioned vertical distances easily fulfill this condition. Figure 5.5 shows the value of S on the strip of collocation points that lies closest to the ship. As can be seen there is no visible difference between the two predictions. The relative difference between the two curves is even less than one percent.

The transfer term also contains a vertical derivative. Therefore, we also calculated the transfer term with the same two values of Δz . Figure 5.6 shows the result for the eighth strip of collocation points. Unlike the two predictions for the function S , the two predicted transfer terms differ a little, because the vertical derivative is taken from the derivatives of velocities, which introduces some extra inaccuracies. Fortunately, the differences are very

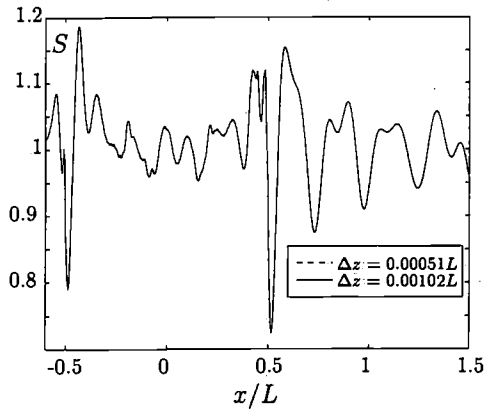


Figure 5.5: The function S on the strip of collocation points closest to the ship for two values of Δz , and 60 panels per wavelength.

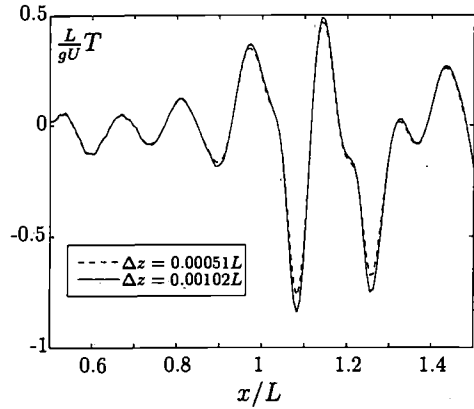


Figure 5.6: The transfer term on the strip of collocation points at $\frac{\Delta y}{L} \approx 0.224$ for two values of Δz , and 60 panels per wavelength.

small again, so we may conclude that the vertical derivatives converge when the vertical distance is decreased, and that the vertical distances we used are small enough.

Now that we know that the vertical derivatives give no problems, we can look what happens to the velocity derivatives if we increase the number of panels in longitudinal direction from 60 per wavelength to 120 per wavelength. Most likely this will influence the tangential derivatives of the squared velocity, the transfer term and the function S .

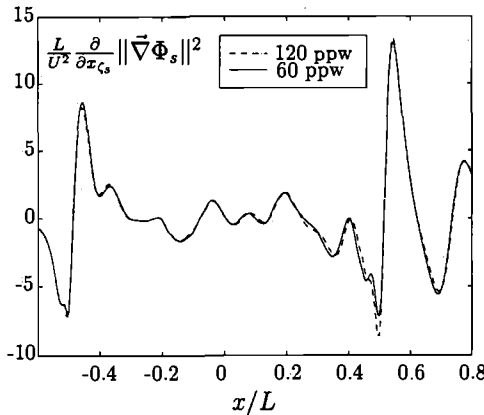


Figure 5.7: Tangential derivative in the x -direction of the squared velocity for 60 and 120 panels per wavelength on the strip of collocation points closest to the ship.

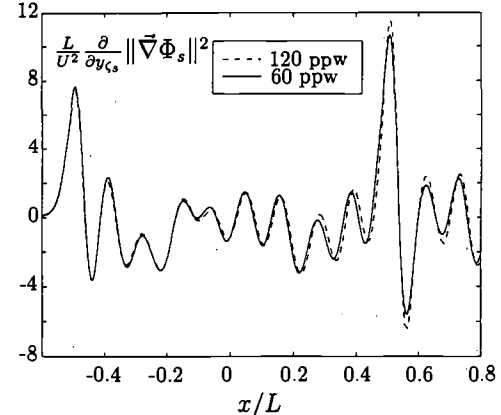


Figure 5.8: Tangential derivative in the y -direction of the squared velocity for 60 and 120 panels per wavelength on the strip of collocation points closest to the ship.

Figure 5.7 shows the tangential derivative of the squared velocity, in the x -direction, on the strip of collocation points that lies closest to the ship. When the number of panels per wavelength is doubled from 60 to 120, no differences between the two predictions can be seen, except at the stern. The y -derivative in figure 5.8 behaves similarly. Therefore, we may conclude that there are no problems with the convergence of the tangential derivatives of the squared velocity and that they may be included in the unsteady free-surface condition.

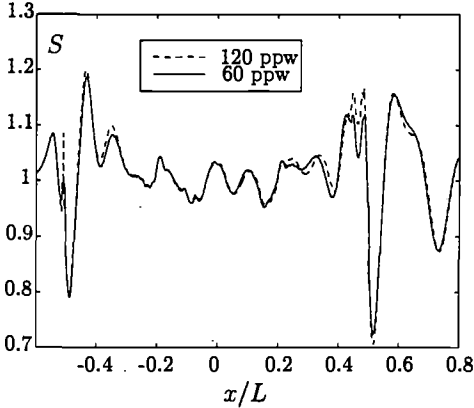


Figure 5.9: The function S on the strip of collocation points closest to the ship for 60 and 120 panels per wavelength, $\Delta z = 0.00102L$.

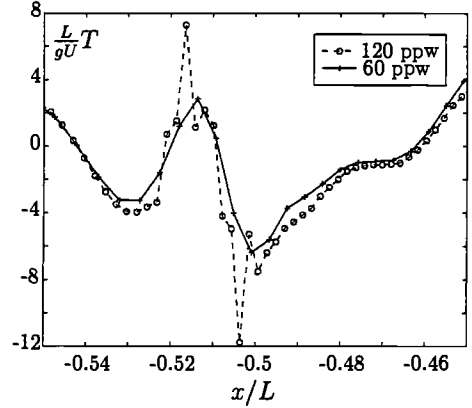


Figure 5.10: Transfer term on the strip of collocation points closest to the ship and near the bow for 60 and 120 panels per wavelength, $\Delta z = 0.00102L$.

What remains to be done is to check the convergence of the transfer term and the function S . Therefore, these were also calculated with 60 and 120 panels per wavelength, while Δz was kept constant. Figure 5.9 shows the function S near the ship. Near the bow, a large peak can be seen when 120 panels per wavelength are used, which indicates strong divergence in a single point. At the stern some differences between the two predictions occur as well, but these are smaller, and the order of the approximation seems correct. If we use the fine grid, then some smoothing algorithm has to be applied to eliminate the peaks at the bow.

Figure 5.10 shows the transfer term at the bow. Just like in figure 5.9 some peaks can be seen in several separate points, which indicates local divergence. The overall picture looks quite good, however, showing only minor differences between the two predictions. Figure 5.11 shows the transfer term between the bow and the stern. Just behind the bow and in front of the stern there are some rather large differences between the two predictions, but at least the curves are smooth, without any strange peaks like near the bow. Finally, figure 5.12 shows the transfer term at the stern. The same holds as for the transfer term at the bow, although the divergence is less bad.

In most collocation points, the transfer term converges, and can be calculated. In collo-

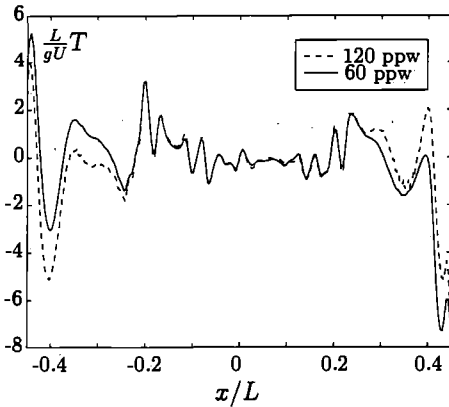


Figure 5.11: Transfer term on the strip of collocation points closest to the ship between bow and stern for 60 and 120 panels per wavelength, $\Delta z = 0.00102L$.

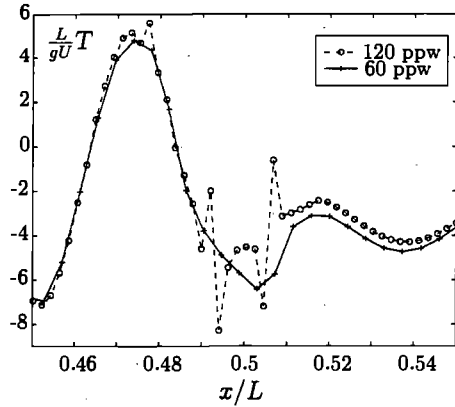


Figure 5.12: Transfer term on the strip of collocation points closest to the ship and near the stern for 60 and 120 panels per wavelength, $\Delta z = 0.00102L$.

cation points where it diverges, like near the bow, it must be extrapolated with values of the transfer term close by that do convergence. When a reasonable accurate value has been obtained, the steady wave, the steady velocities and the derivatives can be used to predict the motions and the resistance of the LNG carrier in waves.

5.3 Added mass, damping and ship motions

The added resistance can only be calculated if the motion of the ship is known. To determine the motion of the ship, we must solve the equation of motion (1.22). Therefore, the first thing to do is to determine all the coefficients in the equation of motion. The mass of the ship and the moments of inertia are known and listed in table 5.1, except the value of k_{zz} , which can be estimated if we assume that the mass of the ship is uniformly distributed over its hull. The restoring-force coefficients are estimated from the steady flow around the ship, and formulas with which they can be determined are listed in appendix A. The added mass and damping are obtained with a time-domain simulation.

The added mass and damping depend on the frequency of the motion. Therefore, a simulation must be run for each required frequency and for each of the six motions. At the start of the simulation, no unsteady waves exist, and to obtain a smooth continuation of this, we have to make sure that the forced motion of the ship starts smoothly. Because the highest time derivative in the free surface condition is a second derivative, we demand that the potential, its first and its second derivative are zero at the start of the simulation. This can be achieved by forcing the motions of the ship to be

$$X_i = A (1 - e^{-ct})^3 \sin \omega t \quad i = 1, 2, 3$$

c is chosen such that after one period, $T = \frac{2\pi}{\omega}$, the amplitude of the motion is 99 percent of its maximal value, A . Of course a similar formula holds for the rotational motion. At the start of the simulation, waves at a wide and continuous range of frequencies are generated. After several periods of forced oscillation, the motion is harmonic with frequency ω , and after some more periods, all non-harmonic waves have been absorbed by the damping zone, and the forces and moments on the ship are harmonic as well. The time this takes depends on the length of the generated waves; in all the cases we study, four periods of oscillation suffice. During the fifth period, the forces and moments are calculated, and after the simulation they are fitted to the motion of the ship. The part of the force that is in phase with the motion gives the added mass, and the part of the force that is out of phase gives the damping, see section 1.6. Because the LNG carrier is symmetric about its center plane, there is no coupling between the even motions surge, heave and pitch, and the odd motions sway, roll and yaw, so a_{ij} and b_{ij} are zero if i plus j is odd. In all simulations, 50 time steps per period were taken, which means that $\Delta t = \frac{2\pi}{50\omega}$. We simulate head waves, bow-quartering waves and beam waves with a length ranging from $\lambda = 0.37L$ to $\lambda = 1.4L$. This means that at Froude number 0.14, the lowest encounter frequency is $\omega = 0.40s^{-1}$ (long beam wave), and the highest encounter frequency is $\omega = 1.23s^{-1}$ (short head wave). This corresponds with values of τ ranging from 0.30 to 0.91. Similarly, at Froude number 0.17, τ ranges from 0.36 to 1.19, and at Froude number 0.2 it ranges from 0.42 to 1.50. It is well known that when the Kelvin condition (1.13) is used, problems occur near $\tau = 0.25$, because then, the dispersion relation has two equal roots and the solution may become unbounded. Of course our free surface condition is different from the Kelvin condition because we use the non-linear steady flow instead of the uniform flow. Still, on parts of the free surface where the non-linear flow is uniform or nearly uniform (outside the bow wave, see figure 5.2), a singularity may appear in a radiated or diffracted wave when τ approaches 0.25, resulting in an unreliable prediction. Therefore, we have to be careful when we interpret our results at the low frequencies, especially when the Froude number is low as well.

Figures 5.13 and 5.14 show several added-mass and damping coefficients. Unfortunately, we have no measurements to compare with, so it is not possible to say whether they are the right values. That will become clear when we use these values to compute the motions. Probably, the oscillations for the low frequencies are due to reflections because the long waves have not been absorbed properly.

When all the coefficients in the equation of motion have been determined, we can simulate the behaviour of the LNG carrier in incoming waves. To simulate the incoming waves, we use the separation method that we described in chapter 4. The incoming-wave potential we use is given by equation (2.13). If the steady flow is uniform, the corresponding, undisturbed, incoming-wave elevation is

$$\zeta_{inc} = \zeta_a \cos(\omega t - kx \cos \theta - ky \sin \theta)$$

We compare the motions of the ship with the incoming-wave elevation in the centre of

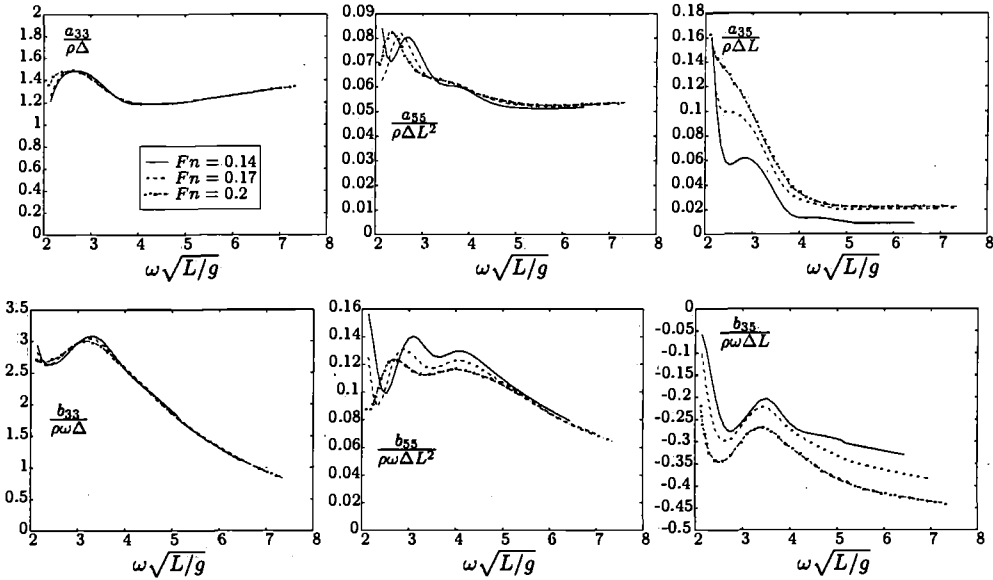


Figure 5.13: Added mass and damping a_{33} , a_{55} , a_{35} , b_{33} , b_{55} and b_{35} .

gravity of the ship, so we write

$$X_i = |X_i| \cos(\omega t - kx_g \cos \theta + \delta_i), \quad \Omega_i = |\Omega_i| \cos(\omega t - kx_g \cos \theta + \gamma_i) \quad i = 1, 2, 3$$

δ_i and γ_i are the differences in phase between the incoming wave in the centre of gravity, and the motion of the ship.

We simulate head waves, bow-quartering waves and beam waves with a length ranging from $\lambda = 0.37L$ to $\lambda = 1.4L$. At each Froude number, the same free-surface grid and hull grid are used for all the wavelengths. As can be seen in the figures in section 2 of this chapter, a large number of panels is needed to accurately represent the steady wave and the velocity derivatives, especially the transfer term. If the Froude number is 0.14, the principal wavelength is $\lambda = 2\pi F_n^2 L \approx 0.12L$. If the Froude number is 0.2, the principal wavelength is about $0.25L$. Of course, also some shorter waves exist, as can clearly be seen in figure 5.3, for example. This means that the steady wave is shorter than the unsteady waves that we try to predict. A free-surface grid that represents the steady wave accurately should also be able to represent these longer unsteady waves. However, to avoid reflections, the computational free surface should have a certain size. This size depends on the length of the unsteady waves. The longer the waves, the larger the size of the free surface and the damping zone should be. Because the grid size has to be small to represent the steady wave, it is not possible to use a very large free surface and very wide damping zone. Had the available computer memory not limited the number of panels to about 3500, the total number of panels could have been increased considerably. Therefore, we truncate the free surface at $x = L$, $x = -L$, and $y = 0.75L$ and use this free-surface

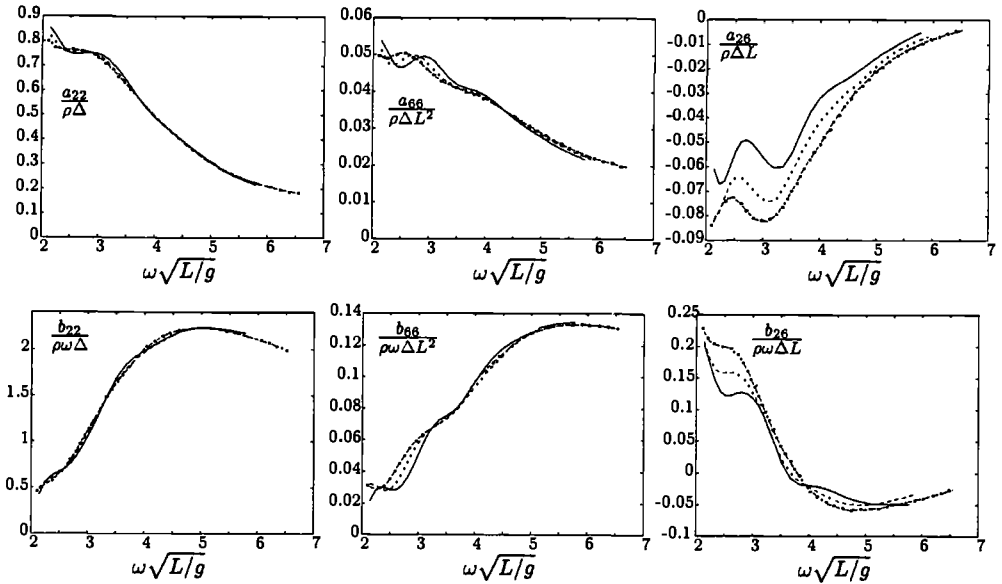


Figure 5.14: Added mass and damping a_{22} , a_{66} , a_{26} , b_{22} , b_{66} and b_{26} .

size in all the computations, although actually we need a larger grid to represent the long waves.

To solve the radiation problem, we smoothed the forced motions of the ship at the start of the simulation; the same smoothing method is applied to the incoming waves as well. After several periods of oscillation, the forces and moments on the ship are harmonic, and from the amplitude and the phase of the forces and moments, we can determine the amplitude and the phase of the harmonic motion of the ship.

Due to the symmetry of the ship, only three motions are possible in head waves: surge, heave and pitch. Figure 5.15 shows our predicted amplitudes and phase differences, and the measured values of these amplitudes and phase differences obtained at the MARIN. The amplitude of the surge motion is predicted reasonably well. For short waves the prediction is very good. When the wavelength increases, there is a point where the amplitude is almost zero. In that point, a jump in the phase of the surge motion occurs which is very hard to predict. For long waves, the surge amplitude is largest and some small differences between our predictions and the measurements can be seen.

The amplitude of the heave motion in short waves is predicted very accurately. Again, in long waves, small deviations occur. The phase difference is also predicted accurately. There is no phase difference between the wave and the heave motion in long waves, which means that the ship follows the motions of the waves. Of course in short waves this is no longer the case.

The prediction of the amplitude of the pitch motion in short waves is very good. Again,

there are some deviations in long waves. In long waves, the pitch motion is 90 degrees out of phase with the incoming wave, so it is in phase with the wave slope.

The small deviations of the motions in long waves have several causes. First, like we indicated before, the computational free surface is too small to represent long waves accurately. Second, we get very close to the value $\tau = 0.25$, especially for the lowest Froude number $Fn = 0.14$. Third, for low frequencies, the restoring-force coefficients have a large influence on the motions of the ship. To determine these coefficients, we have to differentiate the steady velocity on the hull of the ship. Especially at the bow and the stern of the ship, this can be difficult due to the high curvature of the hull and the presence of stagnation points. Therefore, the restoring-force coefficients may be inaccurate. The derivatives of the steady velocities are also required to determine the added mass and damping, so these may also be inaccurate for the low frequencies.

In bow-quartering waves, the lateral forces and moments are also non-zero, so besides the even motions surge, heave and pitch, also the odd motions sway, roll and yaw have to be determined. Figure 5.16 shows our predictions for the even motions and experimental data obtained at the MARIN. The results are quite similar to those in head waves, but of course they differ because the longitudinal wave number, $k \cos \theta$, is different (and therefore the waves also have another encounter frequency), and because the transverse wave number, $k \sin \theta$, is different. The encounter frequency of a bow-quartering wave is lower than that of a head wave with the same length. Therefore the diffracted and radiated waves are longer when the ship sails in bow-quartering waves than when it sails in head waves of the same length. This explains why the deviations between the predicted and measured motions in bow-quartering waves occur already at a smaller wavelength than the deviations in head waves. The reasons for the deviations in long waves have already been discussed.

Figure 5.17 shows the odd motions in bow-quartering waves. The sway motion and the yaw motion in waves with small and medium length are predicted very accurately. In long waves however, our predicted amplitudes just follow a straight line, whereas the measured amplitudes show some fluctuation. This has several reasons. First, in our model, the LNG carrier has no rudder, whereas the prototype used in the measurements has. In long waves, this has a significant influence on the lateral forces and moments on the ship. Second, there is a coupling with the roll motion, especially for sway. As can be seen in figure 5.17, our prediction for the roll motion is very bad, and due to its coupling with sway, it will influence this motion as well. Third, we have the familiar problem of long waves on a too small computational free surface.

Our prediction of the roll motion is very bad because we have no viscosity in our model. It is well known that, to obtain a reasonable accurate prediction of the roll motion with potential flow, one must add viscous roll damping to the ordinary damping that follows from pressure integration. Empirical formulas exist for this roll damping, but it is not obvious that these can be applied to a bulbous tanker sailing at moderate speed. Therefore, viscous damping is not included in our model, and our model is not able to predict the roll motion accurately. This has no serious consequences, since the effect of the roll motion on the added resistance in oblique waves is not very large, unless the amplitude

of the roll motion is very large.

Finally, figure 5.18 shows the sway and heave motion in beam waves. The roll motion is not shown because our model cannot predict it accurately. The other motions are very small in beam waves, hardly influence the added resistance, and are therefore not shown either. The predictions for the sway and the heave motion are reasonably accurate. The deviations from the measurements in beam waves are larger than in head waves and bow-quartering waves. This is due to the fact that the encounter frequency is very low for all wavelengths. The results hardly depend on the Froude number because the encounter frequency of a beam wave is independent of the forward speed of the ship.

We can conclude that our model is able to predict the motions of the LNG carrier very accurately at moderate and high encounter frequencies. Only the roll motion cannot be predicted accurately because there is no viscosity in our model. For low encounter frequencies, so in long head waves, in long bow-quartering waves and in beam waves, differences between our predictions and the measurements can be observed. This is mainly due to a computational free surface that is too small to fit and absorb the long waves. Also, the absence of the rudder of the ship in our model and the coupling of sway with the roll motion have some influence on the predictions. With these predicted motions we will try to obtain a prediction of the added resistance.

5.4 Added resistance

The added resistance of the LNG carrier can be obtained from a final simulation in which we include both the incoming wave and the motions of the ship. Again, we have to wait several periods before the wave elevation and the ship's motions are harmonic. During the final period, the second-order forces and moments are determined and afterwards, they are averaged to obtain the added resistance of the ship, amongst others.

Before we compare our predicted added resistance with the measured values, we have to stress the fact that it is rather difficult to obtain these measured values. At the MARIN, the forces on the ship are measured by mooring a prototype of the ship with a number of soft linear springs. From the displacement of the springs, the forces on the ship can be determined. By averaging the longitudinal force and subtracting the wave resistance, one can find the added resistance. The difficulty is that the springs may not interact with the motions of the ship because the drift forces depend upon these motions. Therefore, the spring constants of the mooring system are chosen such that the natural period of the mooring system is well below the encounter frequency of the incoming wave, which is of course also the frequency of the motions of the ship. A disadvantage of this method is that it is difficult to control the heading of the ship once the vessel responds to the waves and the current. Therefore, the surge motion is often repressed during the measurements. A more extensive description of measuring drift forces can be found in Huijsmans [17].

This indicates how difficult it is to measure the drift forces, and that the measured values may be influenced by the method of measurement. Therefore, we may never assume

that the measured values are the exact values and must always keep a critical eye on the method of measurement.

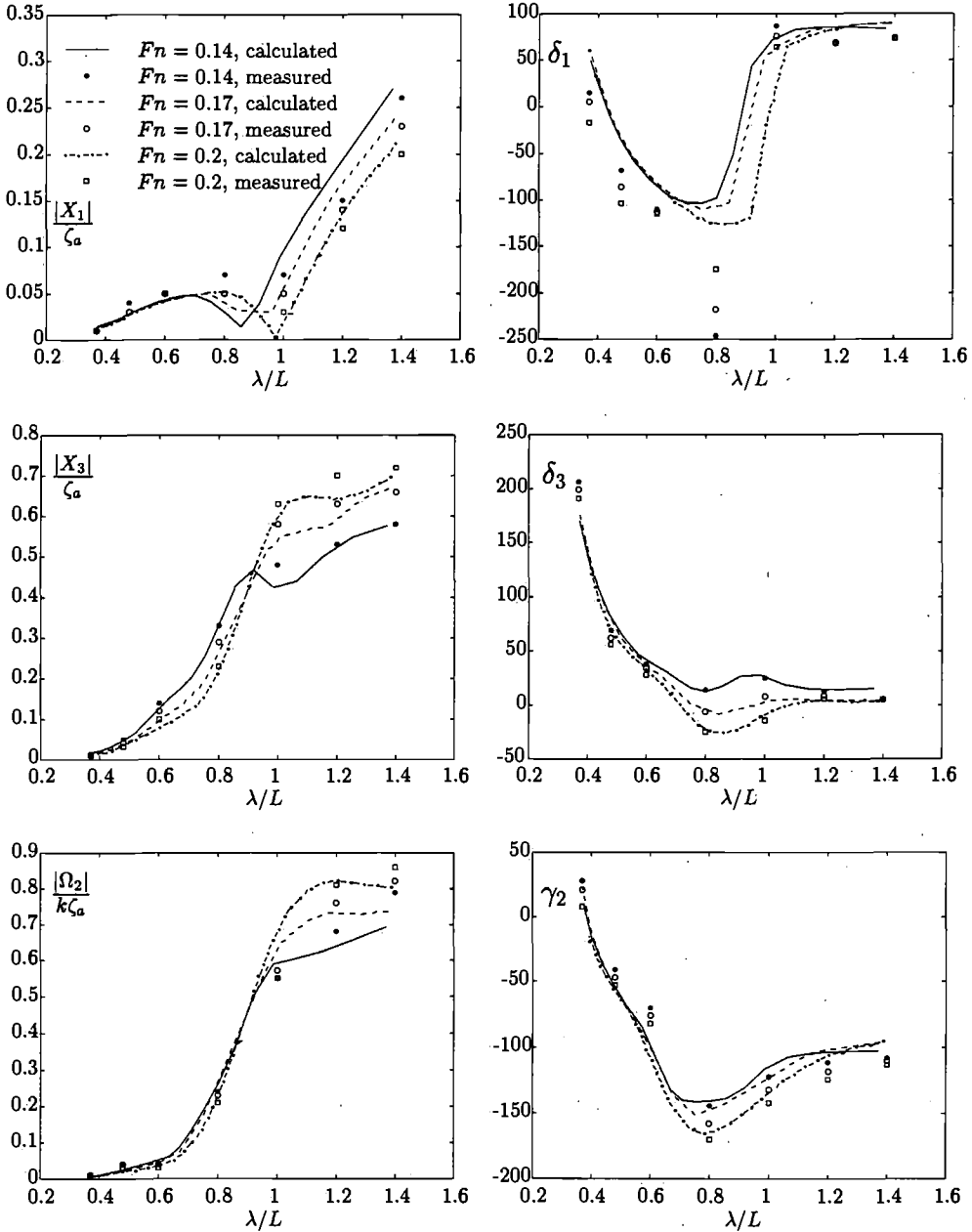


Figure 5.15: Surge, heave and pitch motion in head waves.

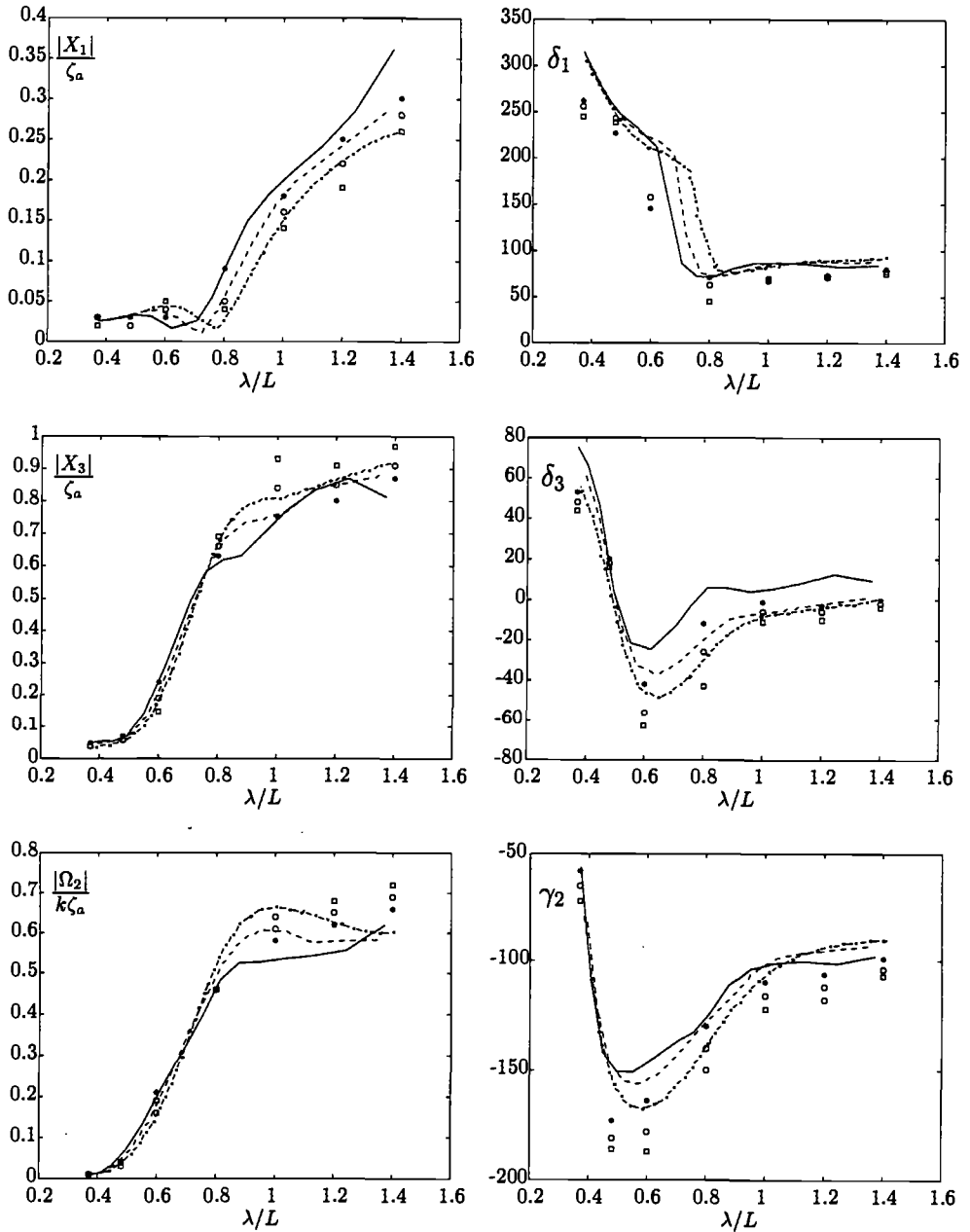


Figure 5.16: Surge, heave and pitch motion in bow-quartering waves. Legend as in figure 5.15.

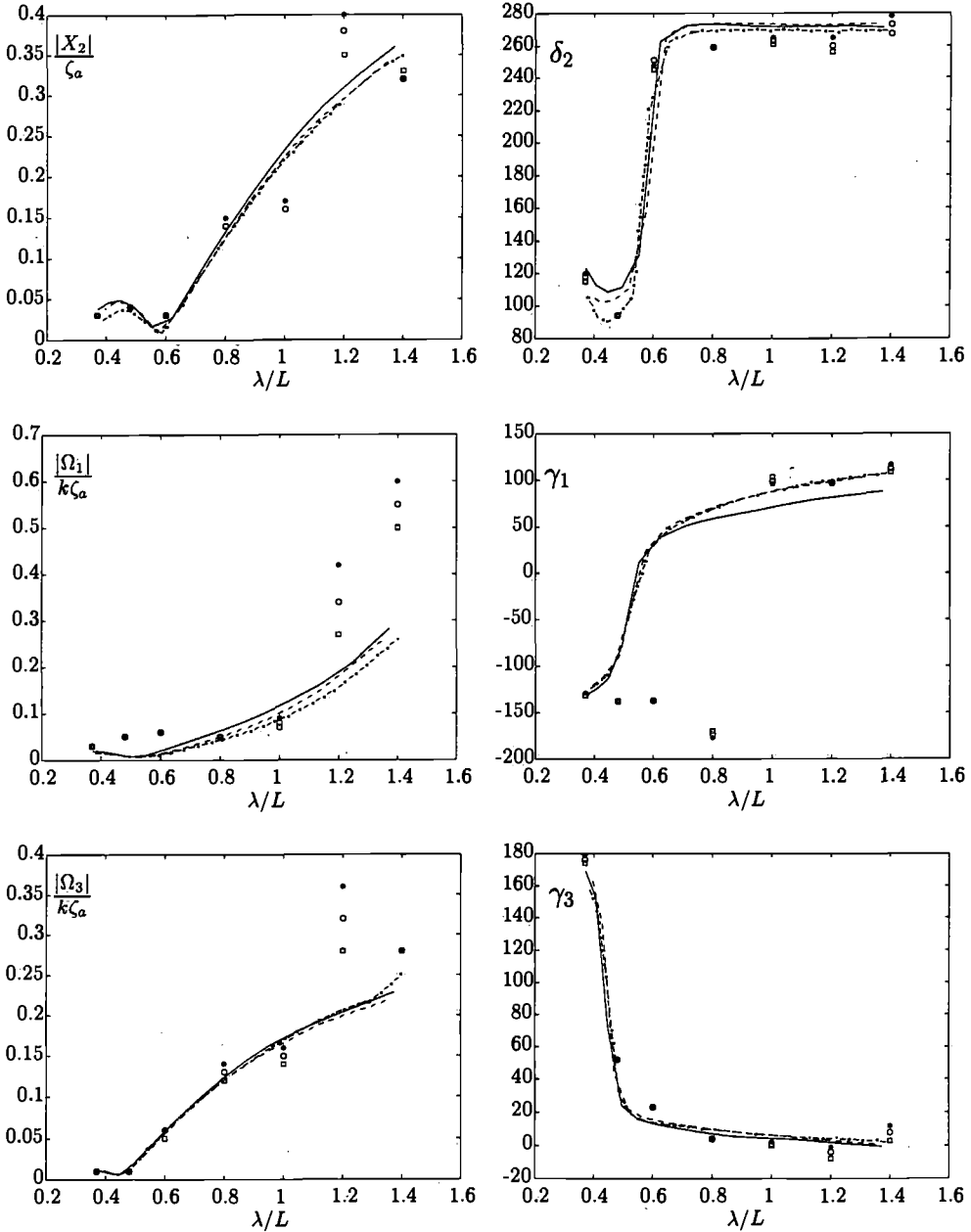


Figure 5.17: Sway, roll and yaw motion in bow-quartering waves. Legend as in figure 5.15.

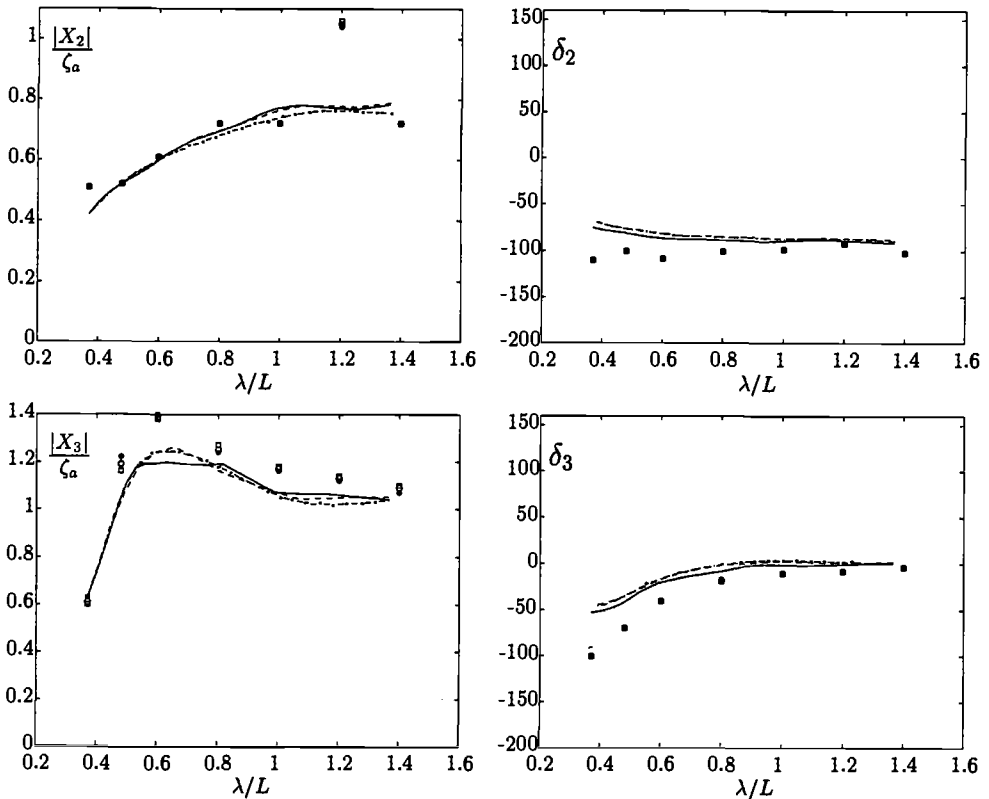


Figure 5.18: Sway and heave motion in beam waves. Legend as in figure 5.15.

Figure 5.19 shows our prediction of the added resistance in head waves, and measurements from the MARIN. Especially at the highest Froude number, $Fn = 0.2$, hardly any differences can be seen between our prediction and the measurements. Only the maximal value seems to be slightly underestimated. For the two lower Froude numbers, there is some deviation in long waves. In that case, our method gives lower values than the measurements. Remarkably, our method gives a good prediction for short waves as well. Most linear methods are not capable of doing this and greatly underestimate the added resistance in short waves. Therefore, our predictions in head waves are very good.

Figure 5.20 shows our prediction of the added resistance in bow-quartering waves. Unfortunately, the differences between our prediction and the measurements are larger than in head waves. For long waves our model underpredicts the added resistance. For short waves, the added resistance seems to increase again, which is not predicted by our model. Only for waves with medium length the results are accurate.

There are several reasons for the deviations in long waves. First, there is the familiar problem of a long wave on a too small free surface. This not only influences the predicted motions, as we saw in the previous section, but also the predicted wave elevation. Since

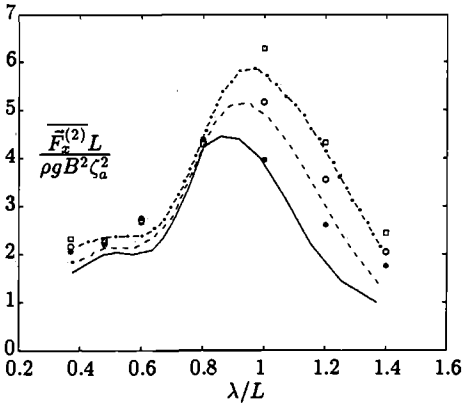


Figure 5.19: Added resistance in head waves, legend as in figure 5.15.

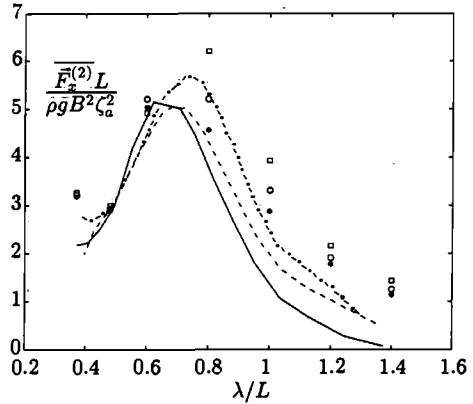


Figure 5.20: Added resistance in bow-quartering waves, legend as in figure 5.15.

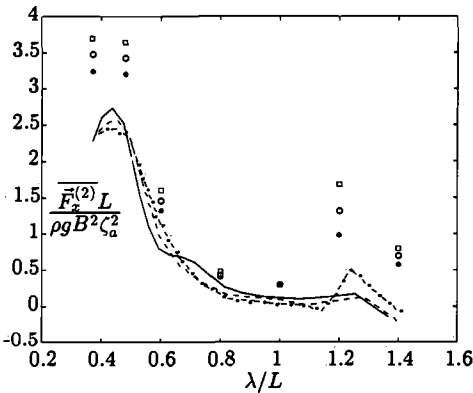


Figure 5.21: Added resistance in beam waves, legend as in figure 5.15.

both the motions of the ship and the wave elevation on the steady waterline are needed to determine the added resistance, an error enters the predicted added resistance twice. Second, the derivative of the first-order pressure in the direction of the motion is needed to calculate the added resistance, as can be seen in equation (1.26). We are not sure that this derivative can be calculated accurately. If it is not accurate, then the inaccuracies in the added resistance are large if the amplitude of the motion is large, so for long waves. The prediction for short waves will not be influenced by errors in the pressure derivative. Finally, we showed that

the roll motion and the yaw and sway motion in long bow-quartering waves cannot be determined accurately. This also has some influence on the added resistance. The deviations in short waves probably occur due to the fact that the longitudinal wavelength, $\lambda \cos \theta$ (which is the length of the projection of the wave on the x -axis) is smaller for a bow-quartering wave than for a head wave with the same length, and it is therefore harder to represent the bow-quartering wave accurately than the head wave when the same free-surface grid is used.

Figure 5.21 shows the added resistance in beam waves. The added resistance is for the larger part determined by the difference in wave height between the bow and the stern, and this difference is very small in beam waves, so the added resistance is small as well. Only for short waves, the encounter frequency is such that the diffracted and radiated waves that propagate along the waterline are short enough to cause a resistance increase.

Although our model underestimates it, it does predict this increase in added resistance. In long waves, there is a small increase in the added resistance because the roll motion is very large, which we did not show. Our model does not predict this large roll motion, and therefore neither the slight increase in the added resistance.

5.5 Comparison with other linearizations

After having obtained good results with a quite complicated method, you can always wonder whether similar results can be obtained with simpler methods that already exist. Therefore, we repeat some of our calculations with other approximations of the steady flow: the uniform flow and the double-body flow. These were described in chapter 1. Sierevogel [31] also used the double-body flow to predict the motions and the added resistance of the LNG carrier, and she got very poor results. Because our numerical model and our mathematical model are very different from hers, it is not sure that in our case the use of the double-body flow gives poor results as well.

We substitute these steady flows into our free-surface condition (1.12). If the flow is uniform, this leads to the Kelvin condition on the calm-water plane, $z = 0$ (1.13). If we use the double-body flow, this leads to a condition with similar terms as in condition (1.12), except for the transfer term, which is zero because the normal velocity on the free surface is zero. Furthermore, this condition is defined on the calm water plane instead of on the actual steady free surface. Although this linearization about the double-body flow is not consistent (for a derivation of the actual free-surface condition if the double-body flow is used see Prins [28]), it will give enough insight to make some statements on the use of the double-body flow.

Not only the free-surface condition is affected when other base flows are used, also the body boundary condition and the equation of motion change. When we use uniform flow, the derivatives of the steady flow along the hull are zero, which simplifies the body boundary condition to

$$\frac{\partial \phi}{\partial n} = \frac{\partial \bar{\alpha}}{\partial t} \cdot \bar{n} + U \frac{\partial \bar{\alpha}}{\partial x} \cdot \bar{n}$$

The body boundary condition is not affected if the double-body flow is used, so the velocity derivatives on the hull still have to be determined. Because the restoring-force coefficients are obtained from the steady flow field (see appendix A), they also depend on the kind of linearization that is used. So, even if the same first-order force is predicted by all three methods, this can still lead to differing predictions of the motions.

Figure 5.22 shows the predictions for the steady wave elevation on the strip of collocation points that lies closest to the ship, for Froude number 0.2. Of course the predicted wave elevation is zero if uniform flow is used. When double-body flow is used, no waves are generated behind the ship, and the amplitudes of the bow wave and the stern wave are greatly underestimated, compared to the non-linear and far more realistic case. Still, the approximation is much better than in the uniform-flow case. An incoming wave reacts

very differently when it propagates over the non-linear steady wave field and when it propagates over the uniform-flow field. The double-body case will probably be somewhere in between.

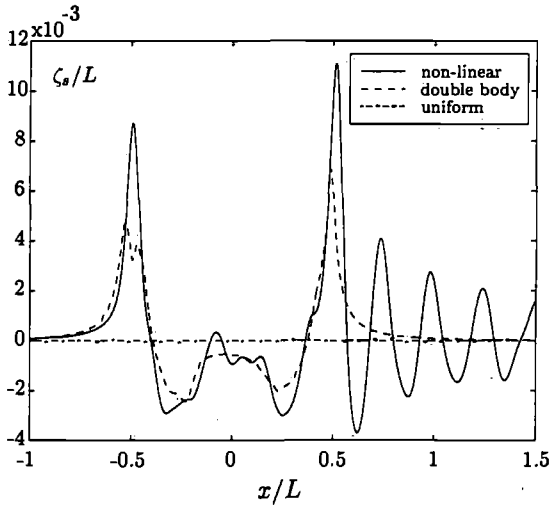


Figure 5.22: Steady wave on strip of collocation points closest to the ship.

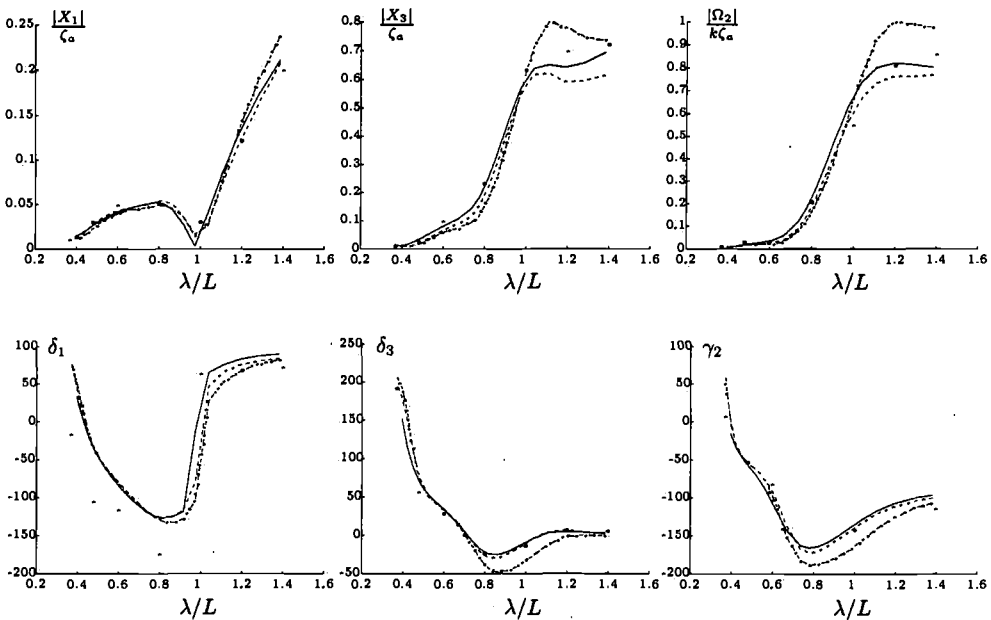


Figure 5.23: Amplitudes and phase shifts of surge, heave and pitch motion in head waves and for $Fn = 0.2$. Legend as in figure 5.22. The asterisks correspond to measurements.

We compare the ship's motions and the added resistance in head waves when the ship sails at Froude number 0.2. As shown in the previous section, our results were very good in that case. Figure 5.23 shows the surge, heave and pitch motion if we use the non-linear flow, the double-body flow and the uniform flow. In most cases, no large differences between the three predictions can be seen. The differing predictions of the restoring-force coefficients only influence the low-frequency motions. Therefore, there are some differences between the three heave amplitudes, and between the three pitch amplitudes in long waves. It seems that all three linearizations can predict the motion of the LNG carrier in short waves quite accurately. However, the prediction that uses the non-linear steady flow is the best.

Figure 5.24 shows the added resistance computed with the non-linear flow, the double-body flow and the uniform flow. Although the predicted motions of the ship were not that much different, we see large differences between the predicted added resistances. The use of the double-body flow results in a large underestimation of the added resistance, and the use of the uniform flow in a huge underestimation of the added resistance. These underestimations cannot be caused by the small differences between the predicted motions. Therefore, there must be another explanation. Since the differences between the predicted added resistances do not seem to be caused by the first-order fluid quantities on the hull of the ship (otherwise there would have been larger differences between the motions), nor the motions, they must be caused by the predicted wave elevation on the steady waterline of the ship.

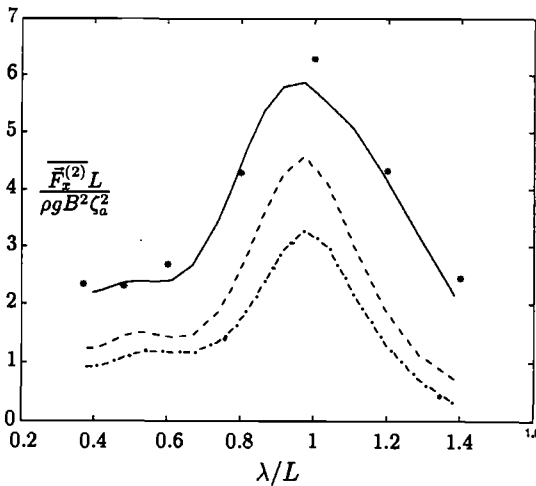


Figure 5.24: Added resistance in head waves and for $Fn = 0.2$. Legend as in figure 5.22. The asterisks correspond to measurements.

To verify this statement, we calculated the amplitude of the diffracted and incoming wave at the bow (coordinates $(x, y) = (-\frac{L}{2}, 0)$) and the amplitude of the diffracted and incoming wave at the stern (coordinates $(x, y) = (\frac{L}{2}, 0)$). The wave elevation at the bow

and the stern largely influence the added resistance. The wave elevation at parts of the waterline that are parallel to the x -axis (so almost the complete waterline except the part near the stern and the bow, see figure 5.2) has no influence on the added resistance since the normal vector on the ship has no component in the x -direction there.

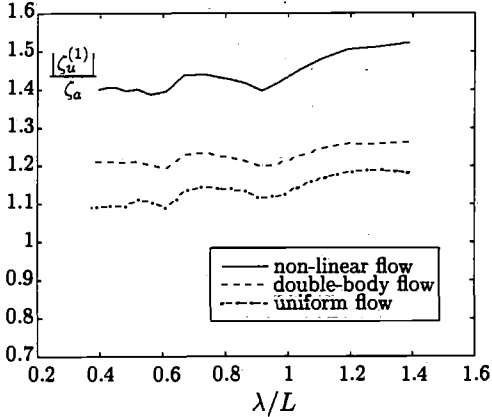


Figure 5.25: Amplitude of incoming and diffracted wave at $(x, y) = (-\frac{1}{2}L, 0)$.

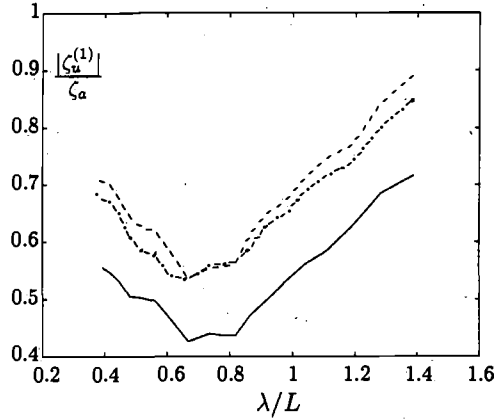


Figure 5.26: Amplitude of incoming and diffracted wave at $(x, y) = (\frac{1}{2}L, 0)$. Legend as in figure 5.25.

Figure 5.25 shows the amplitude of the bow wave when we use the non-linear flow, the double-body flow and the uniform flow. If the non-linear flow is used, then the amplitude of the bow wave is about 40 to 50 percent higher than the amplitude of the incoming wave. The double-body flow results in an increase of about 20 to 25 percent and uniform flow in an increase of about 10 to 15 percent.

Figure 5.26 shows the amplitude of the stern wave if we use the non-linear flow, the double-body flow and the uniform flow. The use of the double-body flow and the uniform flow results in approximately the same predicted amplitude. The use of the non-linear flow results in a much smaller amplitude.

The large differences between the predicted bow waves and stern waves strongly influence the predicted added resistance. Apparently, our method, which uses the non-linear flow, is the only method that predicts the bow and stern wave accurately. However, Iwashita [18], who extended the frequency-domain method developed by Bertram, which also takes into account the non-linear steady flow, found considerable differences between his predicted wave pattern for the Series 60 model sailing at $Fn = 0.2$ in head waves, and measurements of this wave pattern. Although Iwashita uses the same free-surface condition, his numerical model is very different from ours, so this does not imply that our results for the LNG carrier should be questioned. We may conclude that, to calculate the motion of the LNG carrier in waves with small and medium length, one can use the double-body flow or even the uniform flow. If one wants to calculate the added resistance, however, the non-linear steady flow has to be used because only this method predicts the unsteady

waves correctly.

5.6 Summary and conclusions

We applied our model to an LNG carrier sailing at a moderate speed, corresponding to the Froude numbers $Fn = 0.14$, $Fn = 0.17$ and $Fn = 0.2$. Head waves, bow-quartering waves and beam waves were simulated. The non-linear steady flow was determined by RAPID, and the resulting velocities were differentiated to obtain all the steady quantities that we need in the free-surface condition (1.12). A convergence study was carried out that showed that the transfer term close to the bow and the stern diverged in some collocation points. Extrapolation is necessary here.

With this non-linear flow, we calculated the first-order motions of the ship and the added resistance on the ship, and compared our predictions with measurements from the MARIN. For the motions, we got excellent agreement between our predictions and the measurements. Only the roll motion is wrongly predicted, and there are some deviations when the encounter frequency of the waves is low. The roll motion cannot be predicted correctly because there is no viscosity in our model, and therefore no viscous roll damping. For low frequencies, the waves are too long to fit on the computational free surface, which grid size is determined by the length of the steady waves, which is quite small for the mentioned Froude numbers. Therefore, the size of the computational free surface and damping zone must be kept small to avoid a too large amount of panels. Furthermore, for low frequencies, the restoring-force coefficients influence the motions considerably. To determine these coefficients, the steady velocity on the hull has to be differentiated, which is rather difficult, especially near the stagnation points at the bow and the stern. Also, the absence of the rudder in our model influences the yaw motion in long oblique waves.

The added resistance was predicted very well in head waves, especially at the highest Froude number $Fn = 0.2$. For short waves, most linearized methods underpredict the added resistance, but our model is able to get the prediction right. In bow-quartering waves the results are less accurate, especially for long waves. The same holds for beam waves. Again, there is the problem of a long wave on a too small free surface. Furthermore, the derivative of the first-order pressure in the direction of the motion has to be determined, which can be inaccurate, and has the most influence for long waves.

To obtain better results for long waves, a larger computational free surface is needed with a grid size that is related to the steady wavelength. This results in a large number of panels, which can only be stored on a computer with much memory, like a CRAY. A second-order panel method is needed to get more accurate fluid velocities and to describe the curvature of the hull, so derivatives of velocities can more easily be determined. This has to be implemented both in RAPID and in our code. The main problem that arises is that both RAPID and our code use difference schemes on the free surface to stabilize the methods. When velocity derivatives are obtained directly from the integral equation, another way of damping the waves has to be found.

Discussion and conclusions

In this thesis, a method was presented that predicts the motions of and the forces on a symmetrical ship sailing at moderate to high speed in incoming waves. There is a strong interaction between the steady waves on the one hand and the unsteady waves, the motions of the ship and the forces on the ship on the other hand. For moderate and high speeds of the ship, non-linear phenomena in the steady wave become more and more important, and it is no longer possible to use a model in which the steady flow is approximated by the uniform flow or the double-body flow, like Prins [28] and Siervogel [31] did. Therefore, a linearization was carried out about the non-linear steady flow.

The use of the non-linear steady flow in the linearization leads to a linear free-surface condition in which not only the steady velocities are needed, but also several derivatives of these steady velocities, including a second derivative which we called the transfer term. Because these velocities are determined with a first-order panel method, and are therefore of first-order accuracy, their second derivative may diverge. For the cases that we studied; the test ship and the LNG carrier, it turned out that near the bow and the stern, the transfer term indeed diverges in some collocation points. In those points the transfer term has to be extrapolated from the transfer term in points further away from the ship where it does converge. The transfer term cannot be neglected because it significantly influences the wave elevation, and therefore the added resistance as well.

Because of the accuracy of the steady velocities and its effect on the unsteady velocities, it is useless to use a panel method of second order or higher to determine the time-dependent flow, and therefore, a first-order panel method is used. The velocity potential is represented by pulsating sources on the hull of the ship, and on a surface at a short distance above the free surface. The hull and this raised surface are divided into panels on which the source strength is assumed to be constant. The time derivatives in the linearized free-surface condition are discretized with difference schemes in which a constant time step is used. This leads to a simulation in the time domain which has the advantage that it can be applied to a broad scope of problems. In this thesis, however, only calculations have been carried out which could have been carried out in the frequency domain as well. The tangential space derivatives in the linearized free-surface condition are discretized with upwind difference schemes. In such schemes, only collocation points are used that are upstream of the position at which the derivative is required. In our stability analysis, we showed that for moderate and high speeds, such schemes have to be used to guarantee a stable numerical scheme. Only for low speeds it is safe to use the more accurate central

difference schemes.

In the time domain, incoming waves can be modeled by using wave makers, or by separating the incoming wave and the diffracted wave, and only calculate the latter. Both methods were implemented and gave satisfactory results for the test ship. We prefer the separation method, because it takes less simulation time and requires less panels, and because there is only damping and dispersion in the diffracted wave.

The model was applied to an LNG carrier, sailing at three moderate speeds, corresponding to the Froude numbers $F_n = 0.14$, $F_n = 0.17$ and $F_n = 0.2$. The predicted motions and added resistances were compared with measurements from the MARIN. In head waves, we got excellent agreement between the predictions and the measurements. Only for long waves some deviations were observed. The main problem for long waves is that the grid size is related to the length of the steady waves, whereas the size of the computational free surface and the damping zone is related to the longest waves that must be represented. In case of a long unsteady wave that propagates over a short steady wave, a enormous number of panels is required to have an appropriate grid size and an appropriate size of the free surface. Unfortunately, the computers we did our calculations on had not enough memory to store this amount of panels. Therefore, for the long waves, we had to use a very unsatisfactory grid size and free-surface size.

In oblique waves, the encounter frequency of the waves is even lower than that of a head wave with the same length. Therefore, in oblique waves, the grid problems were even more evident than in head waves. For short waves however, the predictions are again very good. Only the roll motion cannot be predicted by our method because we have no viscous roll damping.

For the highest Froude number, we repeated the calculations for head waves with two simpler models. Instead of the non-linear flow, we first used the uniform flow and then the double-body flow to model the steady flow around the ship. It turns out that with these simplified models it is possible to determine the motions of the LNG carrier, but that they both give a large underprediction for the added resistance. This is due to the predicted amplitude of the unsteady waves at the waterline of the ship. Only if the non-linear steady flow is used, the waves are predicted correctly.

For future research, the following recommendations are made:

- The computer code must be implemented on a faster computer with more memory. This gives the opportunity to model long waves as well.
- A higher-order panel method must be used, both in RAPID and in our own code, to determine derivatives of velocities more accurately.
- A frequency-domain version of the code must be written to solve the harmonic solutions more efficiently.
- The code must be validated with some more ships, and extended to be able to simulate, for example, ships with transom sterns, and catamarans.

Appendix A

Restoring-force coefficients

In this appendix, formulas are derived for the restoring-force coefficients. These coefficients relate the restoring forces to the motion of the ship. They differ from the ones listed by Prins [28] because we make no low-speed approximation.

The first-order forces and moments have been derived in chapter 1. They consist of a hydrodynamic part that depends on the first-order potential, and a restoring part that depends directly on the motion of the ship. The restoring part is given by

$$\vec{F}_r^{(1)} = \iint_{\bar{H}} \left(p_s \vec{\Omega}^{(1)} \times \vec{n} + \left(\vec{X}^{(1)} + \vec{\Omega}^{(1)} \times (\vec{x}_s - \vec{x}_g) \right) \cdot \vec{\nabla} p_s \vec{n} \right) dS$$

$$\vec{M}_r^{(1)} = \iint_{\bar{H}} \left(\vec{X}^{(1)} + \vec{\Omega}^{(1)} \times (\vec{x}_s - \vec{x}_g) \right) \cdot \vec{\nabla} p_s (\vec{x}_s - \vec{x}_g) \times \vec{n} dS$$

The restoring-force matrix C , containing the restoring-force coefficients $C_{i,j}$, with $i, j = 1 \dots 6$, follows from

$$\begin{pmatrix} \vec{F}_r^{(1)} \\ \vec{M}_r^{(1)} \end{pmatrix} = -C\vec{Y}$$

By letting all entries of the motion vector \vec{Y} , but one, be zero, the coefficients can be found. If we do this we find coefficients $C_{i,1}$ and $C_{i,2}$ which are non-zero. These coefficients correspond to the restoring forces and moments caused by a small deviation of the ship's mean position in surge and sway direction. In a realistic fluid the steady flow field around the vessel adapts to the new position of the ship immediately, leading to zero surge and sway restoring forces and moments. Due to the linearization around the mean position of the ship, this fact is not accounted for by our model, so we have to set these coefficients zero ourselves. The remaining non-zero coefficients are

$$C_{1,3} = - \iint_{\bar{H}} \frac{\partial p_s}{\partial z} \bar{n}_x dS$$

$$C_{3,3} = - \iint_{\bar{H}} \frac{\partial p_s}{\partial z} \bar{n}_z dS$$

$$C_{5,3} = - \iint_{\bar{H}} \frac{\partial p_s}{\partial z} (-x\bar{n}_z + z\bar{n}_x) dS$$

$$C_{2,4} = - \iint_{\bar{H}} \left(-p_s \bar{n}_z + \left(-z \frac{\partial p_s}{\partial y} + y \frac{\partial p_s}{\partial z} \right) \bar{n}_y \right) dS$$

$$C_{4,4} = - \iint_{\bar{H}} \left(-z \frac{\partial p_s}{\partial y} + y \frac{\partial p_s}{\partial z} \right) (y\bar{n}_z - z\bar{n}_y) dS$$

$$C_{6,4} = - \iint_{\bar{H}} \left(-z \frac{\partial p_s}{\partial y} + y \frac{\partial p_s}{\partial z} \right) (x\bar{n}_y - y\bar{n}_x) dS$$

$$C_{1,5} = - \iint_{\bar{H}} \left(p_s \bar{n}_z + \left(z \frac{\partial p_s}{\partial x} - x \frac{\partial p_s}{\partial z} \right) \bar{n}_x \right) dS$$

$$C_{3,5} = - \iint_{\bar{H}} \left(-p_s \bar{n}_x + \left(z \frac{\partial p_s}{\partial x} - x \frac{\partial p_s}{\partial z} \right) \bar{n}_z \right) dS$$

$$C_{5,5} = - \iint_{\bar{H}} \left(z \frac{\partial p_s}{\partial x} - x \frac{\partial p_s}{\partial z} \right) (-x\bar{n}_z + z\bar{n}_x) dS$$

$$C_{2,6} = - \iint_{\bar{H}} \left(p_s \bar{n}_x + \left(-y \frac{\partial p_s}{\partial x} + x \frac{\partial p_s}{\partial y} \right) \bar{n}_y \right) dS$$

$$C_{4,6} = - \iint_{\bar{H}} \left(-y \frac{\partial p_s}{\partial x} + x \frac{\partial p_s}{\partial y} \right) (y\bar{n}_z - z\bar{n}_y) dS$$

$$C_{6,6} = - \iint_{\bar{H}} \left(-y \frac{\partial p_s}{\partial x} + x \frac{\partial p_s}{\partial y} \right) (x\bar{n}_y - y\bar{n}_x) dS$$

Appendix B

Derivation of the discrete dispersion relation

In this appendix the continuous Fourier transform of the Green function and its vertical derivative are derived. They are used to derive the discrete dispersion relation with help of the aliasing and convolution theorem.

B.1 The continuous Fourier transform of the Green function

To obtain the discrete dispersion relation, we need the continuous spatial Fourier transforms of the Green function, G , and its vertical derivative, $\frac{\partial G}{\partial z}$, as we shall see later. The Green function we use is a Rankine source, given by

$$G(\vec{x}, \vec{\xi}) = \frac{-1}{4\pi\sqrt{(x-\xi)^2 + (y-\eta)^2 + (z-\zeta)^2}} \quad (\text{B.1})$$

We will assume from now on, that the field point \vec{x} is on the free surface $z = 0$ and the source point $\vec{\xi}$ is on the raised surface $z = z_{fs}$. The continuous spatial Fourier transform of the Green function is then defined as follows

$$\tilde{G}(\alpha, \beta) = \int_{-\infty}^{\infty} \int_{-\infty}^{\infty} \frac{-e^{i\alpha x + i\beta y} dx dy}{4\pi\sqrt{(x-\xi)^2 + (y-\eta)^2 + z_{fs}^2}} \quad (\text{B.2})$$

In order to determine this integral, we change to polar coordinates according to

$$x - \xi = r \cos \phi \quad y - \eta = r \sin \phi \quad (\text{B.3})$$

The transform (B.2) now becomes

$$\tilde{G}(\alpha, \beta) = e^{i\alpha\xi + i\beta\eta} \int_0^{\infty} \int_0^{2\pi} \frac{-e^{i\alpha r \cos \phi + i\beta r \sin \phi} r dr d\phi}{4\pi\sqrt{r^2 + z_{fs}^2}} \quad (\text{B.4})$$

Using the properties of the sine and cosine functions, it can be shown that this integral can be simplified into

$$\tilde{G} = e^{i\alpha\xi + i\beta\eta} \int_0^\infty \frac{-r dr}{2\pi \sqrt{r^2 + z_{fs}^2}} \int_0^\pi \cos(r \cos(\phi) \sqrt{\alpha^2 + \beta^2}) d\phi \quad (\text{B.5})$$

The integral to ϕ can be evaluated by using the following expression for the zeroth-order Bessel function, see Abramowitz and Stegun [1]

$$J_0(z) = \frac{1}{\pi} \int_0^\pi \cos(z \cos \phi) d\phi \quad (\text{B.6})$$

The remaining integral to r then contains a Bessel function and can be evaluated using the modified Bessel function, see again Abramowitz and Stegun [1]

$$K_{\frac{1}{2}}(az) = e^{-az} \sqrt{\frac{\pi}{2az}} = \sqrt{\frac{a\pi}{2z}} \int_0^\infty \frac{r J_0(ar) dr}{\sqrt{r^2 + z^2}} \quad a > 0 \quad \Re(z) > 0 \quad (\text{B.7})$$

Using this formula, it can be shown that the continuous spatial Fourier transform of G becomes

$$\tilde{G} = -\frac{e^{i\alpha\xi + i\beta\eta - z_{fs} \sqrt{\alpha^2 + \beta^2}}}{2\sqrt{\alpha^2 + \beta^2}} \quad (\text{B.8})$$

The same method can be applied to obtain the continuous spatial Fourier transform of $\frac{\partial G}{\partial z}$, \tilde{Q} . According to the definition, this transform is

$$\tilde{Q}(\alpha, \beta) = \int_{-\infty}^\infty \int_{-\infty}^\infty \frac{-z_{fs} e^{i\alpha x + i\beta y} dx dy}{4\pi ((x - \xi)^2 + (y - \eta)^2 + z_{fs}^2)^{\frac{3}{2}}} \quad (\text{B.9})$$

A change to polar coordinates and integration with respect to the polar angle ϕ leaves us again with an integral containing a Bessel function of order zero. This time we can solve this integral using the modified Bessel function $K_{-\frac{1}{2}}$, see again Abramowitz and Stegun [1]

$$K_{-\frac{1}{2}}(az) = e^{-az} \sqrt{\frac{\pi}{2az}} = \sqrt{\frac{\pi z}{2a}} \int_0^\infty \frac{r J_0(ar) dr}{(r^2 + z^2)^{\frac{3}{2}}} \quad a > 0 \quad \Re(z) > 0 \quad (\text{B.10})$$

It can be shown that the continuous Fourier transform \tilde{Q} becomes

$$\tilde{Q}(\alpha, \beta) = -\frac{e^{i\alpha\xi + i\beta\eta - z_{fs} \sqrt{\alpha^2 + \beta^2}}}{2} = \tilde{G} \sqrt{\alpha^2 + \beta^2} \quad (\text{B.11})$$

B.2 The discrete dispersion relation

The discrete dispersion relation can be found after applying the discrete Fourier transform (3.13) to equations (3.9), (3.10), (3.11) and (3.12). Before we do this, we introduce two theorems that we need in the derivation.

The discrete convolution theorem

Similar to the continuous case, a convolution theorem holds in the discrete case, saying that

$$\text{If } a_m = \sum_{j=-\infty}^{\infty} b_j c_{m-j}, \text{ then } \hat{a}(\alpha) = \frac{1}{\Delta x} \hat{b}(\alpha) \hat{c}(\alpha)$$

Of course this theorem holds for the discrete Fourier transforms in all spatial directions and in time, so

$$\hat{a}(\beta) = \frac{1}{\Delta y} \hat{b}(\beta) \hat{c}(\beta) \quad \text{and} \quad \hat{a}(\omega) = \frac{1}{\Delta t} \hat{b}(\omega) \hat{c}(\omega)$$

The aliasing theorem

If a function is known only in a countable number of discrete points, the discrete Fourier transform may be taken. If we also know the function itself or another function taking on the same values in the discrete points, and the corresponding continuous Fourier transform, the discrete Fourier transform can be found from the knowledge of the continuous transform. This follows from the aliasing theorem which states

$$\hat{f}(\alpha) = \sum_{j=-\infty}^{\infty} \tilde{f}\left(\alpha + \frac{2\pi j}{\Delta x}\right)$$

which can easily be derived from the definitions of the continuous and discrete transforms. Of course this theorem holds for the transforms in all spatial directions and in time.

With these two theorems, the discrete dispersion relation can be derived. First we will determine the spatial discrete Fourier transform of the potential ϕ , induced by the source distribution on the raised surface

$$\phi(x_m, y_n) = \sum_{i=-\infty}^{\infty} \sum_{j=-\infty}^{\infty} \sigma_{i,j} G_{m-i, n-j}$$

This equation is in a double convolution shape, so we can use the convolution theorem twice to obtain the discrete Fourier transform. If we call the discrete transform of the source strength $\hat{\sigma}$ we find

$$\hat{\phi}(\alpha, \beta) = \frac{1}{\Delta x \Delta y} \hat{\sigma} \hat{G} \tag{B.12}$$

\widehat{G} is the discrete transform of the integrated Green function $G_{m,n}$ where

$$G_{m,n} = \int_{-\frac{1}{2}\Delta x}^{\frac{1}{2}\Delta x} \int_{-\frac{1}{2}\Delta y}^{\frac{1}{2}\Delta y} \frac{-dx_0 dy_0}{4\pi \sqrt{(m\Delta x - x_0)^2 + (n\Delta y - y_0)^2 + z_{fs}^2}}$$

so \widehat{G} is defined as

$$\widehat{G} = \Delta x \Delta y \sum_{m=-\infty}^{\infty} \sum_{n=-\infty}^{\infty} e^{i\alpha m \Delta x + i\beta n \Delta y} G_{m,n} \quad (\text{B.13})$$

If we change the order of integration and summation in (B.13) we obtain

$$\widehat{G} = \int_{-\frac{1}{2}\Delta x}^{\frac{1}{2}\Delta x} \int_{-\frac{1}{2}\Delta y}^{\frac{1}{2}\Delta y} \left\{ \Delta x \Delta y \sum_{m=-\infty}^{\infty} \sum_{n=-\infty}^{\infty} \frac{-e^{i\alpha m \Delta x + i\beta n \Delta y}}{4\pi \sqrt{(m\Delta x - x_0)^2 + (n\Delta y - y_0)^2 + z_{fs}^2}} \right\} dx_0 dy_0 \quad (\text{B.14})$$

Notice that in brackets is exactly the discrete Fourier Transform of the Green function G . Using the aliasing theorem we can relate it to its continuous Fourier transform \widetilde{G} in equation (B.8), that we derived in the previous section, so

$$\begin{aligned} \Delta x \Delta y \sum_{m=-\infty}^{\infty} \sum_{n=-\infty}^{\infty} \frac{-e^{i\alpha m \Delta x + i\beta n \Delta y}}{4\pi \sqrt{(m\Delta x - x_0)^2 + (n\Delta y - y_0)^2 + z_{fs}^2}} = \\ \sum_{m=-\infty}^{\infty} \sum_{n=-\infty}^{\infty} \widetilde{G} \left(\alpha + \frac{2\pi m}{\Delta x}, \beta + \frac{2\pi n}{\Delta y} \right) = \sum_{m=-\infty}^{\infty} \sum_{n=-\infty}^{\infty} -\frac{e^{i\alpha_m x_0 + i\beta_n y_0 - z_{fs} \sqrt{\alpha_m^2 + \beta_n^2}}}{2\sqrt{\alpha_m^2 + \beta_n^2}} \end{aligned} \quad (\text{B.15})$$

where $\alpha_m = \alpha + \frac{2\pi m}{\Delta x}$ and $\beta_n = \beta + \frac{2\pi n}{\Delta y}$. Because this series converges uniformly, it was allowed to exchange the order of summation and integration. When this expression is substituted in (B.14) and we change back the order of integration and summation, the integration can be carried out which finally leaves us with

$$\widehat{G} = \sum_{m=-\infty}^{\infty} \sum_{n=-\infty}^{\infty} \frac{e^{-z_{fs} \sqrt{\alpha_m^2 + \beta_n^2}}}{2\alpha_m \beta_n \sqrt{\alpha_m^2 + \beta_n^2}} \left(e^{-\frac{1}{2}i\Delta x \alpha_m} - e^{\frac{1}{2}i\Delta x \alpha_m} \right) \left(e^{-\frac{1}{2}i\Delta y \beta_n} - e^{\frac{1}{2}i\Delta y \beta_n} \right) \quad (\text{B.16})$$

A similar procedure can be followed to obtain the discrete Fourier transform of the vertical fluid velocity on the free surface, $\frac{\partial \phi}{\partial z}$. This velocity is induced by a dipole distribution on the raised surface panels

$$\frac{\partial \phi}{\partial z}(x_m, y_n) = \sum_{i=-\infty}^{\infty} \sum_{j=-\infty}^{\infty} \sigma_{i,j} Q_{m-i, n-j}$$

The convolution theorem can again be used, leading to

$$\frac{\widehat{\partial\phi}}{\partial z} = \frac{1}{\Delta x \Delta y} \widehat{\sigma} \widehat{Q}$$

\widehat{Q} follows from the definition of the discrete Fourier transform and $Q_{m-i, n-j}$ (3.12)

$$\widehat{Q} = \Delta x \Delta y \sum_{m=-\infty}^{\infty} \sum_{n=-\infty}^{\infty} e^{i\alpha m \Delta x + i\beta n \Delta y} \int_{-\frac{1}{2}\Delta x}^{\frac{1}{2}\Delta x} \int_{-\frac{1}{2}\Delta y}^{\frac{1}{2}\Delta y} \frac{-z f_s dx_0 dy_0}{4\pi ((m\Delta x - x_0)^2 + (n\Delta y - y_0)^2 + z_{fs}^2)^{\frac{3}{2}}}$$

By changing the order of integration and summation we can relate this expression to the continuous Fourier transform \widehat{Q} (B.11) with the aliasing theorem. When the order of integration and summation is changed back again, the integration can be carried out, after which the following expression is found

$$\widehat{Q} = \sum_{m=-\infty}^{\infty} \sum_{n=-\infty}^{\infty} \frac{e^{-z f_s \sqrt{\alpha_m^2 + \beta_n^2}}}{2\alpha_m \beta_n} \left(e^{-\frac{1}{2}i\Delta x \alpha_m} - e^{\frac{1}{2}i\Delta x \alpha_m} \right) \left(e^{-\frac{1}{2}i\Delta y \beta_n} - e^{\frac{1}{2}i\Delta y \beta_n} \right) \quad (B.17)$$

Now, we will focus our attention on the discrete Fourier transforms of the individual terms that occur in the Kelvin condition (1.13). The first term is the second derivative in time of the potential which we obtain by means of a difference scheme

$$\frac{\partial^2 \phi}{\partial t^2} (t_n) = \frac{1}{(\Delta t)^2} \sum_{j=-\infty}^{\infty} d_j^{(tt)} \phi(t_{n-j})$$

In general most of the coefficients $d_j^{(tt)}$ will be zero. This formulation is used to obtain a general expression. A convolution shape is again recognized so that

$$\frac{\widehat{\partial^2 \phi}}{\partial t^2} = \frac{1}{(\Delta t)^3} \widehat{\phi} \widehat{d^{(tt)}} = \frac{1}{(\Delta t)^3} \frac{1}{\Delta x \Delta y} \widehat{\sigma} \widehat{G} \widehat{d^{(tt)}}$$

where

$$\widehat{d^{(tt)}} = \Delta t \sum_{j=-\infty}^{\infty} d_j^{(tt)} e^{-i\omega j \Delta t}$$

A similar approach can be followed to obtain the discrete Fourier transform of the second term in the Kelvin condition, which is also discretized by using difference schemes

$$2U \frac{\partial^2 \phi}{\partial x \partial t} (t_n, x_m) = \frac{2U}{\Delta x \Delta t} \sum_{j=-\infty}^{\infty} d_j^{(t)} \sum_{i=-\infty}^{\infty} d_i^{(x)} \phi(t_{n-j}, x_{m-i})$$

This expression contains a double convolution, so applying the convolution theorem twice results in

$$2U \frac{\widehat{\partial^2 \phi}}{\partial x \partial t} = \frac{2U}{(\Delta x \Delta t)^2} \widehat{d^{(t)}} \widehat{d^{(x)}} \widehat{\phi} = \frac{2U}{(\Delta x \Delta t)^2} \widehat{d^{(t)}} \widehat{d^{(x)}} \frac{1}{\Delta x \Delta y} \widehat{\sigma} \widehat{G}$$

where

$$\widehat{d}^{(t)} = \Delta t \sum_{j=-\infty}^{\infty} d_j^{(t)} e^{-i\omega j \Delta t} \quad \text{and} \quad \widehat{d}^{(x)} = \Delta x \sum_{j=-\infty}^{\infty} d_j^{(x)} e^{i\alpha j \Delta x}$$

Finally, the discrete Fourier transform of $U^2 \frac{\partial^2 \phi}{\partial x^2}$ is

$$U^2 \frac{\partial^2 \widehat{\phi}}{\partial x^2} = \frac{U^2}{\Delta x^2} \frac{1}{\Delta x} \widehat{d}^{(xx)} \widehat{\phi} = \frac{U^2}{\Delta x^2} \frac{1}{\Delta x} \widehat{d}^{(xx)} \frac{1}{\Delta x \Delta y} \widehat{\sigma} \widehat{G}$$

where

$$\widehat{d}^{(xx)} = \Delta x \sum_{j=-\infty}^{\infty} d_j^{(xx)} e^{i\alpha j \Delta x}$$

We already derived the discrete Fourier transform of $\frac{\partial \phi}{\partial x}$, so now we can collect all the terms and write down the complete transform of equation (3.1)

$$\begin{aligned} \widehat{W} \widehat{\sigma} = & \left(\frac{1}{(\Delta t^2)} \sum_{j=-\infty}^{\infty} d_j^{(tt)} e^{-i\omega j \Delta t} + \frac{2U}{\Delta t \Delta x} \sum_{j=-\infty}^{\infty} d_j^{(x)} e^{i\alpha j \Delta x} \sum_{j=-\infty}^{\infty} d_j^{(t)} e^{-i\omega j \Delta t} + \right. \\ & \left. \frac{U^2}{(\Delta x)^2} \sum_{j=-\infty}^{\infty} d_j^{(xx)} e^{i\alpha j \Delta x} + g \frac{\widehat{Q}}{\widehat{G}} \right) \frac{\widehat{G} \widehat{\sigma}}{\Delta x \Delta y} = \widehat{RHS} \end{aligned}$$

To get back the potential itself, we apply the inverse discrete Fourier transform (3.14) to (B.12) and find

$$\phi(t_p, x_m, y_n) = \frac{1}{(2\pi)^3} \int_{-\frac{\pi}{\Delta t}}^{\frac{\pi}{\Delta t}} \int_{-\frac{\pi}{\Delta y}}^{\frac{\pi}{\Delta y}} \int_{-\frac{\pi}{\Delta x}}^{\frac{\pi}{\Delta x}} \frac{\widehat{RHS} \widehat{G}}{\Delta x \Delta y \widehat{W}} e^{i(\omega p \Delta t - m \Delta x \alpha - n \Delta y \beta)} d\omega d\alpha d\beta$$

Using the aliasing theorem and the fact that \widehat{W} is periodic, we can rewrite this into

$$\phi(t_p, x_m, y_n) = \frac{1}{(2\pi)^3} \int_{-\infty}^{\infty} \int_{-\infty}^{\infty} \int_{-\infty}^{\infty} \frac{\widehat{RHS} \widehat{G}}{\Delta x \Delta y \widehat{W}} e^{i(\omega p \Delta t - m \Delta x \alpha - n \Delta y \beta)} d\omega d\alpha d\beta$$

This expression can be compared with the similar expression for the continuous case (3.7). The discrete dispersion relation follows from setting the denominator of the integrand in (B.2) zero, because this gives us the poles that contribute to the wave-like behaviour of the potential, so

$$\begin{aligned} \frac{1}{(\Delta t^2)} \sum_{j=-\infty}^{\infty} d_j^{(tt)} e^{-i\omega j \Delta t} + \frac{2U}{\Delta t \Delta x} \sum_{j=-\infty}^{\infty} d_j^{(x)} e^{i\alpha j \Delta x} \sum_{j=-\infty}^{\infty} d_j^{(t)} e^{-i\omega j \Delta t} + \\ \frac{U^2}{(\Delta x)^2} \sum_{j=-\infty}^{\infty} d_j^{(xx)} e^{i\alpha j \Delta x} + g \frac{\widehat{Q}}{\widehat{G}} = 0 \end{aligned}$$

Bibliography

- [1] M. Abramowitz and I.A. Stegun. *Handbook of Mathematical Functions*. Dover Publications, 1965.
- [2] M. Ba and M. Guilbaud. A fast method of evaluation for the translating and pulsating Green's function. In *Ship Technology Research*, 42: 68-80, 1995.
- [3] P.J.F. Berkvens. *Floating Bodies Interacting With Water Waves*. PhD Thesis, University of Twente, The Netherlands, 1998.
- [4] V. Bertram. *A Rankine Source Method for the Forward-Speed Diffraction Problem*. PhD Thesis, University of Hamburg, Germany, 1990.
- [5] V. Bertram. A 3-D Rankine Panel Method to Compute Added Resistance of Ships. Technical Report 566, Technical University of Hamburg, Germany, 1996.
- [6] J. Broeze. *Numerical Modelling of Nonlinear Free surface Waves with a 3D panel method*. PhD Thesis, University of Twente, The Netherlands, 1993.
- [7] B. Büchmann and J. Skourup. Stability of time-domain Boundary Element Models; Theory and Applications. In *Proceedings of the 14th International Workshop on Water Waves and Floating Bodies*, 1999.
- [8] T.H.J. Bunnik and A.J. Hermans. Stability analysis for the 3D unsteady free-surface condition with raised panels. In *Proceedings of the 13th International Workshop on Water Waves and Floating Bodies*, 1998.
- [9] M.S. Celebi, M.H. Kim and R.F. Beck. Fully Nonlinear 3-D Numerical Wave Tank Simulation. In *Journal of Ship Research*, 42(1):33-45, March 1998.
- [10] X. Chen. An introductory treatise on ship-motion Green functions. In *Proceedings of the 7th International Conference on Numerical Ship Hydrodynamics*, 1999.
- [11] A.H. Clément. An ordinary differential equation for the Green function of the time-domain free-surface hydrodynamics. In *Journal of Engineering Mathematics*, 33(2):201-217, 1998.
- [12] E.F.G. van Daalen. *Numerical and Theoretical Studies of Water Waves and Floating Bodies*. PhD Thesis, University of Twente, The Netherlands, 1993.

- [13] Z. Fang. A new method for calculating the fundamental potential functions induced by a source/dipole polygon. *Applied Mathematics and Mechanics*, 6(7): 675-680, 1985.
- [14] P. Ferrant. Nonlinear wave-current interactions in the vicinity of a vertical cylinder. In *Proceedings of the 12th International Workshop on Water Waves and Floating Bodies*, 1997.
- [15] P.C.A. de Haas. *Numerical simulation of nonlinear water waves using a panel method*. PhD Thesis, University of Twente, The Netherlands, 1997.
- [16] Y. Huang and P. Slavounos. Nonlinear ship motions. *Journal of Ship Research*, 42(2):120-130, June 1998.
- [17] R.H.M. Huijsmans. *Mathematical modelling of the mean wave drift force in current*. PhD Thesis, Delft University of Technology, The Netherlands, 1996.
- [18] H. Iwashita. Diffraction waves of a blunt ship with forward speed taking account of the steady nonlinear wave field. In *Proceedings of the 14th International Workshop on Water Waves and Floating Bodies*, 1999.
- [19] G. Jensen. *Berechnung der stationären Potentialströmung um ein Schiff unter Berücksichtigung der nichtlinearen Randbedingungen an der Wasseroberfläche*. PhD Thesis, University of Hamburg, Germany, 1988.
- [20] Y. Kim, D.C. Kring and P. Slavounos. Linear and nonlinear interactions of surface waves with bodies by a three-dimensional rankine panel method. In *Applied Ocean Research* 19, 1997.
- [21] F.T. Korsmeyer and H.B. Bingham. The Forward Speed Diffraction Problem. In *Journal of ship research*, 42(2):99-112, 1998.
- [22] D. Kring, T. Korsmeyer, J. Singer, D. Danmeier, J. White. Accelerated nonlinear wave simulations for large structures. In *Proceedings of the 7th International Conference on Numerical Ship Hydrodynamics*, 1999.
- [23] W. Lin, S. Zhang, K. Weems and D. Yue. A mixed source formulation for nonlinear ship-motion and wave-load simulations. In *Proceedings of the 7th International Conference on Numerical Ship Hydrodynamics*, 1999.
- [24] D.E. Nakos. *Ship wave patterns and motions by a three dimensional Rankine panel method*. PhD Thesis, Massachusetts Institute of Technology, USA, 1990.
- [25] J.N. Newman. The theory of ship motions. In *Advances in Applied Mechanics* 18, 1978.
- [26] T.F. Ogilvie. Recent progress towards the understanding and prediction of ship motions. In *Proceedings of the 5th Symposium on Naval Hydrodynamics*, 1964.

- [27] J.A. Pinkster. *Low frequency second-order wave exciting forces on floating structures*. PhD thesis, Delft University of Technology, The Netherlands, 1980.
- [28] H.J. Prins. *Time-Domain Calculations of Drift Forces and Moments*. PhD Thesis, Delft University of Technology, The Netherlands, 1995.
- [29] H.C. Raven. *A Solution Method for the Nonlinear Ship Wave Resistance Problem*. PhD Thesis, Delft University of Technology, The Netherlands, 1996.
- [30] J.E. Romate. *The Numerical Simulation of Nonlinear Gravity Waves in Three Dimensions using a Higher Order Panel Method*. PhD Thesis, University of Twente, The Netherlands, 1989.
- [31] L.M. Siervogel. *Time-Domain Calculations of Ship Motions*. PhD Thesis, Delft University of Technology, The Netherlands, 1997.
- [32] J. Skourup, B. Büchmann and H. Bingham. A Second Order 3D BEM for Wave-Structure Interaction. In *Proceedings of the 12th International Workshop on Water Waves and Floating Bodies*, 1997.
- [33] A. Sommerfeld. *Partial differential equations in physics*. Academic Press, New York, 1965.
- [34] K. Tanizawa. A Nonlinear Simulation Method of 3-D Body Motions in Waves; expanded formulation for multiple fluid domains. In *Proceedings of the 11th International Workshop on Water Waves and Floating Bodies*, 1996.
- [35] R. Timman and J.N. Newman. The coupled damping coefficients of a symmetric ship. In *Journal of ship research*, 5(4):1-7, 1962.
- [36] R. van 't Veer. *Behaviour of catamarans in waves*. PhD Thesis, Delft University of Technology, The Netherlands, 1998.
- [37] J.V. Wehausen and E.V. Laitone. *Surface waves*, volume 9 of *Encyclopedia of physics*. Springer-Verlag, Berlin, Germany, 1960.

Summary

A ship sailing at sea experiences a resistance due to its forward speed and incoming waves, which must be balanced by the propulsive power of the ship. To save fuel, this resistance is desired to be as small as possible, and a lot of expensive model tests in seakeeping basins are carried out to minimize the resistance. It is important to have a tool that can predict the forces on a ship sailing in waves and assist these model tests or partially replace them. Mathematics and computer simulations give us such a tool.

The non-viscous part of the resistance of a ship has two major contributions. First, there is the resistance that a ship experiences when it sails at a constant speed in a calm sea, without incoming waves. This is called the wave resistance, and it can reasonably well be predicted by the method RAPID, developed at the MARIN, which calculates the non-linear steady flow around a ship. Second, there is an extra resistance when a ship sails in incoming waves. Although harmonic incoming waves have a mean value which is zero, the forces due to these incoming waves can have a mean value which is non-zero. It is as if the waves want to push the ship ahead of them. This phenomenon is called drifting and is responsible for a resistance increase and can, in oblique waves, result in a change of a ship's course. The increase of the resistance is also known as the added resistance. This added resistance strongly depends on the forward speed of a ship. Prins [28] developed a method that can determine the drift forces for low speeds of a ship. In this thesis we presented a method that can determine the drift forces for moderate and high speeds of a ship as well.

When the speed of a ship increases, the interaction between the steady waves on the one hand and the unsteady waves, the ship motions and the added resistance on the other hand becomes more and more important. Therefore, for moderate and high speeds of a ship, the non-linear steady flow has to be taken into account. We have modeled what happens to a ship when an incoming wave propagates over this non-linear steady wave, reaches the ship, and diffracts. We did this by assuming that the steepness of the incoming waves and the amplitude of the motions of the ship are small. This allowed us to linearize the condition that holds on the free surface, which describes the propagation of the waves, and the condition that holds on the hull of the ship, which relates the water flow and the motions of the ship. Due to the linearization, not only the steady fluid velocities are required, but also first and even second derivatives of these velocities. This sometimes gives problems due to inaccuracies in the steady velocities.

This linear model was solved with a boundary-element method. The free surface and the

hull of the ship were divided in small areas, called panels, and on each of these panels a pulsating source was placed with a constant strength. This way it is made sure that the Laplace equation inside the fluid is fulfilled. The strength of these sources was found by applying the boundary conditions in (or below) the centre of these panels. Furthermore, the boundary condition on the free surface was discretized by using difference schemes for the time derivatives and the space derivatives. For the space derivatives, upwind difference schemes were used. With a stability analysis we showed that the use of the more accurate central difference schemes easily leads to instabilities. By using upwind difference schemes, the occurrence of instabilities can be avoided.

We applied this model to a test ship, and investigated the grid dependence of the steady waves and the derivatives of the steady velocities, which are required to determine the unsteady waves. Then we investigated the dependence of the unsteady waves on the grid size and the time step and the dependence of the predicted forces on the panel density on the hull. In all cases a good convergence was obtained, except for the transfer term, a second derivative of steady velocities, which diverges near the ship, and which has to be obtained by means of extrapolation from the transfer term further away from the ship. To model incoming waves we implemented two methods: a method in which the incoming waves are generated by a wavemaker, and a method in which we separate the incoming waves from the diffracted waves and only calculate the latter. Although both methods gave satisfactory results, we prefer to separate the waves.

After checking the numerical convergence of the model, we validated the model by comparing the predicted motions and added resistance of an LNG carrier with measurements from the MARIN. A comparison was made for three moderate Froude numbers of the carrier, namely $Fn = 0.14$, $Fn = 0.17$ and $Fn = 0.2$. With the separation method, incoming head waves, bow-quartering waves and beam waves were simulated. For short waves, a very good agreement between the predicted and the measured motions and added resistance was found. For long waves there were some deviations, amongst others due to an insufficient size of the free surface. For all wavelengths, the roll motion could not be predicted because we neglect viscosity in our model. Finally, we compared our predictions with the predictions obtained by using the uniform flow and the double-body flow. It turned out that only by using the non-linear steady flow, an accurate prediction of the added resistance can be obtained.

Samenvatting

Een schip dat vaart op zee ondervindt een weerstand door zijn voorwaartse snelheid en door inkomende golven, die moet worden tegengewerkt door de kracht die de schroef van het schip levert. Om brandstof te besparen moet deze weerstand zo klein mogelijk worden gehouden. Er worden daarom een heleboel dure proeven uitgevoerd om de weerstand te minimaliseren. Het is belangrijk om een hulpmiddel te hebben dat de krachten op een schip dat in golven vaart kan voorspellen, en de modelproeven kan assisteren of gedeeltelijk vervangen. Dit hulpmiddel kan worden gevonden in de wiskunde en de computer simulaties.

Het niet-viskeuse gedeelte van de weerstand van een schip kan worden opgedeeld in twee belangrijke stukken. Ten eerste is er de weerstand die een schip ondervindt wanneer het met een constante snelheid in vlak water vaart. Dit wordt de golfweerstand genoemd. De golfweerstand kan worden voorspeld met de methode RAPID, die ontwikkeld is op het MARIN, en die de niet-lineaire stationaire golven rondom een varende schip bepaalt. Ten tweede ondervindt een schip een extra weerstand als het in golven vaart. Alhoewel harmonische inkomende golven een gemiddelde amplitude hebben die nul is, kunnen de krachten die door deze golven op een schip werken een gemiddelde waarde hebben die ongelijk aan nul is. Het is net alsof de golven het schip voor zich uit willen duwen. Dit verschijnsel wordt driften genoemd en kan een toename van de weerstand veroorzaken en kan in schuine golven ertoe leiden dat het schip van koers verandert. De toename van de weerstand wordt ook wel de toegevoegde weerstand genoemd. Prins [28] heeft een methode ontwikkeld die de driftkrachten voor lage snelheden van een schip kan bepalen. In dit proefschrift hebben we een methode gepresenteerd die de driftkrachten ook voor middelmatige en hoge snelheden van een schip kan bepalen.

Als de snelheid van een schip toeneemt, wordt de interactie tussen de stationaire golven enerzijds en de instationaire golven, de scheepsbewegingen en toegevoegde weerstand anderzijds, steeds groter. Daarom moet voor middelmatige en hoge snelheden van een schip de niet-lineaire stationaire stroming in rekening worden gebracht. We hebben gemodelleerd wat er gebeurt met een schip als een inkomende golf over de niet-lineaire stationaire golf voortbeweegt, het schip bereikt en diffracteert. We hebben dit gedaan door te veronderstellen dat de steilheid van de inkomende golven en de amplitude van de bewegingen van het schip klein zijn. Door dit te doen konden we de de conditie op het wateroppervlak, die de voortbeweging van de golven beschrijft, en de conditie op de scheepsromp, die de interactie tussen het water en de scheepsbewegingen beschrijft, lineariseren. Door deze

linearisatie hebben we niet alleen de stationaire snelheden van de waterdeeltjes nodig, maar ook diverse afgeleiden hiervan. Door onnauwkeurigheden in de stationaire snelheden is het soms lastig om bepaalde afgeleiden uit te rekenen.

Dit lineaire model hebben we opgelost met een randintegraal methode. Het wateroppervlak en de scheepsromp hebben we opgedeeld in kleine gebiedjes die panelen heten, en op elk van deze panelen hebben we een bron gezet met een constante bronsterkte. Dit zorgt ervoor dat aan de Laplace vergelijking is voldaan. De bronsterkte is gevonden door de randcondities toe te passen in (of onder) het midden van de panelen. Ook hebben we de conditie op het wateroppervlak gediscrèteerd door gebruik te maken van upwind differentieschema's. Met een stabiliteitsanalyse hebben we aangetoond dat het gebruik van de nauwkeurigere centrale differentieschema's al snel tot instabiliteiten leidt. Door upwind differentieschema's te gebruiken kan dit worden voorkomen.

Dit model hebben we toegepast op een testschip en we hebben onderzocht in welke mate de stationaire golven en de afgeleiden van de stationaire snelheden van de paneelgrootte op het wateroppervlak afhangen. Daarna hebben we onderzocht hoe de instationaire golven afhangen van de paneelgrootte en de tijdstap en hebben we bekeken of de krachten op het schip afhangen van de paneelgrootte op de romp. In alle gevallen vonden we een goede convergentie, behalve bij het uitrekenen van de transfer term, een tweede afgeleide van de stationaire snelheden, die vlakbij het schip divergeert en daar door middel van extrapolatie moet worden verkregen. Om de inkomende golven te modelleren hebben we twee methoden geïmplementeerd: een methode waarin de inkomende golven worden gegenereerd door golfopwekkers, en een methode waarin we de inkomende golf van de totale golf afsplitsen en dus alleen de gediffracteerde golf uitrekenen. Alhoewel beide methodes goede resultaten gaven, geven we de voorkeur aan de tweede methode.

Nadat we de numerieke convergentie hadden gecontroleerd hebben we het model gevalideerd door de voorspelde bewegingen en toegevoegde weerstand van een gastanker te vergelijken met metingen van het MARIN. De berekeningen zijn gedaan voor drie middelmatige Froude getallen, namelijk $F_n = 0.14$, $F_n = 0.17$ en $F_n = 0.2$. Kogolven, schuin van voren inkomende golven en dwarsgolven zijn gesimuleerd. Voor korte golven kwamen de voorspelde bewegingen en toegevoegde weerstand goed overeen met de metingen. In lange golven waren er wat afwijkingen, mede doordat we een te klein wateroppervlak hebben gebruikt. Voor alle golfengtes werd het slingeren niet goed voorspeld. Dit komt doordat er geen viscositeit is in ons model. Tenslotte hebben we onze voorspellingen vergeleken met voorspellingen die verkregen zijn met gebruikmaking van de uniforme stroming en de double-body stroming. Het blijkt dat alleen door de niet-lineaire stationaire stroming te gebruiken er een nauwkeurige voorspelling van de toegevoegde weerstand kan worden verkregen.

Dankwoord

Ten eerste wil ik professor Hermans bedanken voor het opzetten van dit onderzoek en de begeleiding gedurende de afgelopen vier jaar, al ben ik veel mijn eigen gang gegaan.

Bij het MARIN ben ik voornamelijk Hoyte Raven veel dank verschuldigd voor het leveren van de stationaire snelheidsverdelingen voor het testschip en de LNG carrier. Met name de zeer fijne verdeling die nodig was voor de convergentiestudie heeft nogal wat moeilijkheden met zich meegebracht. Tevens wil ik hem bedanken voor de discussies die we over mijn werk hebben gehad, samen met René Huijsmans, die mij tevens heeft voorzien van meetresultaten.

Alle leden van de vakgroep TA van de afgelopen vier jaar, van afstudeerders tot promovendi en vaste staf, wil ik bedanken voor de gezellige koffiepauzes en lunches. Deze hebben veel kleur gegeven aan een anders toch wel geïsoleerd AIO bestaan. Mirjam Nieman wil ik bedanken voor het doorlezen en corrigeren van de engelse tekst. Zonder haar zou de leesbaarheid van de tekst een stuk minder zijn geweest.

Tenslotte wil ik mijn familie bedanken voor het verschaffen van een thuishaven waar ik mijn gedachten kon verzetten, om daarna met frisse moed het onderzoek weer op te pakken.

Curriculum Vitae

The author was born on March 22, 1973 in Gouda, the Netherlands. After attending secondary school at the "Samenwerkingsschool" in Waddinxveen, he passed his VWO-exam in 1991. He then started his study Applied Mathematics at the Delft University of Technology, where he graduated in 1995 on a topic concerning the behaviour of a Surface Effect Ship in waves, which was done in cooperation with the MARIN. After his graduation he started working as a Ph.D. student at the Applied-Analysis department of the faculty of Information Technology and Systems. The results of this work are shown in this thesis.